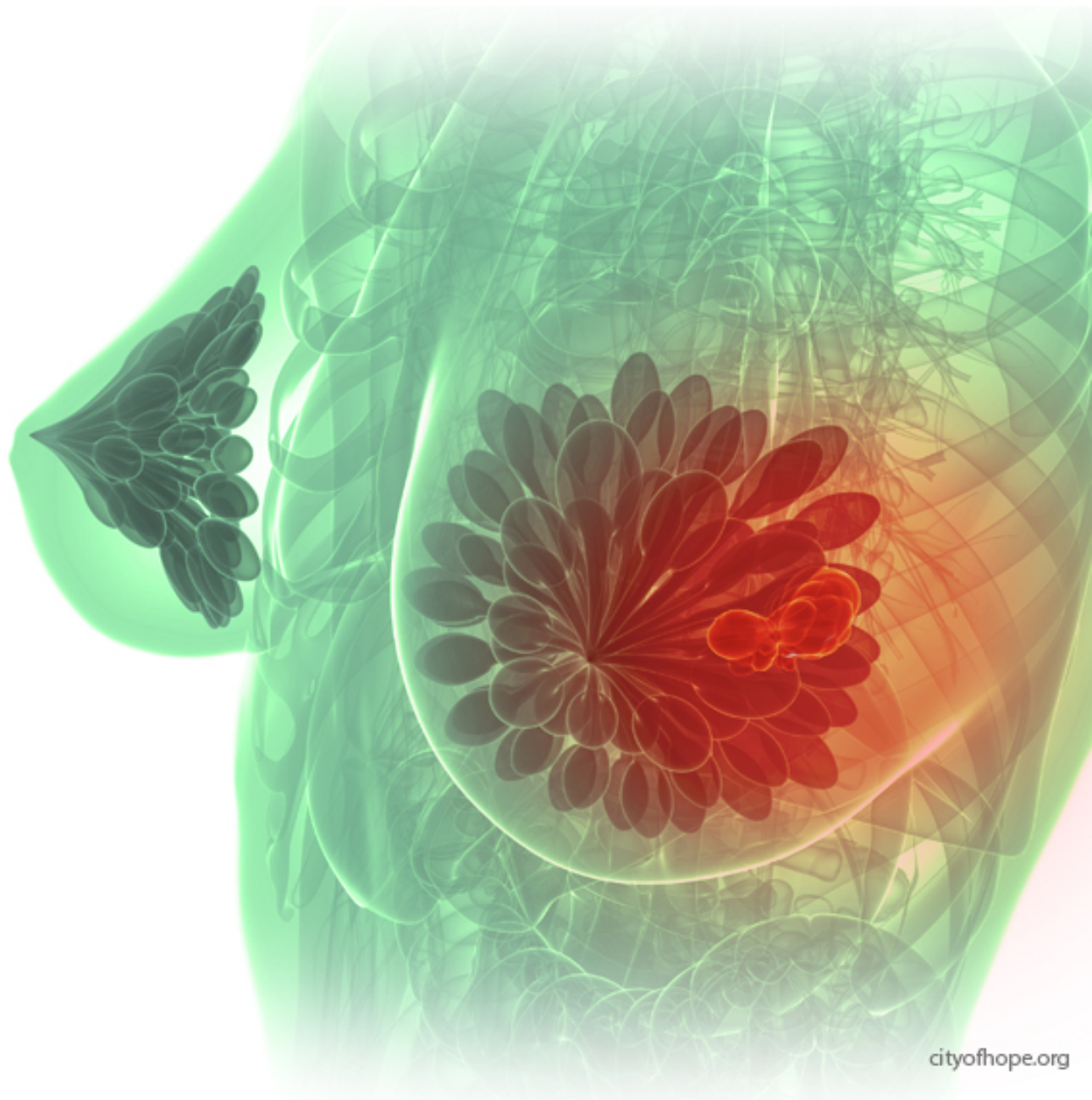


Master Thesis

# Automatic Classification of Non-Mass Breast Lesions in Dynamic Contrast-Enhanced MR Images

Mohammad Razavi

University of Bremen



cityofhope.org



**MASTER THESIS**

**AUTOMATIC CLASSIFICATION OF  
NON-MASS BREAST LESIONS IN DYNAMIC  
CONTRAST-ENHANCED MR IMAGES**

by

**Mohammad Razavi**

in partial fulfillment of the requirements for the degree of

**Master of Science**

in Digital Media

at the University of Bremen,

to be defended publicly on Tuesday October 19, 2015 at 2:00 PM.

Supervisors: Prof. Dr. Gabriel Zachmann  
Prof. Dr. Udo Frese

Advisor: Dr. Lei Wang, Fraunhofer Mevis

*This thesis is confidential and cannot be made public until October 31, 2015.*



# ABSTRACT

## **Purpose**

Today, breast cancer is the highest frequent diagnosed cancer and the most common cause of death among women. The early detection of cancer tumors via the screening programs is the essential policy to increase survival rates. Malignant cancer tumor, in its developed stage, can attack the surrounding cells and metastasis to distant body parts. Metastasis is the main cause of death in patients. In order to prevent that, the malignant cancer tumor has to be detected and treated in its early stage.

## **Methods**

Among lesion types the non-mass-like enhancements are the one with complex distribution patterns of enhancing tissue dispersed between normal tissues, thus their detection is not simple and more challenging than the masses. To fulfill this task, a semi-automatic mean-shift algorithm is used to segment totally 106 cases of non-mass lesions acquired from MR images of 86 patients (38 benign and 68 malignant). First, the segmented lesion volumetric object was packed using a sphere packing algorithm. Then, all sphere center coordinates were normalized. Next, a combination of different features was extracted from the internal spheres using various histograms, Zernike moments, and graph formation features. Finally, random forest machine learning is trained to be integrated into CAD (computer-aided diagnosis) system to do the classification.

## **Results**

Classification is done using 10-fold cross validation technique in patient level over the ground truth dataset. In differentiating between malignant and benign lesions, an accuracy of 89.62%, precision of 90.1% and area under the ROC curve (AUC) of 0.972 is achieved using Random Forest algorithm by applying Mean Decrease Accuracy and Principal Component Analysis (PCA) feature selections.

## **Conclusion**

The results suggest that the morphological features can be used for developing automated breast CAD for early detection of malignant non-mass lesions to achieve a high diagnostic performance. A higher accuracy can be even achieved, by taking advantage of morphological combined with kinetic, and texture features.

**Keywords:** breast MRI; non-mass; enhancement; lesion; classification; sphere packing; morphology; feature extraction; computer-aided diagnosis

*Mohammad Razavi  
Bremen, October 2015*



# ACKNOWLEDGEMENTS

I would like to dedicate my work to all the people that helped me throughout almost a year adventure of my Master's thesis. First of all, I am grateful to my first supervisor, Professor Gabriel Zachmann, not only for his constant trust and support, but also for his beneficial ideas. I should also thank my second supervisor, Professor Udo Frese for taking the time out of his busy schedule and his brilliant ideas. I appreciate my advisor and friend Lei Wang for all his support and concern through this time. His comments and criticism have always been of great guidance to me.

The thesis described herein was undertaken at Fraunhofer Institute for Medical Image Computing MEVIS (Bremen, Germany) between February and October 2015. Having said that, I am thankful of MEVIS breast care team, particularly Hendrik Laue who has enabled this work to proceed swiftly.

I would also like to highlight my collaboration with the computer graphics group at University of Bremen, especially Dr. Rene Weller and Jörn Teuber, who provided me with the Protosphere extended library.

I also thank my colleagues in Radboud University Nijmegen Medical Centre in Netherlands for supplying acquisition sequences for the MRI measurements and in addition to that, I thank all anonymous patients, providing their breast MR scans for scientific works. I will continue praying for their good health and fast recovery.

Lastly, I would like to show my immense gratitude to my wife Parnian for supporting me all the time along my study.



# CONTENTS

<b>Abstract</b>	<b>iii</b>
<b>Acknowledgements</b>	<b>v</b>
<b>List of Figures</b>	<b>ix</b>
<b>1 Introduction</b>	<b>1</b>
1.1 Structure of the thesis . . . . .	3
<b>2 Background and Theory</b>	<b>5</b>
2.1 Anatomy of the Breast . . . . .	5
2.2 Breast Cancer . . . . .	5
2.3 Dynamic Contrast-Enhanced Magnetic Imaging of the Breast . . . . .	9
2.4 Pathophysiology of Lesion Characteristics . . . . .	9
2.4.1 Morphological Features . . . . .	10
2.4.2 Kinetical Features. . . . .	12
2.4.3 Textural Features . . . . .	12
2.5 Related Work . . . . .	14
<b>3 Materials and Method</b>	<b>17</b>
3.1 Materials . . . . .	17
3.2 Method Outline. . . . .	18
3.3 Pre-Processing . . . . .	19
3.3.1 Motion compensation . . . . .	19
3.3.2 Lesion Segmentation. . . . .	20
3.4 Sphere Packing . . . . .	22
3.5 Normalization . . . . .	24
3.6 Feature Extraction . . . . .	25
3.6.1 Volume-Radius Histogram . . . . .	26
3.6.2 3D Spherical Shape Histogram . . . . .	27
3.6.3 Graph Topological Features . . . . .	31
3.6.4 3D Zernike Descriptors. . . . .	43
3.7 Classification using Random Forest. . . . .	46
<b>4 Development</b>	<b>49</b>
4.1 Processing Pipeline. . . . .	49
<b>5 Evaluation and Results</b>	<b>57</b>
5.1 Performance Evaluation Measures . . . . .	57
<b>6 Summary and Conclusions</b>	<b>69</b>
6.1 Failed experiment . . . . .	70
6.2 Opportunities for further work . . . . .	71
6.3 Limitations . . . . .	72
<b>Bibliography</b>	<b>73</b>



# LIST OF FIGURES

2.1	The anatomy of the breast . . . . .	6
2.2	Normal cells and tumor cells . . . . .	6
2.3	Illustrations of breast lesions . . . . .	7
2.4	Different breast tissue density in MR imaging . . . . .	8
2.5	Dynamic subtraction images of the intermediate post-contrast breast MR sequence, including enhancements . . . . .	8
2.6	Patients position while breast MRI is performed . . . . .	9
2.7	Images acquired from DC-MRI several time intervals before and after the injection of contrast agent . . . . .	10
2.8	Schematic illustration of morphological features exhibited by mass lesions . . . . .	11
2.9	Contrast Enhancement Kinetic Curves . . . . .	13
2.10	Texture features based on the spatial relations of a pair of voxels . . . . .	13
3.1	The breast MRI with an overlay provided by the radiologist . . . . .	17
3.2	The proposed lesion classification process workflow . . . . .	18
3.3	Maximum intensity projection images of the difference image $t1 - t0$ . . . . .	19
3.4	Motion quantification visualization for a breast, blurry MRI scan . . . . .	20
3.5	Lesion segmentation using mean shift algorithm and applying threshold . . . . .	21
3.6	Mean shift segmentation applied on a colored image . . . . .	21
3.7	Example of a 2D feature space analysis using mean shift . . . . .	23
3.8	Sphere packing prototype convergence visualization . . . . .	23
3.9	Sphere packing of the lesion 3D volume . . . . .	25
3.10	An example of spheres components before and after normalization . . . . .	26
3.11	Volume-Radius histogram examples of benign and malignant lesions . . . . .	27
3.12	Shells and sectors as basic space decompositions for shape histograms . . . . .	28
3.13	Several 3-D shape histograms of the example protein 1SER-B . . . . .	29
3.14	Space decompositions for the proposed 3D Spherical shape histogram . . . . .	30
3.15	Different strategies for choosing the place for spherical wireframe center point . . . . .	31
3.16	Corresponding histogram of the proposed 3D space decomposition . . . . .	31
3.17	Proportion of smallest enclosing spherical wireframe, filled by embedded spheres . . . . .	32
3.18	Different graph structures, acquired from various algorithms . . . . .	33
3.19	$k$ -nearest neighbors algorithm with various $k_{max}$ values . . . . .	34
3.20	The same edge density graph compactness for two different graphs . . . . .	35
3.21	Converted distance matrix of a graph and associated metrics . . . . .	37
3.22	A graph with the "status", "contrastatus" and "prestige" . . . . .	37
3.23	LAP examples of linear and circular graphs . . . . .	38
3.24	Same Dunn's index for $G3$ and $G4$ . . . . .	38
3.25	Same MinMaxCut, conductance and coverage values for both graphs . . . . .	39
3.26	Two graph clusters with $MQ^*$ smaller than $MQ$ . . . . .	41
3.27	Comparison of cluster partitions $P$ and $P'$ . . . . .	43
3.28	Graph topological features extraction example . . . . .	43
3.29	Graphical illustration of top 20 Zernike terms as a pyramid . . . . .	44
3.30	The 3D spherical harmonic basis . . . . .	45

3.31	Example visualizations of selected 3D Zernike functions $Z_{53}^m$ and $Z_{82}^m$ . . . . .	46
3.32	Random forest a combination of decision trees . . . . .	48
4.1	MeVisLab GUI on Mac OS X . . . . .	50
4.2	MeVisLab image processing network example . . . . .	51
4.3	The processing network used in this work . . . . .	53
4.4	The two initial parts of this study's processing network in MeVisLab . . . . .	54
4.5	The third part of this study's processing pipeline in MeVisLab . . . . .	54
4.6	Integration of the proposed method into Computer-Aided Diagnosis (CADx) tool . . . . .	55
5.1	The comparison of classification results between three classifiers . . . . .	60
5.2	Charts of Random Forest analysis . . . . .	61
5.3	Classification accuracy only based on Volume-Radius Histogram features . . . . .	62
5.4	Classification accuracy only based on 3D shape Histogram features . . . . .	63
5.5	Classification accuracy only based on Zernike moments features . . . . .	64
5.6	Variable importance in Random Forest evaluation . . . . .	65
5.7	Classification evaluation sample data . . . . .	67
6.1	Distribution orientation of the lesion and nipple direction . . . . .	70

# 1

## INTRODUCTION

The research described herein was carried on at the Fraunhofer MEVIS<sup>1</sup> Institute for Medical Image Computing, located in the city of Bremen in Germany between February and July 2015. It constitutes part of ASSURE project<sup>2</sup>, a European Union funded research project seeking to develop image analysis tools to assist personalized breast cancer screening based on risk and breast density markers.

At the moment, women's breast screening is almost solely done by mammography. However, for the women with dense breasts, mammography shows low sensitivity for detecting breast cancer. For that reason, new MRI based screening methods and automated breast ultrasound imaging need to be developed. Using new techniques for prospective personalized screening will minimize the risk of a particular patient to have a cancer missed at its early stage, resulting in decreased mortality and increased quality of life due to less radical treatment options.

Statistically, after lung cancer, breast cancer is the second most frequent one and the fifth most common cause of cancer related deaths in the world. Only among women, breast cancer is the highest frequent diagnosed one and the most common cause of death in both developed and developing countries [1]. The early detection is the essential policy to increase survival rates.

As a result, screening programs based on x-ray mammography have been introduced which have some recognized constraints such as the matter of overlapping image of 3D tissue into 2D [2], low specificity in the detection of malignancy, and low sensitivity for women with dense breast tissue [3]. Therefore, the exploration of alternative imaging modalities led to using new techniques, including magnetic resonance imaging (MRI), sonography (ultrasound) and nuclear medicine (PET and SPECT) imaging [4]. These modalities are commonly used in patients with known or suspected breast cancer or in the screening of high risk patients. Amidst these modalities MRI shows the most promise for improved screening of high risk women [5].

In the modern breast MR imaging, which is based on dynamic contrast-enhanced (DCE) MRI, three dimensional T1-weighted images of one or both breasts are acquired at different time intervals before and after the injection of a contrast agent containing gadolinium. Normally, a clinical DCE-MRI scan consists of one pre-contrast volume, followed by four to six contrast-enhanced volumes, in each there are a large number of 2D slice images are acquired in intervals about 60 to 120 seconds [5].

Based on the difference of voxels intensity level in the captured volumes, a signal-intensity time curve can be acquired which its shape is an important criterion to discriminating lesions and their

---

<sup>1</sup>Fraunhofer MEVIS website: <http://mevis.fraunhofer.de> [Accessed on 26 August 2015]

<sup>2</sup>ASSURE project website: <http://www.assure-project.eu> [Accessed on 26 August 2015]

types based on their kinetic features [6]. The modality of post-initial enhancement can be used to distinguish malignant and benign tumors: the curve may plateau, decline, or continue to increase more slowly with a delayed washout. However, these characteristics do not guarantee the accurate detection [5].

Besides kinetic characteristics, morphological features can also play an important role in lesion type differentiation. For instance, a lesion is identified as malignant if there is a focal mass with irregular or speculated margins and a benign lesion is identified as the one having smooth or lobulated margins with internal septations or if the mass is cystic [7].

Automatic analysis of cancer tumors using computer techniques is necessary, since manual integration along with observation of DCE-MRI volumes is a labor-intensive and even subjective task for radiologists [8]. Utilizing the modern *Computer-Aided Detection (CADe)* and *Computer-Aided Diagnosis (CADx)* systems can improve the objectivity, consistency as well as the efficiency of breast lesion analysis. Hence the DCE-MRI presents a number of challenges for automatic examination: the highly variation of the temporal and spatial distributions of contrast agent in suspicious tissue (both for an individual patient and between patients) [9], and also in comparison to CT imaging, the observed MR signal cannot be easily calibrated [5].

Some recent studies have achieved high discriminating power detecting invasive breast lesions using a quantitative combination of morphological, kinetic, and spatio-temporal features. They achieved the degree of diagnostic sensitivities up to 97% and specificities up to 76.5% [10, 11]. In such cases, MRI reaches a very high sensitivity in the detection of invasive breast cancer due to both the typical appearance (ill-defined shape, stellate borders, and rim enhancement) of malignant tumors and characteristic signal intensity (SI) time courses of contrast enhancement [10].

Most of the studies on lesion detection are performed in the preoperative staging of patients with suspicious lesions, including predominantly tumors with an extension greater than 2cm, in which MRI provides an accurate estimation of invasive breast cancer tumors [10, 12]. In contrast, for non-mass-like enhancing lesions, MRI shows less sensitivity with more than 40% of the false-negative diagnosis [10]. Therefore, double reading is suggested for such cases which is time-consuming, and as an alternative, a computer-assisted system is suggested [13].

The diagnosis of non-mass-like enhancement lesions is a highly challenging task, since they exhibit a heterogeneous appearance in breast MRI with high variations in kinetic characteristics and typical morphological parameters [14, 15] and have a lower reported specificity and sensitivity than mass-enhancing lesions. Early detection of such lesions is highly beneficial since it reduces the biopsies numbers. However, due to their much lower sensitivity and specificity compared with mass-like lesions, and the need for more advanced algorithms, very few studies investigated the characterization of non-mass lesions so far [10].

The focus of the current work, is on classification of the non-mass lesions to benign or malignant types, using merely the morphological features. After segmenting the lesion from the MR image using Mean Shift algorithm, the segmentation is treated as a 3D volumetric object. Then it is filled internally by spheres using Protosphere, GPU-assisted prototype guided sphere packing algorithm for arbitrary objects [16]. By taking advantage of a novel approach, several shape feature vectors are acquired from each segmentation sample. Finally a multiple kernel random forest machine learning technique classifies the lesion types based on the serial combination of those features acquired from a ground truth dataset of 106 lesions.

This novel approach exhibits high classification accuracy of 89.62%, precision of 90.1 with the area under the curve (AUC) of 0.972 using 10-fold cross validation technique over 106 lesion samples obtained from MR images of 86 patients.

## 1.1. STRUCTURE OF THE THESIS

The remainder of this thesis is organized as follows:

- **Chapter 2** presents background knowledge in support of the next chapters. First, an introduction of concepts in MRI, followed by an overview of breast MR imaging and its physiopathology basis. The chapter then contains a section on breast cancer, and its appearance in MRI, thus the kinetic, morphological and textural features of the lesions. Finally, the literature review and related work are presented.
- **Chapter 3** presents the materials used with a description of the method. First, the specification of the “ground truth” data, then the method outline starting from pre-processing by motion compensation of MRI sequences and lesion segmentation from MR subtraction image using provided mask and mean shift algorithm. The processing continues by sphere packing the lesions’ volume, normalization of the spheres and feature extraction. Four feature extraction methods were used, including *Volume-Radius histogram*, *3D spherical shape histogram*, *Graph topological features* and *Zernike invariants*. Finally the Random Forest machine learning is introduced to evaluate the method results using the combination of all the features.
- **Chapter 4** shortly describes the *MeVisLab* software and the proceeding pipeline used in this work. A short description of each module in the network is provided considering their connections and data-flow.
- **Chapter 5** presents several measures for performance evaluation followed by comparisons of evaluation using several machine learning algorithms. Next, using feature selection, the number of features reduces using *Mean Decrease Accuracy* and *Principal Components Analysis* methods.
- **Chapter 6** summaries the important findings of the research and draws conclusions from them. It also outlines the limitations of the research and failed experiments, then provides future directions.



# 2

## BACKGROUND AND THEORY

### 2.1. ANATOMY OF THE BREAST

Knowing about breast anatomy is important in order to understand the development of cancer tumors. The two breasts are formed during the fetal period by epidermis, a depression which forms a mammary pit on the local of the mammary gland. The region where appear the mammary glands is located on left and right sides of the upper ventral region of the trunk. The breasts exist in both woman and man, but the mammary glands are normally most developed in female, except in some particular circumstances related to hormonal problems [17].

As can be seen in [Figure 2.1](#), each breast has a nipple with a series of openings of lactiferous ducts, where milk emerges during the lactation process. Areola is a pigmented area of skin which surrounds the nipple. The skin at the areola has a convoluted surface and contains many sweat and sebaceous glands which open directly to the skin surface. The oily secretion of the sebaceous glands is protective during lactation. In each breast there is a mammary gland, which produces milk and consists of 15 to 20 lobes which are separated by adipose tissue. Each lobe consists of smaller components called lobules, composed of clusters of milk secreting glands called alveoli [18]. In the lactating process of woman, the alveoli secrete milk into the mammary ducts which they expand to form lactiferous sinuses near the breast, where there might be stored some milk before draining into the lactiferous duct. In lobules or ducts are the places that cancer usually develops [19].

There are some factors which makes the composition of breast vary from person to person, including age, pregnancy, lactation, menstruation, and the menopause, which makes alveolar structures regress and reduce the vascularity of the connective tissue [20].

### 2.2. BREAST CANCER

Cancer is a kind of malady in which normal body cells are altered in appearance and functionality. They start growing disorderly and create a tumor (see [Figure 2.2](#)) [18]. Breast cancer is usually a tumor, appears from the epithelium and developing in the lactiferous ducts; it infiltrates the *parenchyma* (the functioning tissue of an organ other than the supporting or connective tissue). It often happens to women who have not given birth to a child or breastfed. The cancer lesion generally appear in the tipper outer quadrant of the breast, since this is the location of most of the glandular tissue. A slow-growing breast cancer may take up to 10 or more years to become palpable, or to reach the size of a small pea [21].

The breast tissue can be divided into two major parts: the non-functioning part consist of non-

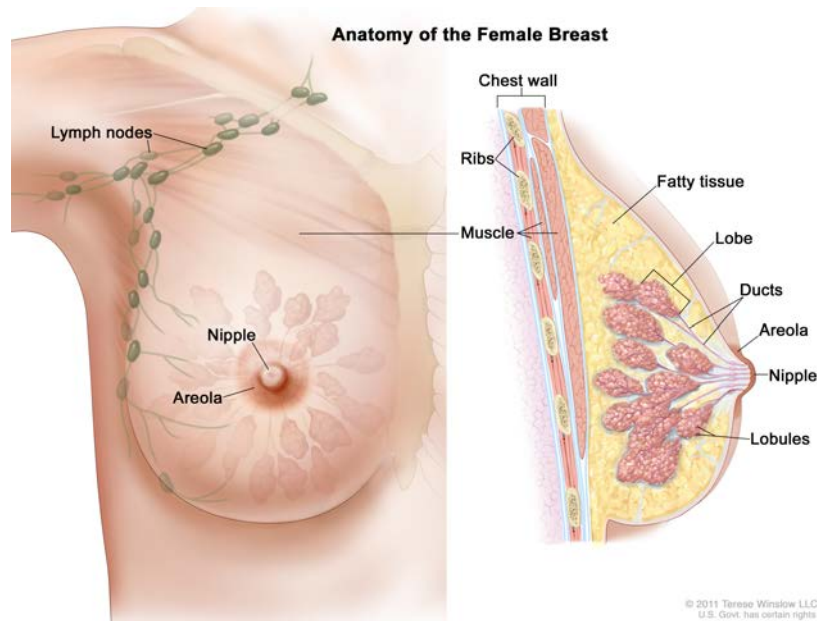


**Figure 2.1:** The anatomy of the breast (Figure taken from [www.cancer.gov](http://www.cancer.gov)).

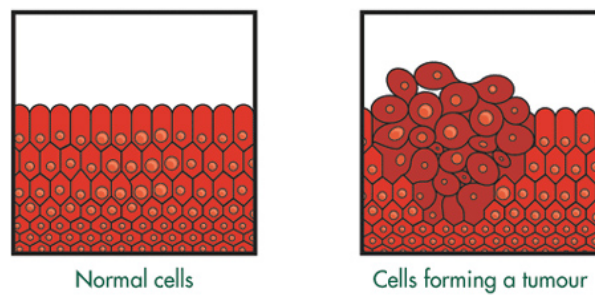


**Figure 2.2:** Normal cells and tumor cells (Figure taken from [macmillan.org.uk](http://macmillan.org.uk)).

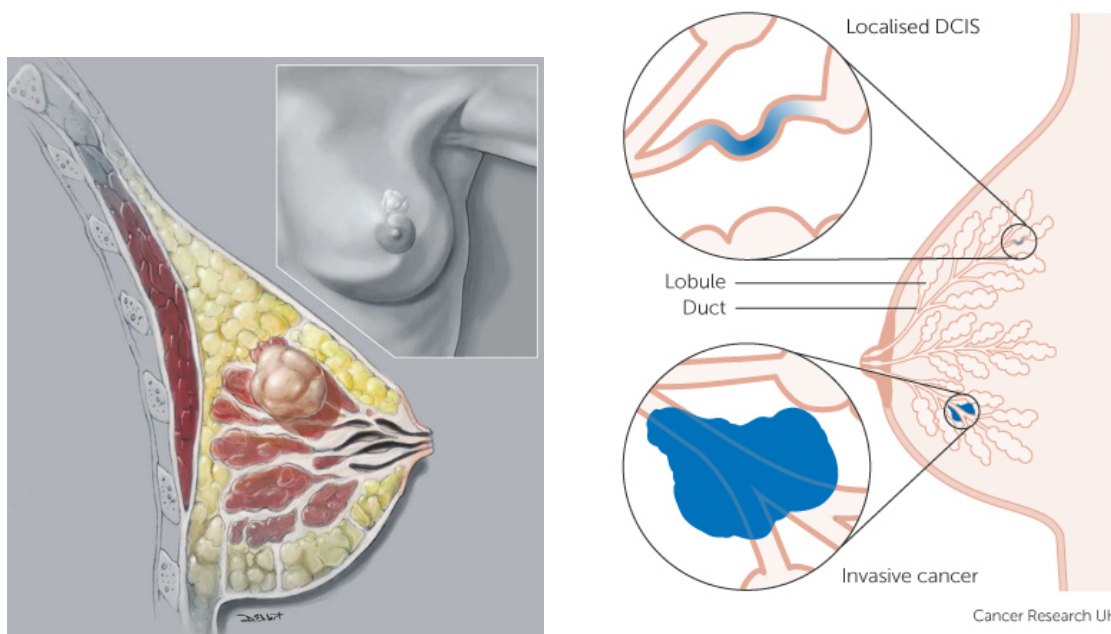
dense fatty tissue, which only helps to keep the other tissues, and the functioning dense part reflects the proportion of epithelial and stromal tissue in the breast (fibroglandular tissue). Breast cancers originate in epithelial cells, so greater areas of fibroglandular tissue may reflect a main part of cells that are at risk of carcinogenesis and/or an increased rate of epithelial proliferation. Therefore, breast tumors do not often appear in fatty or non-glandular tissue [18]. It is plausible that many of the established breast cancer risk factors influence risk through their effect on density [22]. It should be noted that, breast cancer risk in women is 100 times more than men. Only less than 1% of men get cancer, often in high age and it is not usually detected in early stage [20].

### Benign – Malignant

A dubious breast tissue is called *malignant* at the point that it attacks other cells around it and spread (metastasize) to distant other body parts [23]. Metastasis occurs when genetically unstable cancer cells adapt to a tissue micro-environment that is far from the main tumor [24]. In order to prevent metastasis, the cancer has to be detected and treated, since instead of the primary tumor, its metastasis at distant sites, are the main cause of death in patients [25].

When a tissue is suspicious and not yet malignant, it is called *benign*. Such tumors are abnormal growths and can become larger, but they do not spread outside the breast to other body organs.

In short, a suspicious tissue is called benign when it has not shown malignancy (see Figure 2.3(a)). This means the tissue can grow larger, but does not spread to other parts of the body, thus is not a life threat yet [18].



(a) (Figure taken from [ubang75.com](http://ubang75.com))

(b) (Figure taken from [cancerresearchuk.org](http://cancerresearchuk.org))

**Figure 2.3:** Illustrations of breast lesions. **Left:** Breast tumors often appear in the functioning tissue of the breast and they even might appear on the patient's skin. **Right:** Two types of non-invasive breast tumors, *Ductal Carcinoma In Situ (DCIS)* and *Lobular Carcinoma In Situ (LCIS)*, which might be found inside a milk duct or lobules.

Nevertheless, the benign condition of breast is important, since the women who has benign tumors are in danger of developing cancer [23].

Breast density reflects the proportion of epithelial and stromal tissue in the breast, which is more inclined to have breast cancer. Therefore, breast density has the potential to be used as a predictor of breast cancer risk. This factor can be used to monitor risk lowering interventions and as an intermediate end point in studies of breast cancer etiology [22] (see Figure 2.4).

### Invasive – Non-invasive

*Invasive* cancers are the ones that have spread to the healthy surrounding cells beyond their own developing tissue. *Non-invasive* breast cancers are usually the abnormalities in cells found inside the functioning tissue and have not spread to outer areas yet. Figure 2.3(b) shows two types of non-invasive tumors, *Ductal Carcinoma In Situ (DCIS)* and *Lobular Carcinoma In Situ (LCIS)*, which might be found inside a milk duct or lobules. In some cases, DCIS may become invasive and spread to surrounding tissues [18].

### Mass – Non-mass

According to Breast Imaging Reporting and Data System (BI-RADS) [26], the breast cancers found in Dynamic Contrast-Enhanced Magnetic Resonance Imaging (DCE-MRI) (described in section 2.3), can be categorized as mass or non-mass-like enhancements. In enhancing tissue of DCE-MR image, mass-like tumors are compact regions which are clearly notable from the healthy tissue. In

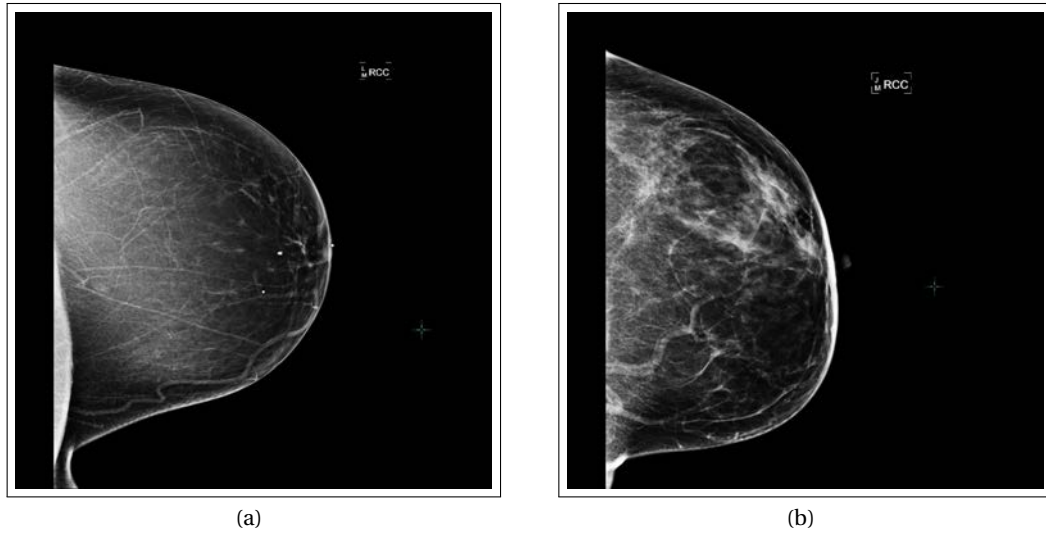


**Figure 2.4:** (a) shows an MR image of a breast with "scattered fibroglandular" tissue and low density; (b) shows an MR image of a breast with "heterogeneously dense" breast tissue (more than 50%) (Figure taken from [staceyvitiellomd.com](http://staceyvitiellomd.com)).

contrast, non-mass-like enhancements have complex distribution patterns of enhancing tissue dispersed among normal tissue. It is not clear to distinguish which part belongs to the glandular tissue of the breast and which tissue is part of the tumor, since the non-mass-like tissue is typically scattered around it [18]. Figure 2.5 shows two subtraction images of second and first different MR sequences ( $t_1 - t_0$ ), including both types of mass and non-mass lesions.

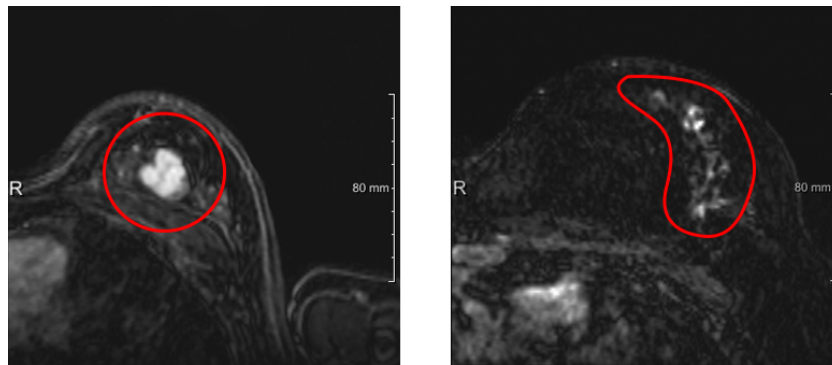


**Figure 2.5:** Dynamic subtraction images of the intermediate post-contrast breast MR sequence, including enhancements. Both shows the subtraction image of the first two MR sequence ( $t_1 - t_0$ ) with a mass enhancement (on **left**) and a non-mass-like enhancement (on **right**). Mass-like enhancements are compact regions which are clearly notable from the healthy tissue, in contrast, non-mass-like enhancements have complex distribution patterns of enhancing tissue dispersed among normal tissue.

### Angiogenesis in tumor vessels

The malignant lesions in their early stage are merely a few millimeters in diameter which are commonly vascular. Depend on the diffusion and vessel growth, they need nutrition. The structure of the vessels in a tumor differs from the normal vessel structure. The vasculature in tumors is heterogeneous, the capillaries are coarse, their walls have lots of openings, and the vessels are more fragile. These disorders occur because of the rapidly growing, which make the capillaries in the tumor leaky. The high permeability of the vessels plays a significant role in DCE-MRI, since they let the fast diffusion of contrast agent to the tumor [18].

### 2.3. DYNAMIC CONTRAST-ENHANCED MAGNETIC IMAGING OF THE BREAST

The most common imaging modality to detect breast cancer is mammography (X-ray); however, its sensitivity reduces significantly in one screening series from 80% to 30% by increasing breast density, which is quite common in younger patients [27]. Therefore, MRI has become the preferred modality for high risk patients, especially with high breast density and history of LCIS or DCIS [18, 27].

As Figure 2.6 shows, to perform breast MRI, the woman usually lies face down, with her breasts positioned through special openings in the table for breasts. The breast positioning and her movements are checked by the technologist through a window. Then patient usually enters a tunnel with magnetic field which creates pulses of radio waves sending from a scanner. Once the radio waves hit the nuclei of atoms in body cells, they send out radio signals. The received signals are converted into an MR image breast part.

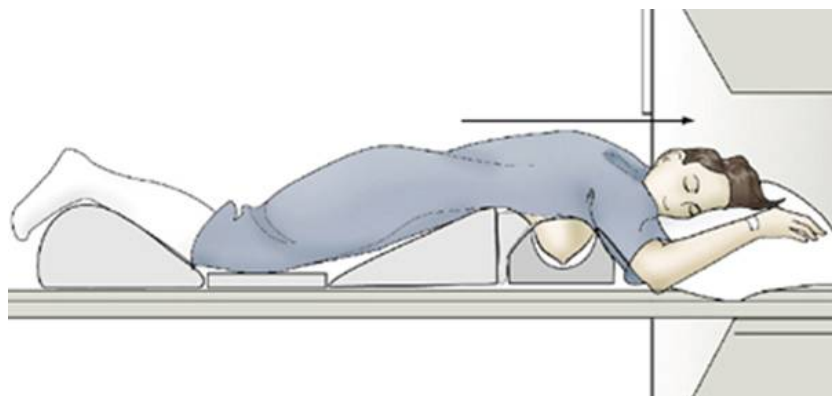


**Figure 2.6:** Patients position while breast MRI is performed. During the breast MRI, the patient usually lies face down, with her breasts positioned through openings in the table (Figure taken from [cornell.edu](http://cornell.edu)).

In comparison to two-dimensional X-ray images, MRI is a three-dimensional imaging technique that has the ability to produce cross-sectional images with a high spatial resolution of about 1 mm. Due to the high sensibility, breast MRI has drawn significant attention in recent years. This high sensitivity is achieved due to the use of contrast agents, such as *gadolinium - diethylenetriamine-pentaacetic acid* (Gd-DTPA) with regard to vascular changes in the tissue (described in 2.2) which causes intensity enhancement (see Figure 2.7). It first increases the vascularity resulting in an increase in contrast agent intake as it is in the blood. Then, it results in vessel permeability as it leads to increased leakage of contrast agent in the tumor. The signal enhancement level seen on T1-weighted images appertains to a number of factors, including tissue perfusion, capillary permeability to the contrast agent, the volume of the extracellular leakage space, and the contrast agent dose [18]. Furthermore, it also depends on the phase of the menstrual cycle in premenopausal women. The second week of the menstrual cycle is the recommended time to perform breast MRI, because of the hormonal responsiveness of the breast tissue [28].

The Breast Imaging-Reporting and Data System (BI-RADS) [26], published by the American College of Radiology (ACR) [29], is a lexicon made to help standardizing radiologists' report on breast MRI findings [5].

### 2.4. PATHOPHYSIOLOGY OF LESION CHARACTERISTICS

Benign and malignant lesions vary in morphology, enhancement intensity and kinetics. For example, round or oval shapes of masses are highly indicative of benignity, since ill-defined or indistinct

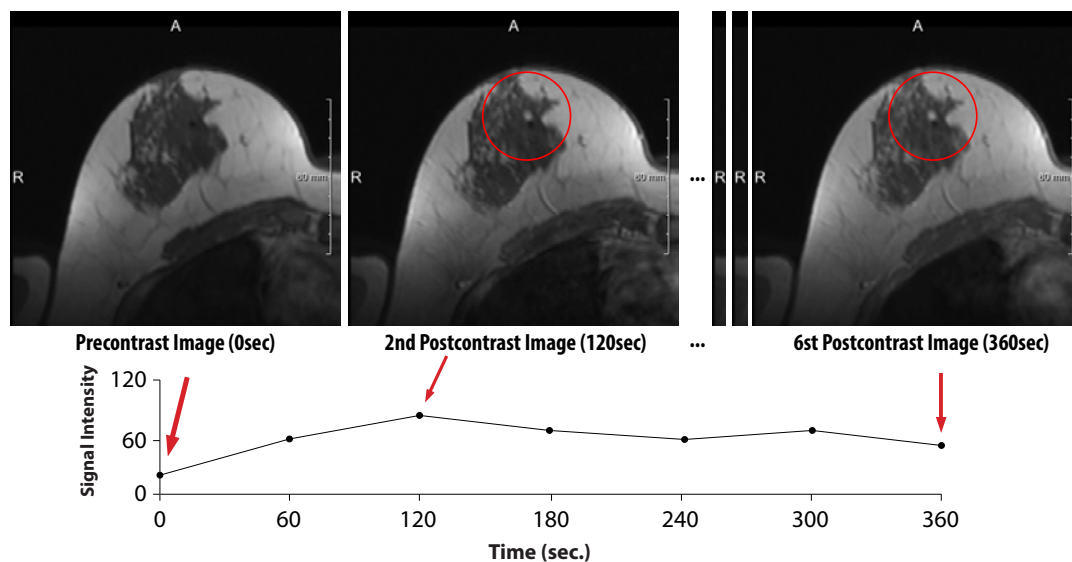


**Figure 2.7:** Images acquired from DC-MRI several time intervals before and after the injection of contrast agent. The curve shows the intensity-time diagram for the value of a single voxel of the DC-MRI sequence on top. **The most left** image shows image before injection, **the rest to the right** show the increase in signal intensity after injection of the contrast agent.

margins indicate lesion infiltrating surrounding tissue. Based on qualitative analysis, in malignant tissue, the signal intensity peaks early compared with normal tissue mainly because of increased vascularisation and leakiness of tumor vessel [5]. Conventional fibroglandular tissue commonly exhibits a low level of enhancement at an early time after contrast administration, and then a gradual, faint enhancement over time. In the following, more details will be discussed regarding these features.

#### 2.4.1. MORPHOLOGICAL FEATURES

Morphologically, lesions can be categorized into focus/foci, mass, and non-mass-like enhancements.

- **Focus** is a breast lesion with the size smaller than 5 *mm*.
- **Mass** is a 3D space-occupying lesion smaller or equal to 5 *mm*. It is characterized by shape (round, oval, lobulated, irregular), rim (smooth, irregular, spiculated) (see Figure 2.8), and internal mass enhancement characteristics (homogeneous, heterogeneous, rim enhancement, dark internal septations, enhancing internal septations, and central enhancement).
- **Non-mass-like** enhancement can be characterized by the distribution pattern (focal, linear, ductal, segmental, regional, multiple regions, and diffuse) and internal characteristics (homogeneous, heterogeneous, stippled/punctate, clumped, reticular/dendritic) (see Table 2.1). Further categorizations are whether the lesion is symmetric or asymmetric between both breasts, lymphadenopathy, and invasion of pectoralis muscle [28].

Margin assessment is one of the most important features in characterization of a breast mass with a high positive predictive value (PPV). Masses with smooth rims highly implies benign lesion. As reported in [32, 33], 97% to 100% of masses with smooth rims were benign. Poorly enhanced lobulated masses and the one with non-enhancing septations also suggested benignity.

A homogeneous internal enhancement pattern has a high predictive value for a benign lesion such as a fibroadenoma. However, the pattern can also be a presentation of invasive cancer [28].

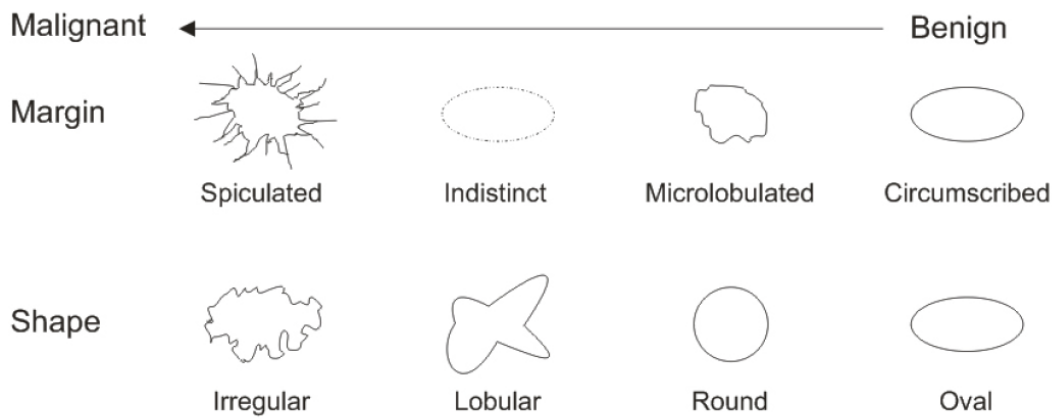


**Figure 2.8:** Schematic illustration of morphological features exhibited by mass lesions (Figure taken from [30])

<b>Mass-like Enhancement</b>	Shape	Round, Oval, Lobulated, Irregular
	Margin	Smooth, Irregular, Spiculated
	Internal Enhancement Characteristics	Homogeneous, Heterogeneous, Rim Enhancement, Dark Septations, Enhancing Septations, Central Enhancement
<b>Non-Mass-like Enhancement</b>	Distribution	Focal Area, Linear, Ductal, Segmental, Regional, Multiple Regions, Diffus
	Internal Enhancement Pattern	Homogeneous, Heterogeneous, Stippled/Punctate, Clumped, Reticular/Dendritic

**Table 2.1:** Lesion's morphology according to the BI-RADS™ standard. A mass is characterized by shape, rim, and the internal enhancement characteristics. A non-mass-like enhancement is characterized by the overall distribution pattern of enhancement and the internal enhancement characteristics (Figure taken from [28, 31]).

In non-mass-like enhancement the area is neither a mass nor a blood vessel, thus the enhancement pattern is distinct from normal surrounding breast parenchyma and there is no space-occupying effect. These lesions include DCIS, ILC, mastopathic changes (focal adenosis), and fibrocystic changes. In these cases, the focal area is defined as a single, small, and confined abnormal enhancing area which occupies less than 25% of a breast quadrant. It varies from a focus, which has the size of less than 5 mm and usually has fat or normal glandular tissue interspersed between the abnormally enhancing components, except when it is a focal area of homogeneous enhancement [28]. Based on quantitative findings, about 50% of benign lesions with a non-mass-like enhancement, present a linear-enhancement distribution [34].

In many cases, the enhancements form two or more large volumes of tissues, not conforming to ductal distribution are separated by normal tissues or fat appearing throughout the fibroglandular tissue of the breast. Although multi-centric benign carcinoma, including IDC or ILC, may also exhibit such appearance, they cannot simply be categorized as benign [28].

Enhancement's symmetry is also can be exploited to further characterizations. Mirror-image like symmetric enhancement in both breasts in any distribution is highly suggestive of benign changes [28].

There are several geometrical and morphological features which are commonly used among researchers as shape descriptors: volume ratio, surface area, compactness, normalized radial length (NRL) mean, sphericity, NRL entropy, NRL ratio, convex hull, and roughness. More detailed descriptions of them can be found [35–37]

### 2.4.2. KINETICAL FEATURES

In this study the main focus is merely on morphological features of enhancements. Although studies have shown that including kinetic data on dynamic contrast-enhanced imaging and diffusion-weighted MR imaging in addition to morphological characteristics, exhibits a higher diagnostic accuracy in the characterization of breast lesions [10].

In terms of kinetic information, the dynamic contrast-enhanced (DCE) curve is characterized by the enhancement of the tumor due to the contrast agent, mainly by considering the mean gray values of each tumor region and how it develops over time [10]. The radiologist can assess the enhancement kinetics qualitatively by paging through the sections and time points, observing factors, including the initial enhancement, the presence or lack of a peak enhancement, and the subsequent delayed enhancement. However, this method depends mainly on the experience of specialist [38].

#### Kinetic Enhancement Curve Assessment

As can be seen in Figure 2.9, enhancement kinetics curve features can be separated in two phases: the *initial* phase and the *delayed* phase. In the **initial phase**, the features are "*slow*", "*medium*", or "*fast*" and in the delayed phase, there are "*persistent*", "*plateau*" or "*washout*". A kinetic curve showing washout or plateau after reaching the peak within 2 – 3 minutes is commonly observed in *invasive breast cancer*; a kinetic curve showing persistent enhancement, continuing throughout the entire time period is commonly observed in *benign diseases* [6].

This trend is not always reliable experimentally, especially for non-mass-like enhancements. It may be used with confidence in differential diagnosis only in lesions showing rapid enhancement and washout pattern. Therefore, an analysis of both morphology and kinetic curve should be taken into account in the interpretation [28].

### 2.4.3. TEXTURAL FEATURES

From the radiography point of view, texture is a repeating pattern of local variations in image intensity, and is characterized by the spatial distribution of intensity levels in a particular area. Haralick et al. [39] defined ten co-occurrence matrix (GLCM) texture features, including energy, maximum probability, contrast, homogeneity, entropy, correlation, sum average, sum variance, difference average and difference variance. These features consider the spatial relationship of pixels/voxels in gray-level and are generally used to characterize lesions without considering the mass factor [35, 37].

#### GRAY LEVEL CO-OCCURRENCE MATRIX

To give a uniform definition of gray-level co-occurrence matrix for both 2D and 3D data. Consider an image (either 2D or 3D) which is first re-binned to  $G$  (a positive integer) gray levels. Displacement vector  $d$  describes the difference of spatial locations of two voxels.

For 2D images, the possible spatial relations of a voxel with 8 neighboring voxel-pairs in 4 independent directions ( $\theta = 0^\circ, 45^\circ, 90^\circ, 135^\circ$ ) are shown in Figure 2.10(left). In 3D images, the displacement vector  $d$  can still be decomposed into a norm-1 distance  $d$  and a direction, which are specified by two angles: azimuth  $\phi$ , and zenith  $\theta$  (Figure 2.10(right)). In 3D space, there are totally

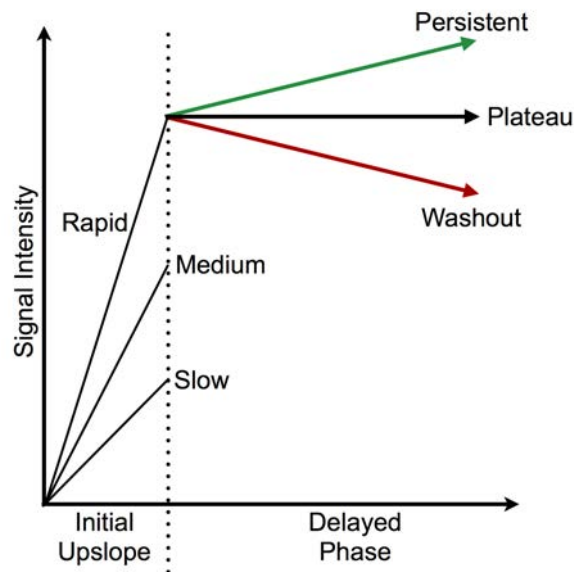


**Figure 2.9:** Contrast Enhancement Kinetic Curves. The contrast uptake curves can be used in breast lesion diagnosis. Ideally, there is no early phase enhancement and persistent delayed phase in normal fibroglandular tissue while it has low variable enhancement. Observing a washout behavior in the delayed phase usually means invasive cancers. Normally, benign lesions have persistent kinetics in the delayed phase, but they can also show washout or plateau kinetics (Figure taken from [38]).

26 neighboring voxel-pairs in 13 independent directions [40].

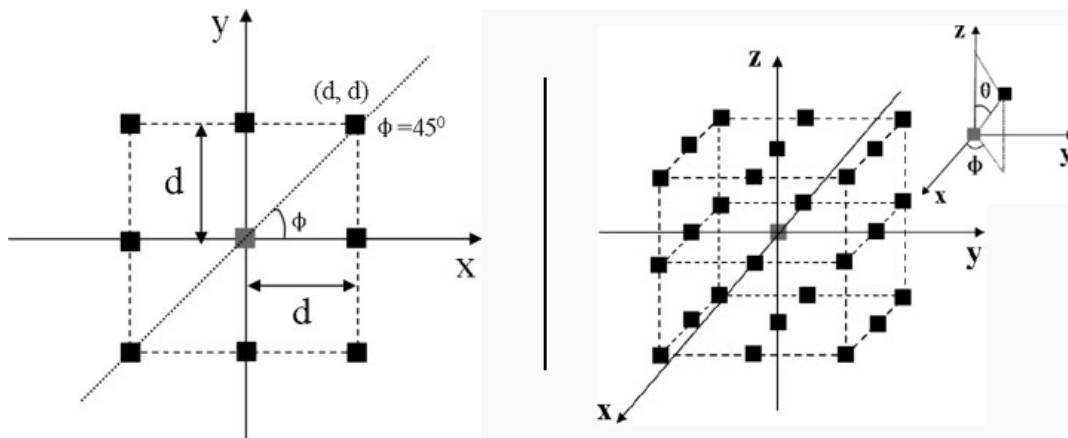


**Figure 2.10:** Texture features based on the spatial relations of a pair of voxels. **Left:** Spatial relations of a pair of voxels in 2D. For a particular voxel (gray), it has 8 neighboring voxels (dark) of norm-1 distance  $d$  in 4 independent directions. **Right:** Spatial relations of a pair of voxels in 3D. For a particular voxel (gray), it has 26 neighbors (dark) of norm-1 distance  $d$  in 13 independent directions (Figure taken from [40]).

For an image of  $G$  gray levels, the  $G \times G$  gray level co-occurrence matrix  $P_d$  for a displacement vector  $d$  is defined as follows:

The entry  $(i, j)$  of  $P_d$  is the number of occurrence of voxel-pair of gray levels  $i$  and  $j$  whose spatial locations are a vector  $d$  apart. After normalization by the total counts, the entry  $(i, j)$  of  $P_d$ , denoted as  $p(i, j)$ , represents the (empirical) probability of occurrence of voxel pair of gray levels  $i$  and  $j$  whose spatial locations are a vector  $d$  apart. In this definition, the co-occurrence matrix  $P_d$  is a function of the displacement vector  $d$ .

Now, a set of texture features defined by Haralick et al. [39] can be extracted from the co-

occurrence matrix to quantify the spatial dependence of gray-level values. Equation 2.1 shows more detailed calculations of several features such as Angular Second Moment, Contrast, Correlation, Sum of Squares, Inverse Difference Moment, Sum Average, Sum Variance, Sum Entropy, Entropy, Difference Variance, and Difference Entropy in 2D images. The definitions and explanations of the complete set of features can be found in [39].

$$\begin{aligned}
 \text{Angular Second Moment} &= \sum_i \sum_j \{p(i, j)\}^2 \\
 \text{Contrast} &= \sum_{n=0}^{N_g-1} n^2 \left\{ \begin{array}{l} \sum_{i=1}^{N_g} \sum_{j=1}^{N_g} p(i, j) \\ |i - j| = n \end{array} \right\} \\
 \text{Correlation} &= \frac{\sum_i \sum_j (i, j) p(i, j) - \mu_x \mu_y}{\sigma_x \sigma_y} \\
 \text{Sum of Squares} &= \sum_i \sum_j (i - j)^2 p(i, j) \\
 \text{Inverse Difference Moment} &= \sum_i \sum_j \frac{1}{1 + (i - j)^2} p(i, j) \\
 \text{Sum\_Average} &= \sum_{i=2}^{2N_g} i p_{x+y}(i) \\
 \text{Sum Variance} &= \sum_{i=2}^{2N_g} (i - \text{Sum\_Entro})^2 p_{x+y}(i) \\
 \text{Sum Entropy} &= - \sum_{i=2}^{2N_g} p_{x+y}(i) \log\{p_{x+y}(i)\} \\
 \text{Entropy} &= - \sum_i \sum_j p(i, j) \log p(i, j) \\
 \text{Difference Variance} &= \text{variance of } p_{x-y} \\
 \text{Difference Entropy} &= - \sum_{i=0}^{N_g-1} p_{x-y}(i) \log\{p_{x-y}(i)\}
 \end{aligned} \tag{2.1}$$

(Equations are taken from [39])

## 2.5. RELATED WORK

Unlike most previous works which have put emphasis on kinetical and textural features analysis for mass lesions, this study focused merely on investigating the morphological features efficacy among non-mass-like enhancements in breast MRI lesion diagnosis [37].

Conventionally in most of the existing scientific works, the evaluation is done on diagnostic impressions generated by visual examination of morphological features and contrast enhancement

kinetics using descriptors defined in the BI-RADS (Breast Imaging-Reporting and Data System) lexicon [26, 41].

Current commercially available computer-aided diagnosis (CAD) systems are specialized for automated detection and diagnosis of mass lesions that are applicably characterized by shape and kinetic descriptors according to the BI-RADS lexicon [10]. Such systems only depict the suspicious lesion area using intensity level threshold filter in addition to some enhancement kinetic diagnosis [42–44]. Further morphological analysis and the final diagnostic impression have to be done by the radiologist which depend heavily on his/her level of experience [37].

During the enhancement diagnosis of malignant non-mass lesion, numerous cases often do not show the expected wash-out pattern in enhancement kinetics. Therefore, this very advantageous diagnosis pattern of mass lesions has a confined diagnostic value for non-mass lesions [45, 46]. Additionally, poorly defined boundaries in non-mass lesions bring more hardship in morphological analysis [37, 43, 47].

Plevritis et al. stated that, by combining dynamic enhancement kinetic data and morphologic characterization, more accurate assessment is acquired rather than either method alone. The reason is that data acquisition from each characterization is based on a separate pathophysiologic mechanism [48, 49]. Therefore, usually analyzer systems characterize the morphological features along with their enhancement kinetics after applying automated or manual segmentation on the lesion. As the final step, they build a classifier based on the combination of those features which yield the highest diagnostic performance [37].

Newell et al. [37] developed methods to characterize the morphology, enhancement kinetic and textural features of both mass and non-mass lesions to investigate the diagnostic performance to differentiate between malignant and benign lesions. For each mass 8 shape/ margin parameters (volume, surface area, compactness, normalized radial length (NRL) mean, sphericity, NRL entropy, NRL ratio and roughness) and 10 enhancement texture features were obtained. Compactness is defined as the ratio of the square of the surface area to the volume of the lesion. This index for a sphere is the lowest and for an irregular undulating shape, such as a speculated lesion, is higher. NRL is defined as the Euclidean distance from the object's center of mass to each of its contour pixels [35, 50].

They pointed out that, since there were no clearly defined boundaries for non-mass lesions, these shape parameters could not be reliably analyzed [37]. For the non-mass-like enhancement, only the texture parameters were considered. To build a diagnostic model they used an artificial neural network (ANN) machine learning technique. For the masses, they reached an area under the ROC curve (AUC) of 0.87 in differentiating between malignant and benign lesions. The kinetic parameter reached a comparable AUC of 0.88. The combined morphological and kinetic features improved the AUC to 0.93, with a sensitivity of 0.97 and a specificity of 0.80. For non-mass-like enhancement, the texture analysis achieved an AUC of 0.76 and the kinetic parameter reached an AUC of 0.59, with a low added diagnostic value [37].

Nie et al. [35] investigated the feasibility of using quantitative morphology/texture features of breast lesions for diagnostic prediction. They carried out the automated lesion segmentation, quantitative feature extraction, including eight morphological parameters and 10 GLCM texture features, diagnostic feature selection using artificial neural network (ANN), and lesion classification. They achieved the area under the ROC curve of 0.86 and AUC of 0.82.

Hoffmann et al. [10] present a novel technique for establishing the automated diagnosis of non-mass-enhancing lesions. Extracting both morphological and kinetic features is being done in an automated step and use them for lesion detection. In addition to kinetic features, they apply Zernike velocity moments to acquire the spatio-temporal behavior of the lesions. The evaluation is done by

SVM automated classification quantitatively and qualitatively. They came to the conclusion that kinetic features are more discriminative in the case of non-mass-like enhancing lesions followed by the morphological ones.

This study only focuses on morphological feature extraction using the novel sphere packing technique. More details will be described in the upcoming chapter.

# 3

## MATERIALS AND METHOD

### 3.1. MATERIALS

#### PATIENTS DATASET

For this study, a data set of coronal T1-weighted MR breast volumes from 86 different patients – who were diagnosed having non-mass lesions by MRI scan – were collected within the years 2003 and 2009 from the Radboud University Nijmegen Medical Center in the Netherlands. All the patients were scanned in prone position. The age of screened women ranged from 23 to 76 years ( $45.84 \pm 11.97$  on average). Breast MRI examinations were performed on either a 1.5 or 3 Tesla Siemens scanner (Magnetom Vision, Magnetom Avanto and Magnetom Trio), with a dedicated breast coil (CP Breast Array, Siemens, Erlangen). Clinical imaging parameters varied; matrix size:  $256 \times 128 \times 256 \times 96$ ; slice thickness: 1.3 mm; slice spacing: 0.625 - 1.25 mm; flip angle: 8, 20 or 25 degrees; repetition time: 7.5 - 9.8 ms; echo time: 1.7 - 4.76 ms.

#### GROUND TRUTH

In total 106 non-mass lesions of different types (38 benign and 68 malignant) were examined. The region of interest (ROI) of cases were provided by an experienced radiologist as binary spherical masks in a separate dataset. As [Figure 3.1](#) shows, by overlaying the masks on original MR image, I was able to focus only on the area of breast in which there are lesions and therefore, a more precise segmentation could be achieved. [Section 3.3.2](#) describes the segmentation process in details.

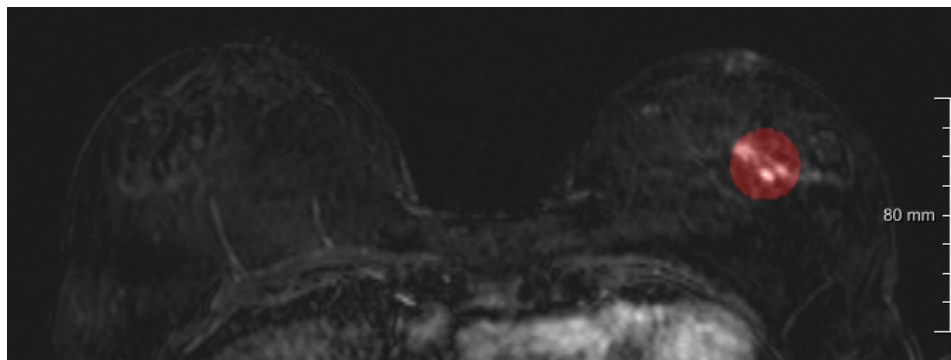


**Figure 3.1:** The breast MRI with an overlay provided by the radiologist. The ROI mask by radiologist (the red overlay) can simplify finding the lesion position and focus the segmentation on the specific area with the lesion

It should be mentioned that, the MR scans in the dataset are not ready yet to be processed since there might be some motion artifacts between different MR sequences. In order to get a better segmentation, the probable motion must be corrected. Motion artifacts play an important role in correct diagnosis of non-mass-enhancing lesions [10]. This pre-processing step is described in [Section 3.3.1](#) with more details.

### 3.2. METHOD OUTLINE

In this study, the processing pipeline can be briefed into three main steps as shown in [Figure 3.2](#).

1. **Preprocessing:** this step commences with applying motion compensation on DC-MRI data to remove most of the artifacts from images acquired at different time intervals. Then, a semi-automatic mean shift segmentation is performed on the data to extract the lesion volumetric shape from the image.
2. **Feature extraction:** in this step the 3D lesion volume acquired from the last step is filled with spheres using sphere packing algorithm. The internal spheres data, including center coordinates and their radius is obtained to generate further features. Before using internal spheres data, the coordinate values of spheres have to be normalized and rescaled to the unit length. Next, three kinds of features are extracted, including volume-radius histogram, 3D spherical shape histogram, and graph topological features which will be defined in the following section. Furthermore, in this very step, the Zernike invariants are calculated directly from the lesion 3D volume.
3. **Classification:** all the acquired features are combined linearly as an all-inclusive feature vector to be provided to the classifier. The, Random forest classifier is trained using a dataset of the feature vectors from all the sample lesions. Finally, the evaluation is done using 10-fold cross validation method.

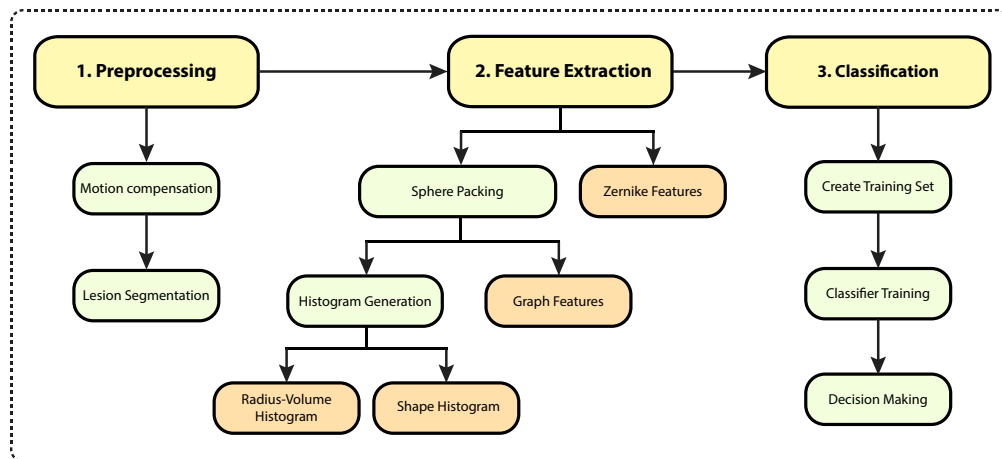


**Figure 3.2:** The proposed lesion classification process workflow. From left to right, **preprocessing** includes motion compensation and semi-automatic mean shift segmentation. **Feature extraction** consists of sphere packing of lesion, extracting two kinds of histogram features, graph topological features and Zernike features. **Classification** contains combining all sample dataset and training the random forest classifier to differentiate the lesion type between benign and malignant.

### 3.3. PRE-PROCESSING

#### 3.3.1. MOTION COMPENSATION

In MR imaging, to observe the uptake of the contrast agent, an MR scan is acquired prior to the injection, followed by a dynamic sequence of MR scans. The uptake rate can be acquired from the difference between pre and post-contrast images. However, this might not be so easy because of mis-registrations, caused by patient motion. In particular, motions such as respiratory motion [51], muscle relaxation, and coughing during image acquisition [52]. Often patient motions can reduce the interpretability of breast MRI; however, for scans with strong motion, it might be necessary to recall the patient for a repeated scan. In this work, a fully automated tool, based on image-processing introduced by Wang et al. [52], is used to detect and quantify motion for unambiguous scan quality evaluation.

Figure 3.3 shows the blurred maximum intensity projections (MIPs) caused by motion between pre-contrast time ( $t_0$ ) and following post-contrast sequences ( $t_1 \dots t_n$ ), as they are based on the subtraction of  $t_0$ .

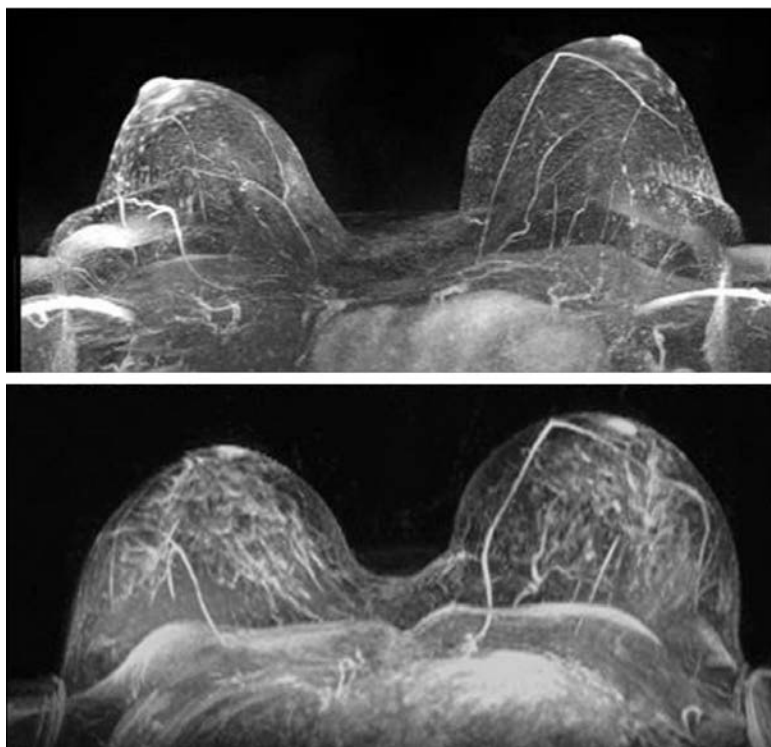


**Figure 3.3:** Maximum intensity projection images of the difference image  $t_1 - t_0$  of the same patient. **Top**, represents a case without motion. **Bottom** represents a case with moderate motion in both breasts (Figure taken from [52])

To correct the motion artifacts of the used dataset, I utilized the motion compensation technique presented by Wang et al. [52]. As can be seen in Figure 3.4(a), motion artifact quantification between  $t_0$  and  $t_1$  is done by detecting the prominent edges delineating the boundary contours of parenchyma, skin and pectoral muscle in both  $t_0$  and  $t_1$ . Using a fully automatic breast segmentation technique by Wang et al. [53], edge detection enclosed only to the breast internal region and irrelevant motion that occurred in the thorax, such as heart, lung or liver, was excluded from processing. Then, the Canny edge detection algorithm using a Gaussian smoothing kernel is adopted only on the 10 central slices of scan instead of the entire volume to boost up the processing speed.

According to Wang et al. [53], in order to measure the distance between two sets of detected

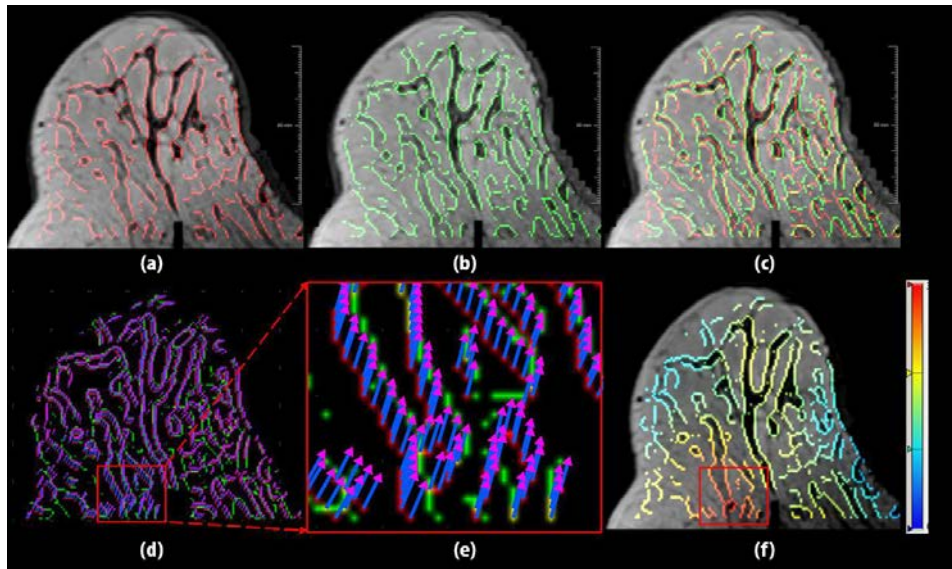


**Figure 3.4:** Motion quantification visualization for a breast, blurry MRI scan. Detection scheme: (a) detected edges in  $t_0$  (red contours); (b) detected edges in  $t_1$  (green contours); (c) detected edges in  $t_1$  (green) overlaid with edges in  $t_0$  (red); (d) visualization of deformation vectors showing correspondence between edges in  $t_0$  and  $t_1$ ; (e) magnified view of the deformation vectors in the red square in (d); (f) color map of deformation magnitude (displacement in mm) calculated for edge voxels in  $t_0$ , red correlates with strong motion (Figure taken from [52]).

edges, a fast and non-rigid registration method with a volume preservation constraint to register  $t_1$  (moving image) onto  $t_0$  (fixed image) is employed (see Figure 3.4(d)&(e)). Then, a 3D deformation vector representing the occurred motion direction and magnitude (strength), was assigned to each voxel in  $t_0$ . Next, the magnitude of those vectors for all the edge voxels are saved to a list, which encoded the motion strength along edges (see Figure 3.4(f)). A set of features is extracted from the corresponding histogram. Finally, Random Forest (RF) classifier makes decision whether a test case had moderate or severe motion artifact.

Up till this point the motion artifact is removed from the MR sequences, therefore, the segmentation on the subtraction image can be done easier with more precision on boundaries of the lesions.

### 3.3.2. LESION SEGMENTATION

For this step, a semi-automatic 3D mean shift segmentation (will be discussed in Section 3.3.2) is adopted to separate the lesion from its surrounding tissue. I developed a 3D extension of the 2D EDISON framework [54, 55] to process 3D volumetric data. Taking advantage of the lesion binary masks, provided by the specialist, the search area for the lesion is confined within the mask region (see Figure 3.1). Restricting the examination area speeds up the mean shift segmentation, since this algorithm is very slow processing large volumetric images [56].

Figure 3.5 illustrates each step of the segmentation process. First, a bounding box of area defined by the mask is separated from the subtraction image of  $t_1 - t_0$  (Figure 3.5(a)). Next, mean shift segmentation is applied, which decomposes the enhancement area into an arbitrary number of clusters with various intensity values (Figure 3.5(b)). By mapping the intensity values of the clusters into the uniform range, applying threshold filter and keeping only the clusters above the threshold band value, the result will be a 3D binary volume of the enhancement (Figure 3.5(c)).

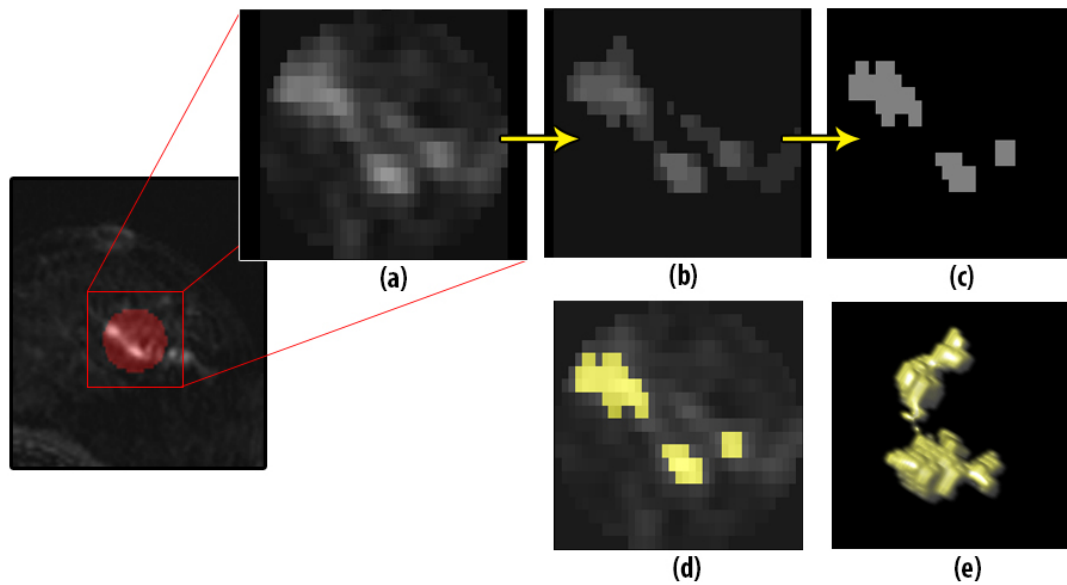


**Figure 3.5:** Lesion segmentation using mean shift algorithm and applying threshold. (a) the enhancement area from subtraction MR image defined by the mask; (b) the multi-clustered result of mean shift segmentation; (c) segmentation result after applying threshold filter with a manual value; (d) an overlay of the segmentation result over enhancement area; (e) the 3D illustration of the lesion segmented volume.

### MEAN SHIFT ALGORITHM

The mean shift algorithm is a powerful unsupervised clustering technique introduced in 1975 by Fukunaga and Hostetler [57]). The algorithm detects modes in the gradient of a probability density function in an iterative scheme and represents a general non-parametric mode finding/clustering procedure. In contrast to the classic K-means clustering approach [58], there are no embedded assumptions neither about the shape of the distribution nor the number of modes/clusters [59].

Mean shift has been used for image segmentation by seeking the modes in a feature space composed of intensity/color in addition to spatial information [60]. The applications of the mean shift algorithm are in various fields, including clustering, segmentation, and filtering. This algorithm can provide consistently good results [56] (see Figure 3.6).

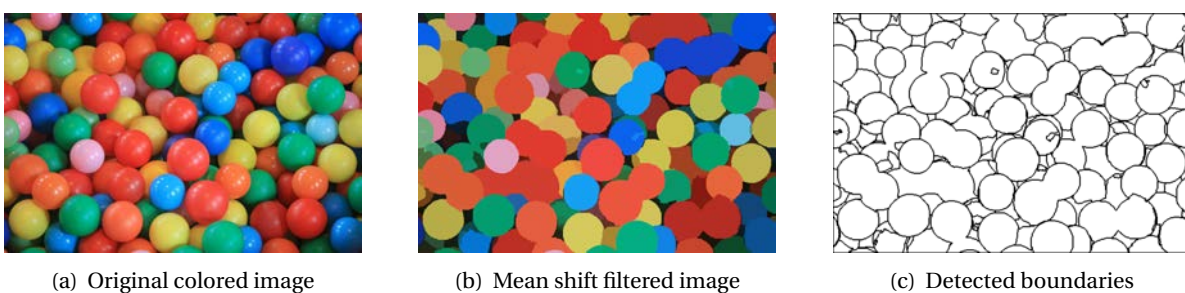


**Figure 3.6:** Mean shift segmentation applied on a colored image. The results are acquired using EDISON software [54] (Ball pool photo taken from [rgbstock.com](http://rgbstock.com))

As mentioned earlier, the mean shift technique detects modes in a probability density function based on the Parzen Density Estimate [57]:

$$\hat{f}_{K_S}(x) = \frac{1}{Nh^d} \sum_{i=1}^N K_S\left(\frac{x-x_i}{h}\right) \quad (3.1)$$

$N$  equals the number of  $d$ -dimensional vectors  $x_1 \dots x_N$ . The parameter  $h$  is the window radius of the used kernel  $K_S$ . In the field of image segmentation, each feature vector is composed of the spatial information of each pixel/voxel and the corresponding color/intensity information in the range domain of dimension one or more. The multivariate mean shift vector in the point  $x$  is given by [55]

$$m_K(x) = \frac{\sum_{i=1}^N x_i K\left(\frac{x-x_i}{h}\right)}{\sum_{i=1}^N K\left(\frac{x-x_i}{h}\right)} - x \quad (3.2)$$

For the uniform kernel  $K_U$  the calculation of the multivariate mean shift vector (Equation 3.2) becomes an average of vector differences. It can be shown that the mean shift vector is proportional to the normalized density gradient estimate [55].

$$m_K(x) = \frac{1}{2} h^2 c \frac{\nabla \hat{f}_{K_E}(x)}{\hat{f}_{K_U}(x)} \quad (3.3)$$

where  $c$  is the corresponding normalization constant and  $K_E$  is the radially symmetric Epanechnikov kernel given by

$$K_E(x) = \begin{cases} \frac{1}{2} c_d^{-1} (d+2) (1 - \|x\|^2) & \text{if } \|x\| \leq 1 \\ 0 & \text{otherwise} \end{cases} \quad (3.4)$$

with  $c_d$  being a normalization constant. To ensure the isotropy of the feature space, a uniform color space, such as the  $L^* u^* v^*$  is typically used. In the case of gray-value images, the  $L^*$  component is only used. To account for different spatial and tonal variances it is reasonable to choose a kernel window of size  $S_h = S_{h_s, h_r}$  with differing radii  $h_s$  in the spatial and  $h_r$  in the range domain [56].

The mean shift vector is designed to be aligned with the local gradient estimate. Therefore, it can be shown that by successive computation of Equation 3.2 and shifting the kernel window by  $m_K(x)$ , the mean shift procedure is guaranteed to converge to a point with zero gradient, i.e. to a mode corresponding to the initial position (see (Figure 3.7(c))). Modes that are closer than  $h_s$  and  $h_r$  are grouped together. For segmentation purposes, to each pixel/voxel is then assigned the color/intensity value of the corresponding mode (see (Figure 3.7(d))). Furthermore, regions with less than some pixel/voxel count  $M$  might be optionally eliminated [56].

The mean shift procedure is hence an effective algorithm for mode seeking in a density distribution without prior calculation of the distribution itself [56].

### 3.4. SPHERE PACKING

Sphere packing is filling an object with a set of non-overlapping spheres. It has diverse applications in a various fields of scientific and engineering, including automated radiosurgical treatment plan-

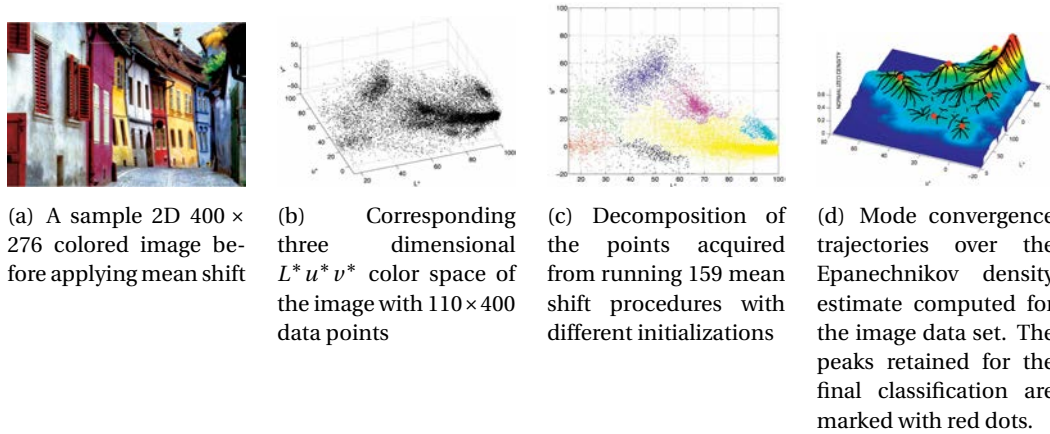


**Figure 3.7:** Example of a 2D feature space analysis using mean shift (Figure taken from [55])

ning, investigation of processes such as sedimentation, compaction and sintering, powder metallurgy for 3D laser cutting, cutting different natural crystals, and so forth. Polydisperse sphere packing is a new and promising data representation for several fundamental problems in computer graphics and virtual reality such as collision detection and deformable object simulation. Polydisperse means that the radii of the spheres can be an arbitrary real number [61].

Here, it is tried to broaden the usages of sphere packing algorithm and utilize it to classify an object (which here is the breast lesion), using its shape features. In this work, an extended version of sphere packing algorithm, called *Protosphere*<sup>1</sup> a GPU-assisted prototype guided sphere packing algorithm is used. The Protosphere is inspired by machine-learning techniques and uses a prototype-based greedy choice to extend the idea of Apollonian sphere packing [61]. For an arbitrary given object, it starts with the largest possible sphere that fits in the object. It iteratively inserts new spheres, under the constraints that first, they must not intersect the already existing ones and second, they be completely contained inside the object [16].

The Protosphere algorithm was introduced in 2010 by Weller and Zachmann [16] and has got extended by Teuber et al [61]. It is able to efficiently compute a space filling sphere packing for arbitrary container objects and object representations (polygonal, NURBS, CSG, etc.) under the only precondition that it must be possible to compute the distance to the object's surface from any point. This packing is achieved by successively embedding the largest possible sphere into the object [61].

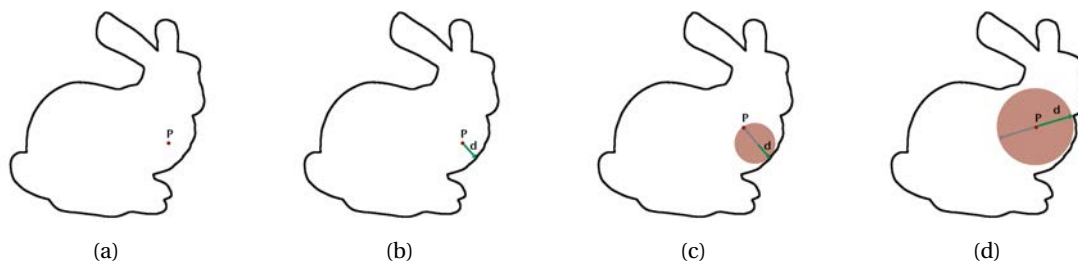


**Figure 3.8:** Sphere packing prototype convergence visualization. (a) placing the prototype  $P$  randomly inside the object; (b) calculating the closest point on the surface and the distance  $d$ ; (c) moving  $P$  away from the closest point; (d) repeating this until the prototype converges (Figure taken from [61]).

Consider the largest sphere  $s$  inside  $O$ , the surface of a closed and simple object in 3D. Obviously,

<sup>1</sup>Protosphere: A GPU-Assisted Prototype Guided Sphere Packing Algorithm for Arbitrary Objects  
<http://cgvr.cs.uni-bremen.de/research/protosphere> [Accessed on 6 September 2015]

$s$  touches at least four points of  $O$ , and there are no other points of  $O$  inside  $s$ . This implies that the center of  $s$  is a *Voronoi Node (VN)* of  $O$ . Consequently, the *Apollonian* filling can be formulated as an iterative computation of the VNs of the object's hull  $O$  plus the set of all spheres existing so far. To compute the *Voronoi Diagram (VD)* they approximate the VNs by placing a single point, *the prototype*, inside the object and let it move away from the object's surface in a few iterations (see [Figure 3.7](#)). By choosing a clever movement, the prototype converges automatically towards a VN (see [Algorithm 3.1](#)). The last step of the algorithm guarantees that, after each single step,  $p$  is still inside the object, because the entire sphere around  $p$  with radius  $\|p - q_c\|$  is inside the object.

Moreover, moving  $p$  away from the border, into the direction  $(p - q_c)$ , leads potentially to bigger spheres in the next iteration. Usually,  $\epsilon(t)$  denotes a cooling function that allows large movements in early iterations and only small changes in the later steps. This process is parallelized and uses a set of prototypes that are allowed to move independently instead of inserting just a single prototype, which might end up in a local optimum rather than of converging toward the global optimum.

---

**Algorithm 3.1** Sphere packing prototype converge
 

---

```

1: procedure CONVERGEPROTOTYPE (PROTOTYPE  $p$ , OBJECT  $O$ )
2:   place  $p$  randomly inside  $O$ 
3:   while  $p$  has not converged do
4:      $q_c = \arg \min \{ \|p - q\| : q \in \text{surface of } O \}$ 
5:     choose  $\epsilon(t) \in [0, 1]$ 
6:      $p = p + \epsilon(t) \cdot (p - q_c)$ 
7:   end while
8: end procedure

```

---

(Algorithm is taken from [61])

In order to apply sphere packing to the binary volumetric lesion segmentation ((see [Figure 3.9\(a\)](#))), at first, it is converted to a mesh geometric object (see [Figure 3.9\(b\)](#)), then I let Protosphere pack it with arbitrary number of spheres (here, 4000 is chosen as the maximum number of spheres inside any lesion object) (see [Figure 3.9\(c\)](#)). In the following section, a couple of advantageous shape features are elicited from the internal spheres to create a samples dataset for classifier.

### 3.5. NORMALIZATION

The mesh geometries, acquired from converting segmented lesions into geometric meshes, have various sizes. As a result, the sphere coordinates from packing step also have arbitrary scales and positions in the 3D space. As the embedded sphere coordinates are going to be used in generating feature vectors for classifier's dataset, their values should be in equal range. Therefore, the normalization of the size and coordinates of the spheres before feature extraction is required for them to be represented in a canonical coordinate system. The aim of the normalization step is to guarantee the fact that same feature can properly be extracted from the same 3D object in any scale, position and orientation [62].

Generally, there are two schemes to realize such a *per-model-based* normalization [63] for 3D objects:

1. The normalization technique to find a canonical coordinate frame based on methods similar to the Principle Component Analysis (PCA), also referred to as pose estimation or pose registration.
2. The invariance-based technique to define and extract feature descriptors that possess the in-

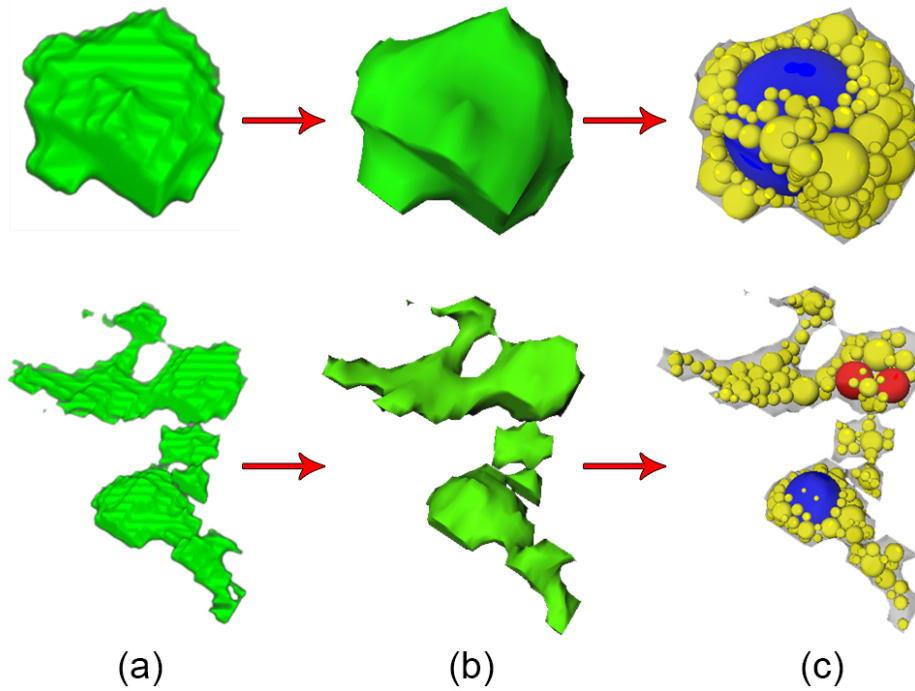


**Figure 3.9:** Sphere packing of the lesion 3D volume.

**Top** shows an example of benign lesion. **Bottom** shows an example of malignant lesion. **(a)** is the binary volumetric segmented of the lesion; **(b)** is converted lesion volume into a 3D mesh geometry; **(c)** is the lesion packed with 200 spheres (the spheres color is size based and is only for better differentiation in visualization).

herent invariance characteristics, so as not to change under any rigid transformations. The invariance-based approaches have been accorded increasing weight in recent research because of their robustness and simplicity [62].

In general, to guarantee the descriptive power and robustness of the feature representations, canonical coordinate normalization, such as alignment and scaling is a necessary step before invariant feature extraction [62].

In this study, the *scaling by overall maxima* method is used to normalize the spheres components ( $x$ ,  $y$  and  $z$  positions plus *radius*) in a way that their range remains between zero and one disregarding the alignment. [Algorithm 3.2](#) shows the normalization steps in pseudocode. At first, the maximum and minimum values of all the components are calculated along with their difference ( $diff = max - min$ ). Next, their minimum value of components is shifted to zero by adding the absolute value of minimum to all the position components. Then, via dividing each component ( $x$ ,  $y$  and  $z$  positions plus *radius*) by the difference value, the range of all components is being scaled down to between zero and one.

An example of applying normalization to a set of 5 spheres is shown in [Figure 3.10](#).

### 3.6. FEATURE EXTRACTION

In this section, several shape feature extraction methods are described. In each method an array of values is extracted as feature vector and a combination of all feature vectors is provided to the classifier as samples dataset.

The lesion meshes as complex objects must be mapped into a feature vector in a multidimensional space using *feature transforms* [64]. Among those transforming methods, the first three (*Volume-*

**Algorithm 3.2** Sphere components normalization using scaling by overall maxima method

---

```

1: procedure NORMALIZESPHERES (SPHERESLIST spheresList)
2:   Set max = maximum(for all positions x,y,z in spheresList)
3:   Set min = minimum(for all positions x,y,z in spheresList)
4:   Set diff = max - min ▷ the difference value
5:   for each sphere in spheresList do
6:     sphere.position(X, Y, Z) = (sphere.position(X, Y, Z) + abs(min)) ÷ diff
7:     sphere.radius = sphere.radius ÷ diff
8:   end for
9: end procedure

```

---

#	x	y	z	R
0	-75.3692	-37.7979	11.8563	2.1406
1	-85.1198	-29.7031	6.5474	0.7516
2	-85.8355	-37.0971	8.0866	0.5956
3	-84.9846	-33.1219	11.8964	1.1526
4	-74.7476	-35.0559	11.9773	0.673

(a) An example of 5 internal spheres without normalization

#	x	y	z	R
0	0.107003	0.491118	0.998763	0.0218847
1	0.00731704	0.573876	0.944487	0.00768407
2	0	0.498282	0.960223	0.00608918
3	0.00869927	0.538923	0.999173	0.0117837
4	0.113358	0.519151	1	0.00688049

(b) Normalized components of the same 5 spheres

**Figure 3.10:** An example of spheres components before and after normalization. The first three components ( $x$ ,  $y$ ,  $z$ ) show the position of the center and  $R$  is radius. The values range after normalization for all components are mapped between zero and one.

*Radius Histogram*, *3D Spherical Shape Histogram*, and *Graph Topological Features*) are based on the embedded spheres, packed into the lesion mesh. The *3D Zernike Descriptor* features are directly calculated from the binary volumetric object of lesions.

In the literature [36, 65–67], there are numerous feature extraction methods, especially from 3D models. Such methods are described comprehensively in [62]. Studying the the existing methods got me inspirations to adapt them into a special case of usability for sphere packing. One could find several more interesting and useful methods when there is adequate time for exploration.

### 3.6.1. VOLUME-RADIUS HISTOGRAM

The histogram of volume-radius feature provides an estimate for the proportion of the volume covered by spheres with a specific radius range. Some experimental observations are done on the alignment and structure of internal packed lesions:

- Benign lesions in comparison to malignant ones have a more regular shape mostly with oval or round form. According to the principal essence of the sphere packing algorithm, which initially tries to occupy as much proportion as it can with the biggest sphere possible, it is found out that the majority of their internal space is filled with a few number of very big spheres and the rest is occupied by smaller ones with considerable differences in size.
- On the contrary, in malignant lesions, there is no such regularity: most of their volume is occupied with middle size spheres and the rest are either big ones or small ones which are scattered along the shape.

Therefore, a histogram can be created such that on the x-axis lies radius of the spheres and the y-axis is the summation of spheres' volumes with radius between two bins. An arbitrary number of bins

in x-axis can be considered to form the radius range of spheres. On the y-axis values represent the amount of lesion's volume occupied by spheres with a particular radius range.

Figure 3.11 shows two examples of the mentioned histogram for benign lesions (on top) and two examples for malignant lesions (on bottom). By collecting the corresponding value to each radius range on x-axis, a feature vector of an arbitrary number of features can be extracted from this method. This is one of the feature vectors needed to generate the samples dataset for the classifier.

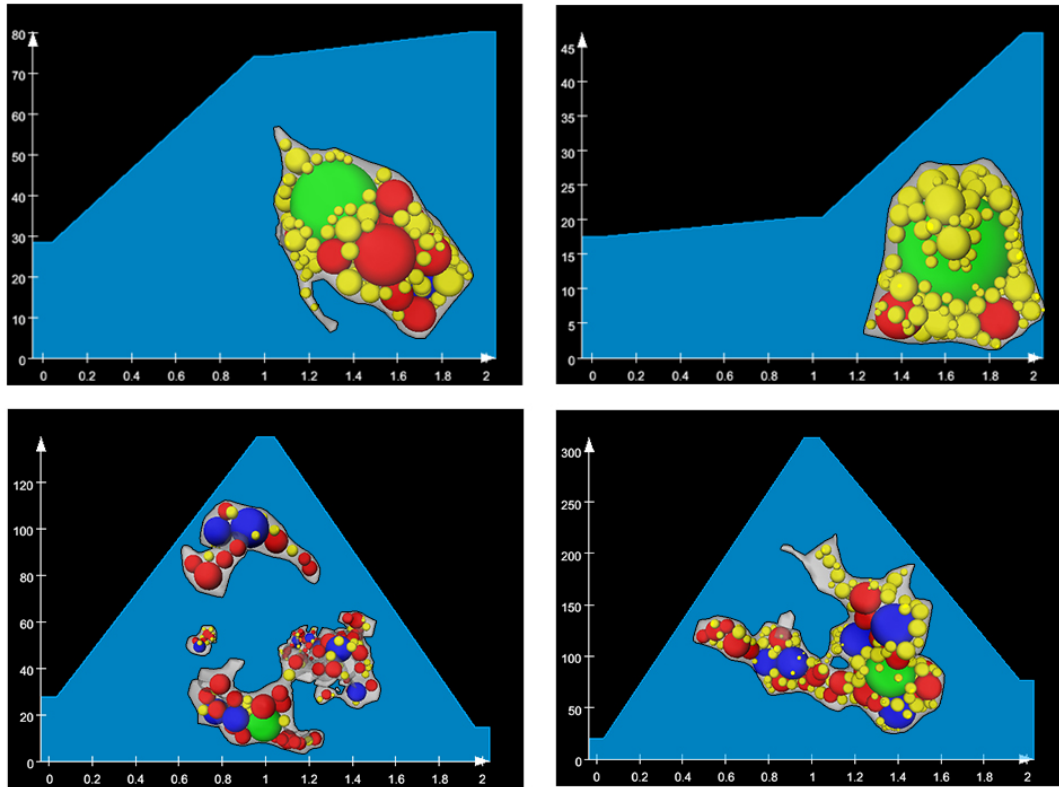


**Figure 3.11:** The Volume-Radius histogram from the objects packed with 200 spheres of two examples of benign (**on top**), and two examples of malignant lesions (**on bottom**). The difference between histogram shapes can be seen here, according to the different distribution pattern of sphere sizes. In benign lesions most of the object is filled with spheres having a big radius; in malignant lesions middle size spheres occupy most of the internal space. The color of spheres is based on size and is only for better differentiation in visualization.

### 3.6.2. 3D SPHERICAL SHAPE HISTOGRAM

In this section a feature vector extraction method is introduced, uses uniformly distributed elements of a 3D shape. Here, elements are the spheres positioned inside the 3D object.

I adapted the idea of 3D Spherical Shape Histogram feature extraction approach from a section coding technique developed for retrieving 2D polygons by Ankerst et al. [64]. They introduced 3D shape histograms as intuitive feature vectors [66]. Generally, shape histograms are based on partitioning of space in which elements reside i.e., a complete and disjoint decomposition into cells, which correspond to the bins of the histograms [36]. They suggested three techniques for space decomposition: a shell model, a sector model and a spiderweb model as the combination of the former two.

Figure 3.12 illustrates the space partitioning technique, which I got inspired of. In the preprocessing step, the origin of the model is moved to the centroid point. Thus the models are aligned to the center of mass of the solid [62].

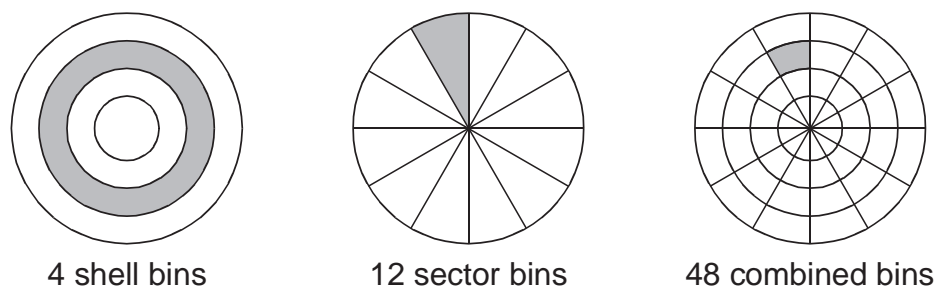


**Figure 3.12:** Shells and sectors as basic space decompositions for shape histograms. In each of the 2D examples, a single bin is marked (Figure taken from [64])

The definitions of each space partitioning approaches are as follows:

1. **Shell model:** The model is decomposed into concentric shells around the model's center point. This representation is particularly rotation independent such that any rotation of an object around the center point of the model results in the same histogram. The radii of the shells are driven from the dividing the outermost shell's radius by the number of shells needed.
2. **Sector model:** The model is broken down into sectors that emerge from the model's center point. This approach is related to the 2D section coding method. However, there is a more sophisticated definition and computation of 3D sector histograms, and they define the sectors as follows: To distribute the desired number of points uniformly on the surface of a sphere. For this purpose, they use the vertices of regular polyhedrons and along with their recursive refinements. Once the points are distributed, the Voronoi diagram of the points immediately defines an appropriate decomposition of the space. Since the points are regularly distributed on the sphere, the Voronoi cells meet at the center point of the model. For computation of sector-based shape histograms, one does not need to materialize the complex Voronoi diagram, but simply apply a nearest neighbor search in the 3D model, since the typical number of sectors is not very large.
3. **Combined model:** More detailed information is represented than the pure shell models and pure sector models in the combined model. A simple combination of two fine-grained 3D decompositions results in a higher dimensionality. However, since the resolution of the space decomposition is a case based parameter, the number of dimensions may easily be tuned application based [64].

As can be seen in Figure 3.13, Ankerst et al. [64] depicted different shape histograms for the example protein, 1SER-B, which is located on the left side of the figure. The middle figures are schematics of the various space decompositions and, on the right side, there placed the corresponding shape histograms. The histogram on top is only based on shell bins, and the one on the bottom is defined by 122 sector bins. The histograms in the middle are defined by 20 shell bins and 6 sector bins, and by 6 shell bins and 20 sector bins, respectively, and they follow the combined model. All the different histograms in this example have approximately the same dimension of about 120. In these examples, the histograms are not built from volume elements, but from uniformly distributed surface points acquired from the molecular surfaces [62].

For the very special case of this study, each 3D model is packed by spheres instead of voxels or points. Therefore, the method presented by Ankerst et al. [64] is adapted. The method is modified such that all the spheres inside each 3D lesion model are completely surrounded by a *spherical wireframe or cage like structure* with internal shells, sectors, and bins analogous to their shape his-

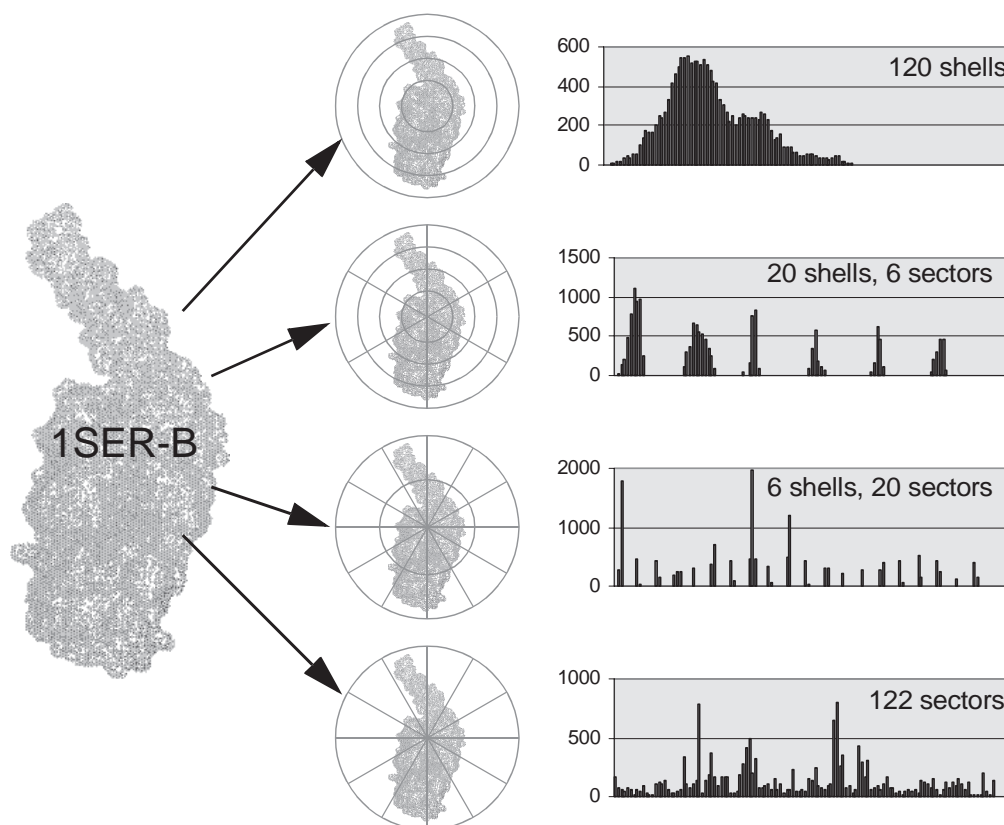


**Figure 3.13:** Several 3-D shape histograms of the example protein 1SER-B. The example *protein 1SER-B* is located on the **left** side of the figure; in the **middle**, the protein is surrounded by various space decompositions; on the **right** the corresponding shape histograms are depicted. From **top to bottom**, the number of shells decreases and the number of sectors increases. All of the different histograms have approximately the same dimension of about 120 (Figure taken from [64]).

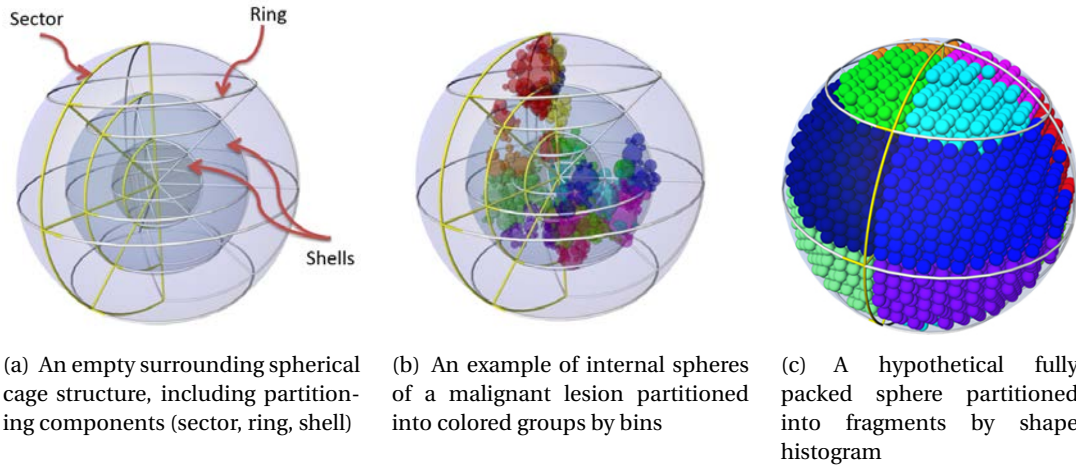
togram.

Figure 3.14 shows an illustration of my developed approach based on the shape histogram method:

- Figure 3.14(a) shows an empty example of the proposed development for shape histogram. It has been divided into a number of *sectors* (vertical lines as longitude in geographic coordinate system), *rings* (horizontal lines as latitude in geographic coordinate system), and *shells* (concentric spheres with various radius). Each spherical *wedge segment* delimited by two sectors, two rings, and two shells, represents a *partition* or *fragment*.
- Figure 3.14(b) shows internal spheres of a packed malignant lesion which are surrounded by the proposed spherical wireframe. As can be seen, the inner spheres of each partition, colored differently, showing that their centroids are inside the same partition and they belong to the same group.
- Figure 3.14(c) shows a hypothetical fully packed sphere, divided into segments which clearly shows how partitioning has separated the internal spheres into different groups.

Several strategies can be considered in order to choose the best location for placing the *center point* in space among all the spheres. As can be seen in Figure 3.15, I examined four strategies out of many possible ones to choose the centroid points according to the distance and the size of the spheres.

- In Figure 3.15(a), the center point's location is calculated based on the *mean value* of the all



**Figure 3.14:** Space decompositions for the proposed 3D Spherical shape histogram. In this approach the internal spheres are surrounded by a spherical wireframe with several partitions. Then, the number of surrounded spheres within each partition are counted as histogram bin values and feature vector elements.

spheres center points locations in 3D space. After finding the 3D coordinates of the centroid, I estimate its distance with all the internal spheres and choose the longest distance plus the radius of that most distant sphere as the radius of the spherical wireframe.

- In [Figure 3.15\(b\)](#), the centroid is placed precisely in *middle of the two most distant* internal spheres among all. Then to calculate the radius, I do exactly as I did for the first strategy.
- The third strategy is shown in [Figure 3.15\(c\)](#). Here, instead of finding the centroid location, I place it right in the *center of the biggest sphere* among all. Then radius is estimated as the first strategy. Consequently, the biggest sphere is not considered in the tally of histogram values, since its center point does not belong to any of the sections.
- The last strategy is shown in [Figure 3.15\(d\)](#). The location of center point is acquired using an extension of Gärtner's Smallest Enclosing Ball method [68] based on a simple randomized algorithm by Emo Welzl [69]. The C++ implementation of the code is publicly available<sup>2</sup> to calculate the Smallest Enclosing Balls of Points and also is included in The Computational Geometry Algorithms Library (CGAL)<sup>3</sup> [70]. It is a recursive algorithm which guarantees to compute the smallest sphere that contains all of the given set of packing spheres in the Euclidean space.

After partitioning of the spheres, it is time to generate the feature vector. The output histogram shows the distribution of spheres into several partitions for each lesion 3D shape. Then, the feature vector is composed of output histogram values obtained from the tally of the number of spheres' center points enclosed inside each partition. The number of bins in the histogram depends on the multiplication of the quantity of sectors, rings, and shells ( $sectors \times rings \times shells$ ).

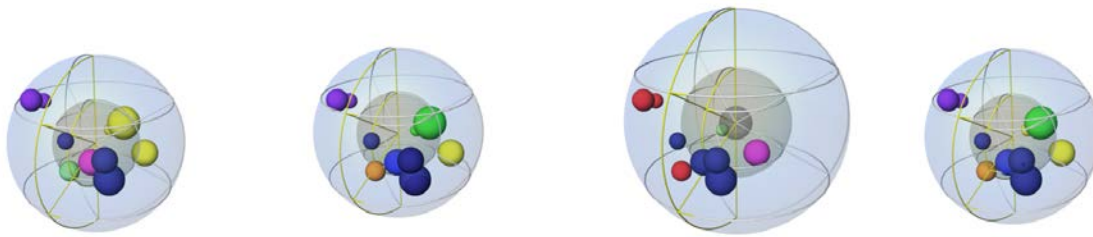
After creating the histogram, another interesting attribute is extracted using this technique, which is the occupied proportion of the surrounding wireframe sphere with internal spheres regardless of its partitioning. Based on the experimental observations, for benign lesions, which often have a round shape, the surrounding sphere is more occupied with internal spheres than the malignant ones. This attribute is closer to one for benign lesions (see [Figure 3.17\(a\)](#)) and it is near

<sup>2</sup>Smallest Enclosing Balls of Points - Fast and Robust in C++. (Bernd Gärtner)

<http://www.inf.ethz.ch/personal/gaertner/miniball.html> [Accessed on 10 August 2015]

<sup>3</sup>The Computational Geometry Algorithms Library (Sitewide ATOM)

<http://www.cgal.org> [Accessed on 10 August 2015]



(a) The center point is placed in the *mean distance* of the all spheres' center points  
 (b) The center point is placed in the *middle of the two most distant* spheres  
 (c) The center point is placed right in the *center of the biggest* sphere  
 (d) The center point is located according to the *Smallest Enclosing Ball of Balls* algorithm

**Figure 3.15:** Different strategies for choosing the place for spherical wireframe center point. Choosing various center point locations affects the radius of the spherical wireframe. Different colors of spheres represent that they belong to different sections based on 3D space decomposition by spherical wireframe.

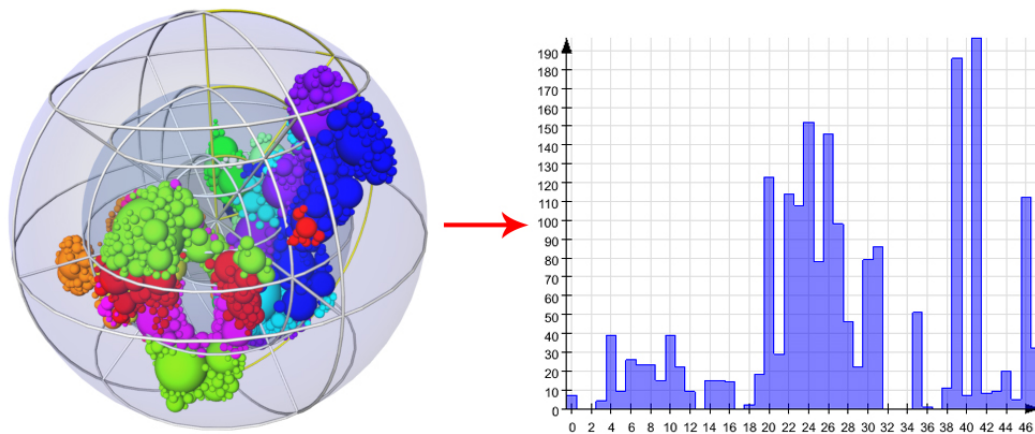


**Figure 3.16:** Corresponding histogram of the proposed 3D space decomposition. The histogram bins represent each segment of spherical cage and bin values are the tally of the number of spheres' center points enclosed inside each partition. The number of bins in the histogram depends on the value of  $sectors \times rings \times shells$ . Different colors of internal spheres represent their belonging to particular sectors which is a bin in corresponding histogram.

zero for malignant ones (see Figure 3.17(b)). Finally, histogram values for bins and filled proportion attribute are put together as the feature vector from this method.

### 3.6.3. GRAPH TOPOLOGICAL FEATURES

This section expresses how to extract descriptions from a 3D shape using a graph-based representation. Such driving the elements of shape into significant parts is basically used for classification of the 3D objects [67]. Recently, graph theory has been used to characterize the spatial arrangement of the object's components by constructing a graph considering each embedded component as the node.

The drawback of several available graph based algorithms (Delaunay, Voronoi, Minimum Spanning Tree) is that they do not allow for elicitation of local spatial attributes from complex networks such as the ones emerge from large volumetric MR images, possibly containing millions of voxels [71]. Similar to an approach proposed by Ali et al. [71], in this paper, I exploited the distribution of embedded spheres from sphere packing as a geometrical signature to retrieve shape features from

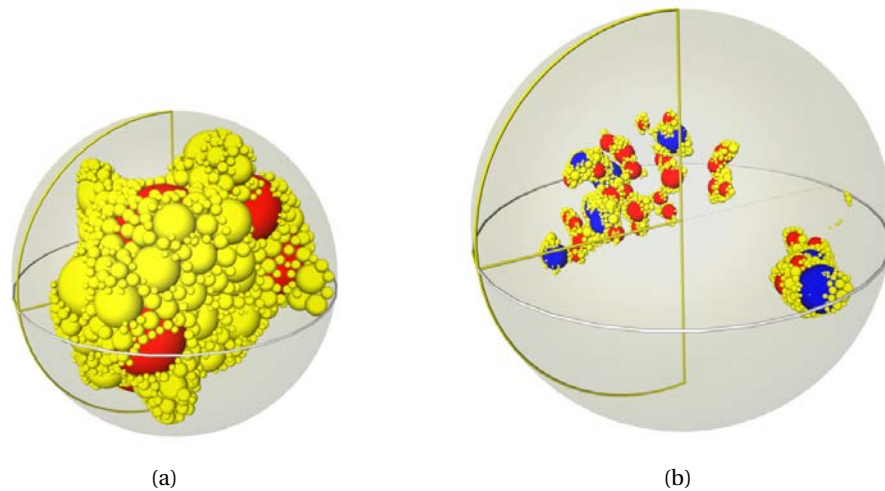


**Figure 3.17:** Proportion of smallest enclosing spherical wireframe, filled by embedded spheres. For benign lesions most of the enclosing spherical wireframe is filled by internal spheres **(a)**. For malignant lesion, the enclosing wireframe is occupied mostly by empty space **(b)**.

any 3D objects. Here, I considered the center point of each embedded sphere as a node to construct a graph. The spatial relationship between nodes is translated into edges. Each edge between any pair of nodes has a certain weight with respect to their distance. Spatial constraints are employed to deconstruct the entire graph into subgraphs and then, I extract global and local graph based features.

Applying the graph theory assists characterizing the complex structures of networks, leading to a better realization of dynamic interactions exist between their components [71] and extracting graph-based descriptions. In the following,  $G = (V, E, \delta V, \delta E)$  is an undirected, labeled graph of nodes  $V$  and edges  $E$  where  $\delta V : V \rightarrow \mathbb{R}^p$ ,  $\delta E : E \rightarrow \mathbb{R}^d$  associate to every node and edge numerical attributes.

I presume that graph  $G$  can have multiple edges from one node to another. A path  $p$  is a sub-graph of  $G$ , defined by a sequence of  $l$  nodes  $p = (v_1 \cdots v_l)$  such that for each  $i$ ,  $(v_i v_{i+1}) \in E$ . The length of  $p$  is defined as  $l(p) = f(\delta_V(v_i), v_i \in p, \delta_E(e), e \in p)$ , where  $f$  is a real function defined on the set of nodes and edges.  $p$  is said to be the shortest path between  $v_i$  and  $v_j$  if for all path  $p'$  between these two nodes,  $l(p) < l(p')$  [67].

Taking advantage of two libraries that provide graph algorithms and data structures, I was able to generate several graph compositions by connecting the internal spheres together. *The Boost Graph Library (BGL)*<sup>4</sup>, a part of Boost C++ Libraries, allows me to generate Prim's Minimum Spanning Tree and Kruskal's Minimum Spanning Tree (see Figure 3.18(a)(b)) and cluster graph structures by giving the shortest path between each two nodes [72]. *Neighborhood Graph Library (NGL)*<sup>5</sup>, a lightweight library written in C++ that supports a variety of geometric neighborhood graphs in arbitrary dimensions, serves to construct Relative neighbor, Gabriel, and  $\beta$ -Skeleton graphs [73] (see Figure 3.18(c)(e)(f)).

Further, clustering is applied to the graphs by restricting the neighbor search to  $k_{max}$  nearest neighbors of a center point. The  $k_{max}$  is a constant factor larger than the  $k$  value selected for  $k$  nearest neighbor graphs [74]. Figure 3.19 illustrates applying the  $k$ -nearest neighbors algorithm

<sup>4</sup>Boost C++ Libraries (The Boost Graph Library):

[http://www.boost.org/doc/libs/1\\_59\\_0/libs/graph/doc/index.html](http://www.boost.org/doc/libs/1_59_0/libs/graph/doc/index.html) [Accessed on 26 August 2015]

<sup>5</sup>Neighborhood Graph Library (NGL): <http://www.ngraph.org> [Accessed on 26 August 2015]

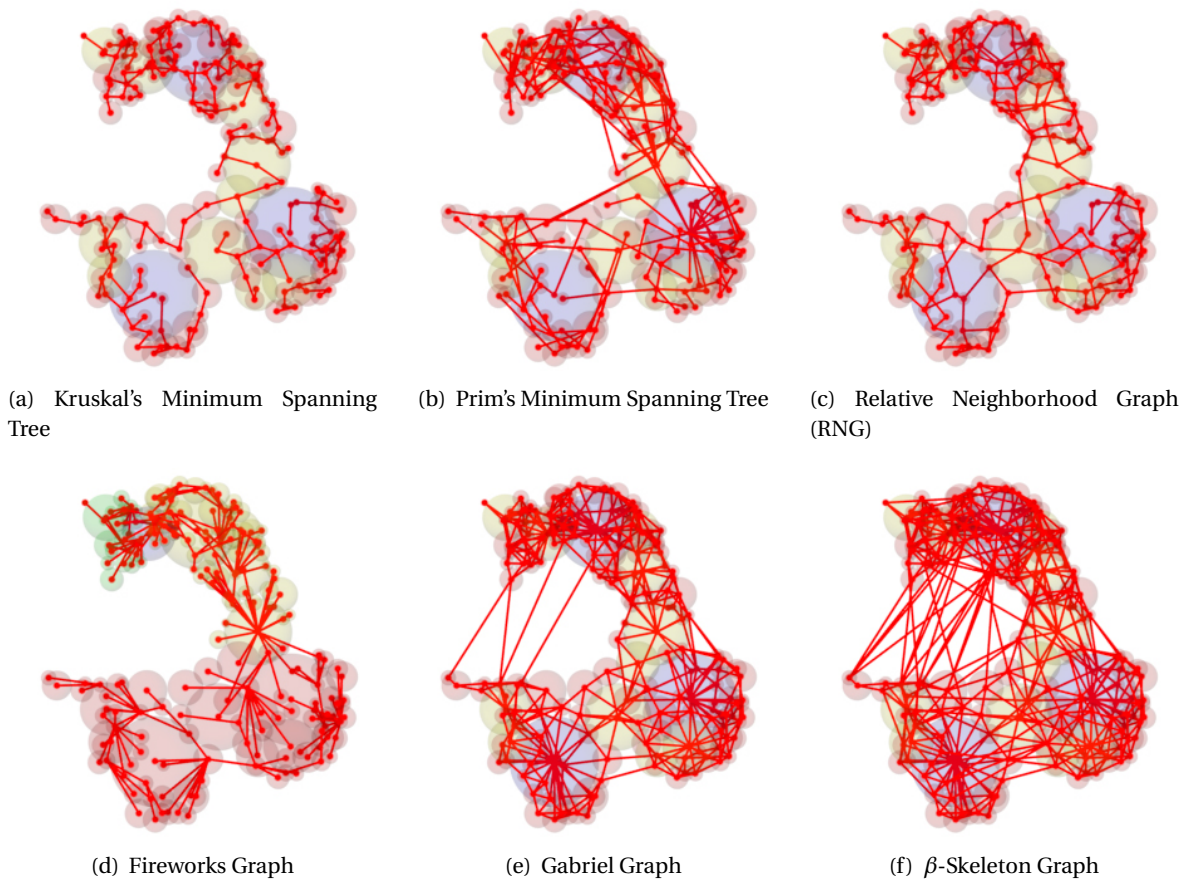


**Figure 3.18:** Different graph structures, acquired from various algorithms. The graph structures are obtained from connections between 200 internal spheres.

on a Gabriel graph with different  $k_{max}$  values, which divides the graph into isolated clusters. The  $k_{max}$  defines the neighborhood distance, so the less value it has, the less nodes are in each other's neighborhood and consequently, more clusters will be generated.

Once the graph structure is separated by different clusters, many graph characteristics can be obtained from the structure such as graph compactness: the more complete and dense the graph is, the more likely it is compact [75]. The compactness feature has different amounts among the graphs of benign and malignant lesion. Thus, a number of cluster validity indices for graph partitioning were adopted to compare different graph partitions [76] as morphological specifications.

In the following, the indices based on graph topology, forming the desired feature vector are pointed out.

### GRAPH COMPACTNESS INDICES

#### Edge Density

These are two simple indices to show graph compactness. Such indices are simply computable, but they do not consider the actual structure of the graph. In many cases, two graphs can have a different structure, although having the same edge density value, followed by the number of nodes and edges [76].

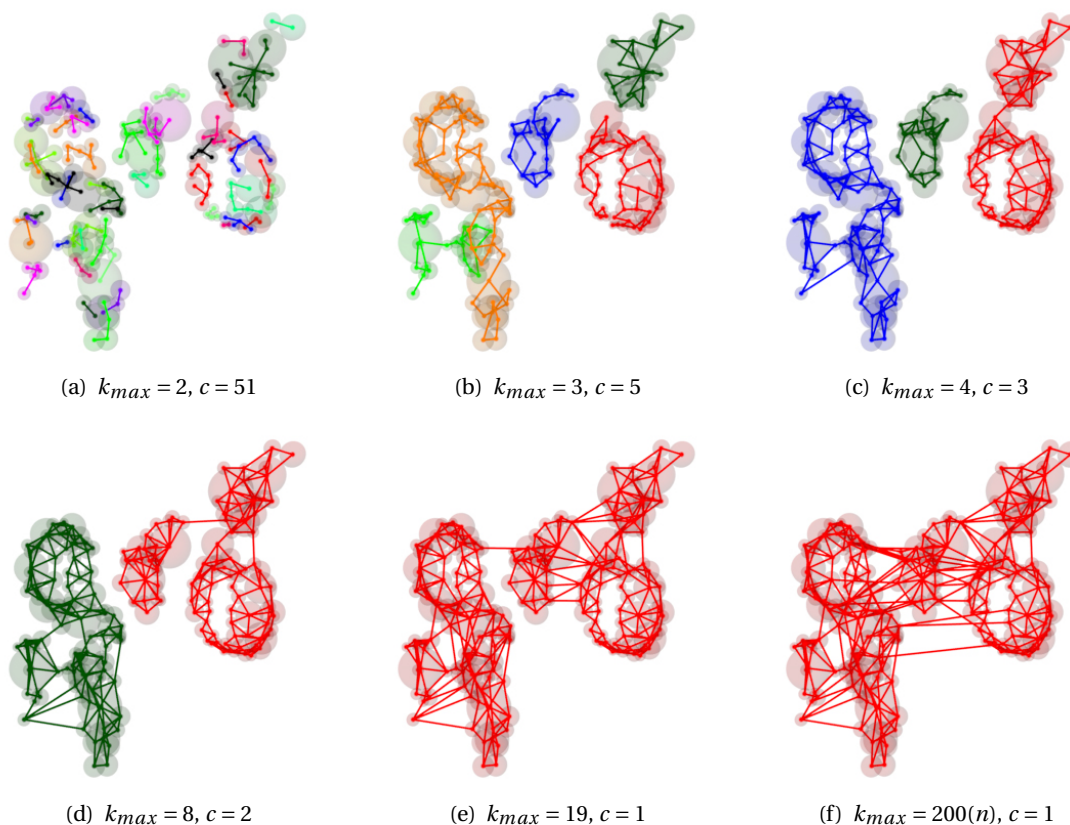


**Figure 3.19:**  $k$ -nearest neighbors algorithm with various  $k_{max}$  values. The  $c$  value represents the *number of clusters* resulted from applying the  $k$ -nearest neighbor algorithm to a Gabriel graph with 200 nodes. Different color indicates disparate clusters. As the  $k_{max}$  values go higher, there are more neighbors for each node in the graph and as a result, the number of clusters decreases. When  $k_{max}$  is equal to the number of nodes, they all are in the same neighborhood. Therefore, the graph contains only a single cluster.

$$\frac{E}{N}, \frac{E}{N^2} \quad (3.5)$$

In Figure 3.20,  $G_1$  and  $G_2$  have same compactness  $E/N = 13/8$ .

### Compactness index $C_p$

As introduced in [77], the compactness index  $C_p$  considers the connectivity of a connected graph  $G$ . It is computed in quadratic time as follows:

$$C_p = \frac{Max - \sum_{i=1}^{N-1} \sum_{j=i+1}^N d(v_i, v_j)}{Max - Min} \quad (3.6)$$

where  $Min$  and  $Max$  are, respectively, the minimum and maximum value of  $\sum_i \sum_j d(v_i, v_j)$ .

There are  $N(N-1)/2$  couples  $(v_i, v_j)$  of distinct nodes. If  $Q$  is defined as the maximal distance between two nodes,  $d(v_i, v_j)$  is between 1 and  $Q$ . Therefore,  $Min = N(N-1)/2$  and  $Max = Q \cdot N(N-1)/2$  [76].

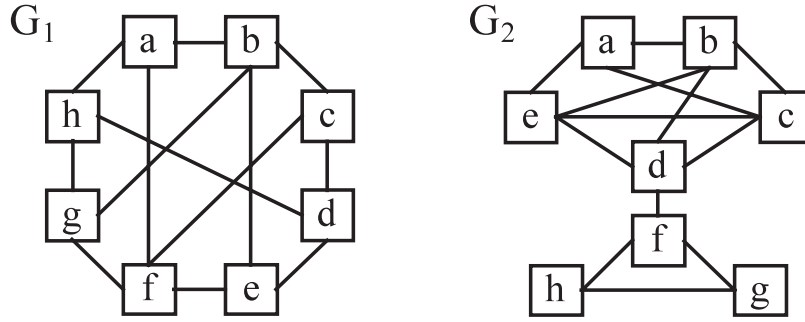


**Figure 3.20:** The same edge density compactness index value for two different graphs  $G_1$  and  $G_2$  (Figure taken from [76])

In Figure 3.20,  $Cp(G_1) = 0.48$  and  $Cp(G_2) = 0.69$ .

### New compactness index $Cp^*$

Boutin et al. [76] introduced a new normalized compactness index denoted  $Cp^*$  which considers a similarity measure instead of a distance.

Considering two nodes  $v_i$  and  $v_j$ , they defined similarity:  $sim(v_i, v_j) = 1/d(v_i, v_j)$ , if  $v_i$  and  $v_j$  are connected and  $sim(v_i, v_j) = 0$ , if  $v_i$  and  $v_j$  are disconnected. Note that  $sim$  value lies between 0 and 1. Now,  $Cp^*$  is computed by:

$$Cp^* = \frac{\sum_{i=1}^{N-1} \sum_{j=i+1}^N sim(v_i, v_j)}{N(N-1)/2} \quad (3.7)$$

$Cp^*$  is delimited between 0 and 1.  $Cp^*$  is zero, if  $G$  is completely disconnected.  $Cp^*$  is one, if  $G$  is a complete graph.

In Figure 3.20,  $Cp^*(G_1) = 0.73$  and  $Cp^*(G_2) = 0.69$ .

### Linear Structure of the Graph

Considering graph features, Harary et al. [78] first introduced a notion called *stratum*. This notion were used later by Botafogo et al. [79] to show the complexity of the hyperlinks as a directional graph structure. For that case, stratum reveals to what degree the hypertext is organized so that some nodes must be read before the others [79].

I adapt the stratum index to indicate the linear structure of the graph.

**Converted Distance Matrix (CDM):** The *distance matrix* contains the distances of every node to every other. When a node does not reach another node, the entry in the distance matrix is infinite. The sum of distances from a node to all other nodes is used to formalize the notion of *centrality*. The *converted distance matrix* is defined as follows [79]:

Let  $C$  be the *converted distance matrix* and  $M$  be the distance matrix. then

$$c_{i,j} = \begin{cases} M_{ij} & M_{ij} \neq \infty \\ K & otherwise \end{cases} \quad (3.8)$$

The choice of  $K$ , a finite *conversion constant*, strongly influences the centrality of nodes. A new notion of *converted distance matrix zero* is defined, when the value for  $K$  is chosen zero. Zero distance ( $K = 0$ ) means that there is no path between two nodes ( $d(v_i v_j) = \infty$ ). For this study,  $K$  is considered as the maximum distance in all indices of matrix plus one.

### Centrality Metrics of graph

This section provides several definitions over the *converted distance matrix*:

As defined in [79], the *converted out distance (COD)* for a node  $i$  is the sum of all entries in row  $i$  in the converted distance matrix (C).

$$COD_i = \sum_j C_{ij} \quad (3.9)$$

Likewise, the *converted in distance (CID)* for the node  $i$  is the sum of all entries in column  $i$  in the converted distance matrix:

$$CID_i = \sum_j C_{ji} \quad (3.10)$$

The *converted distance (CD)* of a graph is given by the sum of all entries in the converted distance matrix:

$$CD_i = \sum_i \sum_j C_{ij} \quad (3.11)$$

the *Relative Out Centrality (ROC)* metric for a node  $i$  is defined as:

$$ROC_i = CD / COD_i \quad (3.12)$$

The higher the ROC metric of a node, the more central it is (the inverse of the COD). Note that the ROC is normalized in relation to the size of the graph (CD), making it more convenient for comparisons between graphs.

The *Relative In Centrality (RIC)* metric is defined similarly as:

$$RIC_i = CD / CID_i \quad (3.13)$$

Figure 3.21 shows a directed graph with the associated converted distance matrix and its relative out-centrality and in-centrality metric. In this example, the value of  $K$  (the conversion constant) is 6, equal to the number of nodes in the graph.

Definitions of *status*, *contrastatus* and *prestige* ( $a_i$  and  $b_j$ ):

- Let  $G$  be an undirected graph (undigraph).
- Let  $d(u, v)$  be the distance between nodes  $u$  and  $u$  in  $G$ .
- The distance sum from  $v_i$ , in  $G$  (represented by  $a_i$ ) is the sum of the finite distances  $d(v_i, u)$  for all  $u$  in  $G$ . Thus,  $a_i$  is the sum of the finite entries in the  $i$ th row of the distance matrix  $DM(G)$ .
- The distance sum to  $v_i$  in  $G$  (represented by  $b_j$ ) is the sum of the finite distances  $d(u, v_j)$  for all  $u$  in  $G$ . Thus,  $b_j$  is the sum of the finite entries in the  $j$ th column of the distance matrix  $DM(G)$ .
- The total distance  $\sum_i \sum_j d_{ij}$ ,  $d_{ij} \neq \infty$  within a undigraph  $G$  is the sum of all the finite distances  $d(v_i, v_j)$  in  $G$ . Thus,  $\sum_i \sum_j d_{ij}$ ,  $d_{ij} \neq \infty$  is the sum of all the finite entries in  $DM(G)$ .

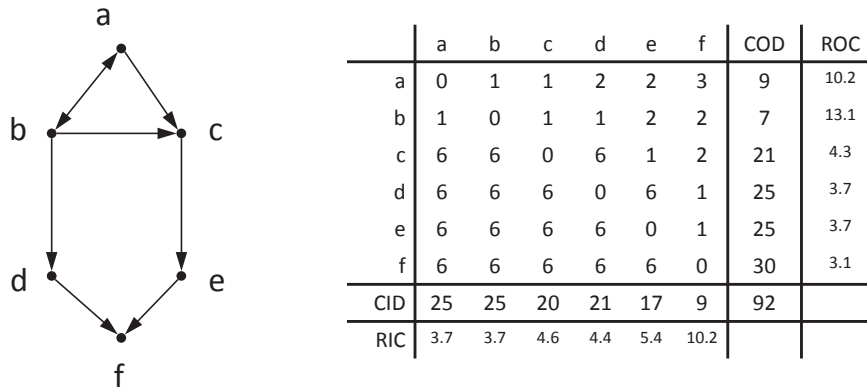


**Figure 3.21:** A graph with its *converted distance matrix* and associated metrics. The converted distance matrix elements are based on distances between each two nodes in the graph (Figure taken from [79])

According to the above definitions, It can be seen that the *status* of node  $v_i$ , is given by  $a_i$ , and the *contrastatus* of node  $v_j$  is given by  $b_j$ .

Another property of each node in the graph, namely its *prestige* can be defined. Harary [78] suggests that the net status of an individual, given by  $a_i - b_i$ , is a better indication of the prestige of an individual in a company [79]. Examples of the status, contrastatus, and prestige of each node in the graph can be seen in Figure 3.22.

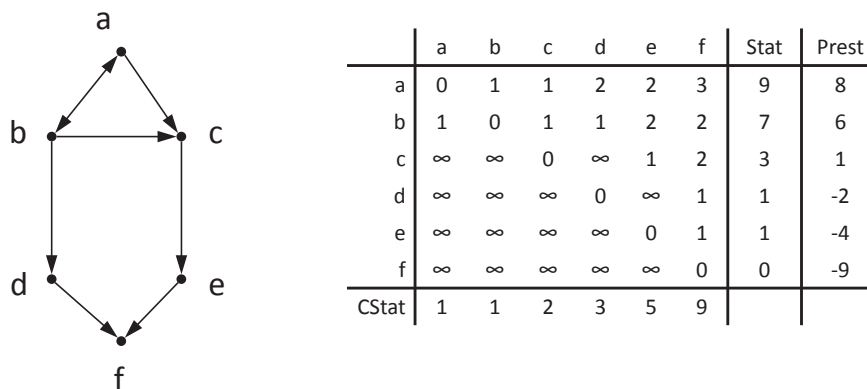


**Figure 3.22:** A graph with the "status", "contrastatus" and "prestige". **Note:** In a directional graph the nodes that reach all the other nodes have status identical to their COD metric. Similarly, nodes that are reached by all other nodes have identical contrastatus and CID metric (Figure taken from [79])

**Linear Absolute Prestige (LAP)**

The *linear absolute prestige (LAP)* of a graph with  $n$  nodes is identical to the absolute prestige of a linear graph with  $n$  nodes. As an example, the LAP of graph in Figure 3.23(a) is 16, since this is the absolute prestige of a graph with 4 nodes.

LAP is given by the following formula:

$$LAP = \begin{cases} \frac{n^3}{4}, & \text{if } n \text{ is even.} \\ \frac{n^3-1}{4}, & \text{if } n \text{ is odd.} \end{cases} \tag{3.14}$$

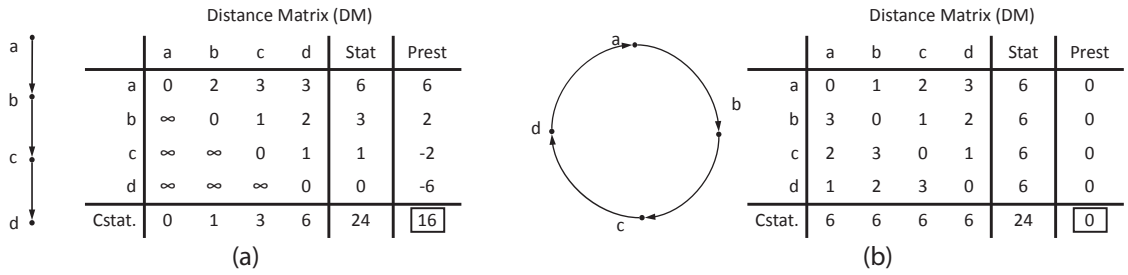


**Figure 3.23:** LAP examples of linear and circular graphs. (a) This linear graph is used as a basis for finding the linear absolute prestige of all graphs that have 4 nodes. The absolute prestige of the graph is 16. (b) In this graph, no structural clue to which node should be read first is present. The absolute prestige of the graph is 0 (Figure taken from [79]).

To define the stratum of the graph, the absolute prestige of the graph is normalized by dividing it by its LAP. Formally, the stratum ( $St$ ) is defined as

$$\text{Stratum}(St) = \text{absolute prestige}/\text{LAP}. \tag{3.15}$$

The *Stratum* ( $St$ ) metric was originally designed to capture the linear structure of the graph. Maximum stratum is achieved in a linear graph. If the stratum is equal to zero, this indicates that graph is structurally more complex [79].

INDICES BASED ON DIAMETER AND DISTANCE

Dunn's Index

Considering  $C_i$  and  $C_j$  as the closest clusters according to average distance  $d$  and  $C_h$  is the graph cluster with the largest diameter, *Dunn's index* [76, 77, 80] is acquired by:

$$D(C) = \frac{d(C_i, C_j)}{\text{diam}(C_h)} \tag{3.16}$$

$d(C_i, C_j)$  and  $\text{diam}(C_h)$  are respectively related to inter and intra-cluster connectivity.  $D$  is not robust since it depends only on few clusters and few edges between them.

Figure 3.24, in both  $G_3$  and  $G_4$ , closest clusters are  $C_2, C_3$  and largest cluster is  $C_1$ . So, Dunn's indices are the same.

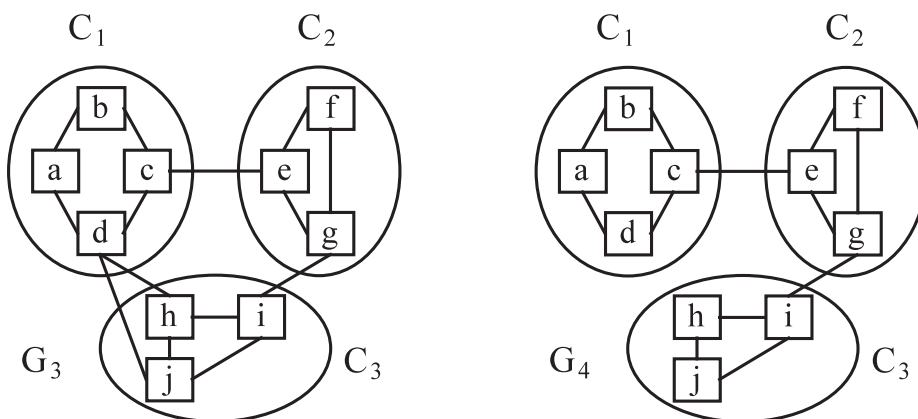


**Figure 3.24:** Same Dunn's index for  $G_3$  and  $G_4$  (Figure taken from [76])

### Davies Bouldin index

*Davies Bouldin index* introduced by David L. Davies and Donald W. Bouldin in 1979 [81], is a metric for evaluating clustering algorithms which indicates the similarity of clusters and how good the clustering has been done [76, 77]. This index is defined by:

$$DB = \frac{1}{K} \sum_{i=1}^K \max_{j \neq i} \left[ \frac{\text{diam}(C_i) + \text{diam}(C_j)}{d(C_i, C_j)} \right] \quad (3.17)$$

Small values of DB correspond to compact clusters. The Davies Bouldin index is more robust than Dunn's index [76].

### INDICES BASED ON INTER & INTRA-CLUSTER EDGES

#### A cut index called MinMaxCut

As defined in [76], the *cohesiveness* of cluster  $C_i$  is computed as follows:

$$\text{Cohesiveness} = \frac{E'_i}{E_i} \quad (3.18)$$

By considering  $E'_i$  as the number of edges between  $C_i$ , and the other clusters, *MinMaxCut* is defined as [82]

$$\text{MinMaxCut} = \sum_{i=1}^K \frac{E'_i}{E_i} \quad (3.19)$$

*MinMaxCut* attempts to maximize the community similar to the node communities while minimizing the degree of similarity between the nodes. The smaller value *MinMaxCut* has, the graph has a higher connection density [83].

In Figure 3.25, *MinMaxCut* is the same for  $G_5$  and  $G_6$  ( $\frac{1}{2}$ ) whereas  $G_6$  contains components with smaller diameter.

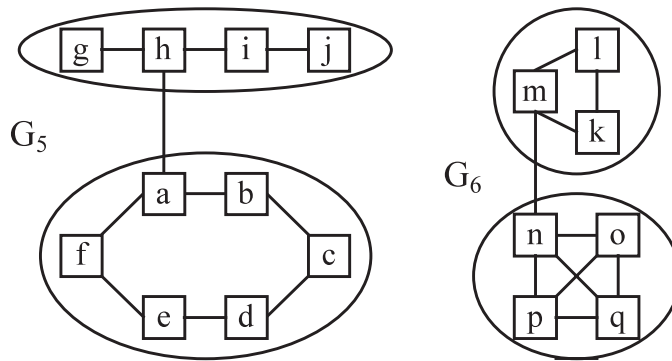


**Figure 3.25:** Same *MinMaxCut*, conductance and coverage values for both graphs (Figure taken from [76])

### Cohesion of a graph clustering

*Cohesion (WSS)* is a measure of how closely nodes are related within a cluster and is measured by the within sum of square distances to the mean distance:

$$WSS = \sum_i \sum_{x \in C_i} (x - m_i)^2 \quad (3.20)$$

where [84] is a cluster,  $\mathbf{m}$  is the mean distance value within each cluster and  $\mathbf{x}$  is the node distance from cluster center [84].

### Coverage of a graph clustering

Coverage of a graph clustering  $C$  is the fraction of intra-cluster edges within the complete set of edges [85].

$$Cov(C) = \frac{\sum_{i=1}^K E_i}{E} \quad (3.21)$$

Large values of coverage shows better quality of clustering of  $C$ . This index is easy to compute but it does not include the number of nodes  $N_i$  in  $C_i$  [76].

### INDICES BASED ON MODULARIZATION QUALITY

#### Modularization quality MQ

The function of *Modularization quality* is based on the difference between intra and inter cluster connectivity [86]: Intra-cluster connectivity of  $C_i$  is computed by:

$$intra(C_i) = \frac{E_i}{N_i(N_i - 1)/2} \quad (3.22)$$

where  $N_i(N_i - 1)/2$  is the maximum number of intra-cluster edges. Inter-cluster connectivity between clusters  $C_i$  and  $C_j$  is defined by:

$$inter(C_i, C_j) = \frac{E_{ij}}{N_i N_j}$$

$$\text{Let define } \overline{intra} = \frac{\sum_{i=1}^K \frac{E_i}{N_i(N_i-1)/2}}{K} \text{ and } \overline{inter} = \frac{\sum_{i<j}^K \frac{E_{ij}}{N_i N_j}}{K(K-1)/2} \quad (3.23)$$

$$MQ = \overline{intra} - \overline{inter} = \frac{\sum_{i=1}^K \frac{E_i}{N_i(N_i-1)/2}}{K} - \frac{\sum_{i<j}^K \frac{E_{ij}}{N_i N_j}}{K(K-1)/2}$$

Unfortunately, this index computes simple instead of weighted means when clusters can be of different size [76].

In Figure 3.26, MQ ignores that  $C_1$  is larger than  $C_2$ .

#### A new Modularization quality index MQ\*

Boutin et al. [76] provided a new weighted MQ\* index by modifying the original MQ as follows:

$$MQ^* = \frac{\sum_i E_i}{\sum_i \frac{N_i(N_i-1)}{2}} - \frac{\sum_{i<j} E_{ij}}{\sum_{i<j} N_i N_j} \quad (3.24)$$

MQ\* takes into account the clusters' connectivity and their size unlike MQ.

In Figure 3.26,  $C_1$  is larger than  $C_2$  with a smaller intra-cluster connectivity, so MQ\* is smaller than MQ (In fact,  $MQ^* = 0.44$  and  $MQ = 0.64$ ).

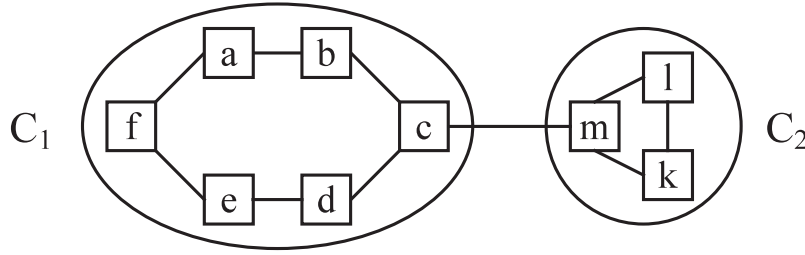


**Figure 3.26:** Two graph clusters with  $MQ^*$  smaller than  $MQ$  (Figure taken from [76]).

### INDICES BASED ON NODE'S NEIGHBORHOOD

Indices based on node's neighbors, by clustering measure of a node itself, can define if a node is well related to its cluster or not.

#### Silhouette index

Considering a node  $v_i$  which belongs to a cluster  $C_j$ , and the closest cluster to node  $v_i$  (according to average distance) is denoted  $C_h$ , the *silhouette index* is defined as in [76, 77] by:

$$s(v_i) = \frac{d(v_i, C_h) - d(v_i, C_j)}{\max(d(v_i, C_j), d(v_i, C_h))} \quad (3.25)$$

Note that  $-1 \leq s(v_i) \leq 1$ . Additionally, when  $s(v_i)$  is close to 1,  $v_i$  is said to be *well clustered*. When  $s(v_i)$  is inferior to 0,  $v_i$  should be assigned to the nearest neighboring cluster [76].

In Figure 3.26,  $s(m) = (2.5 - 1)/2.5 = 0.6$ ,  $s(k) = (3.5 - 1)/3.5 = 0.71$ .

For a given cluster  $C_j$  we compute silhouette  $S_j$  by:

$$S_j = \frac{\sum_{i=1}^{N_j} s(v_i)}{N_j} \quad (3.26)$$

A global silhouette value  $GS$  is also computed by:

$$GS = \frac{\sum_{j=1}^K S_j}{K} \quad (3.27)$$

#### A new index denoted $GS^*$

As proposed by [76], a new index  $GS^*$  is defined that takes into account the size of clusters:

$$GS^* = \frac{\sum_{j=1}^K N_j S_j}{\sum_{j=1}^K N_j} = \frac{\sum_{i=1}^N s(v_i)}{N} \quad (3.28)$$

In Figure 3.26,  $C_1$  is larger than  $C_2$  so its contribution is more important in  $GS^*$ .

### INDICES BASED ON CO-CLUSTEREDNESS

In [76], indices based on repartition of  $N(N-1)/2$  couples of nodes  $(v_i, v_j)$  in partitions  $P = \{C_1, \dots, C_K\}$  and  $P' = \{C'_1, \dots, C'_T\}$  are presented (see Table 3.1).

Partition of $\{(v_i, v_j)\}$	Same cluster in $P'$	Different cluster in $P'$
Same cluster in $P$	a	c
Different cluster in $P$	b	d

**Table 3.1:** Graph indices based on repartitioning (Table taken from [76]).

### Jaccard Coefficient

*Jaccard coefficient* is defined between  $P$  &  $P'$  as follows:

$$J = \frac{a}{a + b + c} \quad (3.29)$$

$J$  computes the probability that two nodes belonging to a same cluster in a partition also belong to a same cluster in the other partition.

### Folkes and Mallows index

*Folkes and Mallows* introduced another index:

$$FM = \sqrt{\frac{a}{a+b} \frac{a}{a+c}} \quad (3.30)$$

$a / (a + b)$  is the probability that two nodes belong to a same cluster in  $P$  if they belong to a same cluster in  $P'$ . Now,  $a / (a + c)$  is the probability that two nodes belong to a same cluster in  $P'$ , if they belong to a same cluster in  $P$  [76].

### Rand Statistic

*Rand Statistic* measures similarity between  $P$  &  $P'$  as follows:

$$R = \frac{a + d}{a + b + c + d} \quad (3.31)$$

Unlike  $J$  and  $FM$ ,  $Rand$  statistic is calculated with  $d$ . It computes the probability that two nodes belong either to a same cluster or to different clusters in both  $P$  and  $P'$  [76].

### Hubert and Arabie's statistic

Hubert and Arabie [87] modified the *Rand Statistic* index the such that its maximum is 1 and its expected value is 0, if classifications are selected randomly [76].

$$Hubert\ t = \frac{a \cdot d - b \cdot c}{\sqrt{(a+b)(c+d)(a+c)(b+d)}} \quad (3.32)$$

In Figure 3.27,  $a = 9$ ,  $b = 4$ ,  $c = 3$ ,  $d = 12$  and so  $J = 0.56$ ,  $FM = 0.72$ ,  $R = 0.75$ ,  $Hubert = 0.50$ .

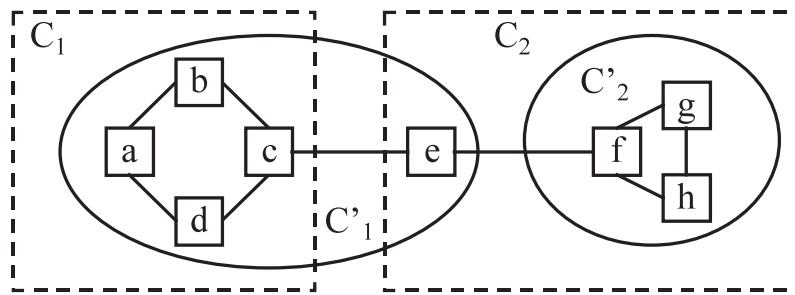


Figure 3.27: Comparison of cluster partitions  $P = \{C_1, \dots, C_K\}$  and  $P' = \{C'_1, \dots, C'_7\}$  (Figure taken from [76]).

### Feature vector based on graph topology

Figure 3.28 shows an example of extracting all the above mentioned graph topological features from a graph containing 200 nodes (spheres), clustered with different  $K - Max$  values, resulting different number of edges and clusters. Sometimes, indices return infinite values, which are not accepted by classifier algorithm. Therefore, they are replaced by zero value in the feature vector.

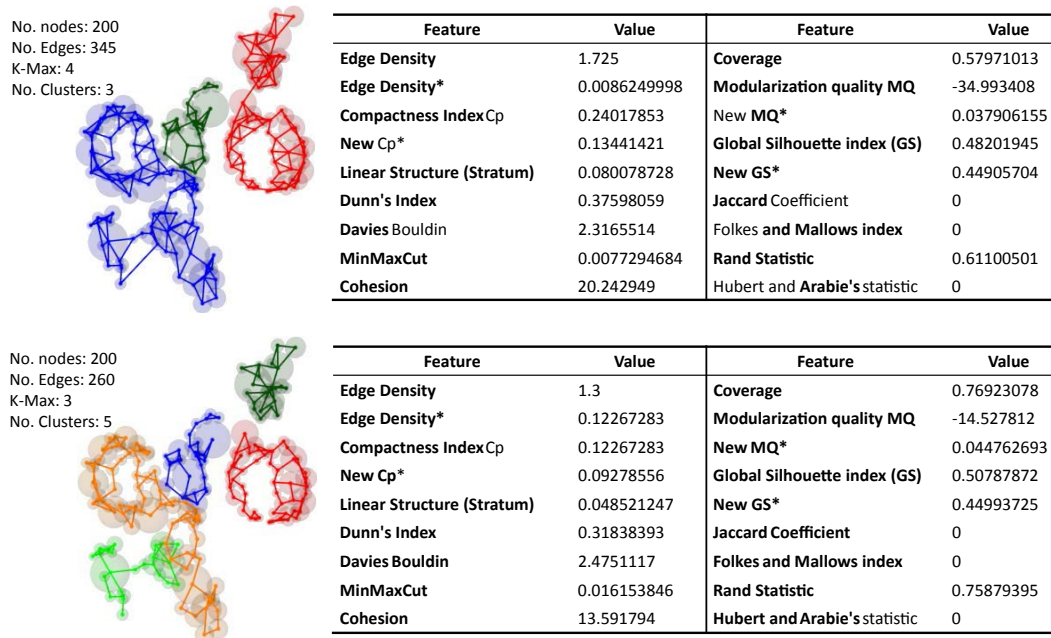


Figure 3.28: Graph topological features extraction example. **Top**, calculated features of graph structure from 200 nodes obtained from  $K - Max = 4$  clustering, including 345 edges and 3 clusters. **Bottom**, features of a graph from the same 200 nodes obtained from  $K - Max = 3$  clustering, including 260 edges and 4 clusters. Some indices return infinite values casewise, which are not accepted by classifier algorithm. Therefore, they are replaced by zero value.

The values of all the above mentioned indices are integrated into the graph based feature vector in the processing pipeline to feed the classifier.

### 3.6.4. 3D ZERNIKE DESCRIPTORS

Moment-based representations are sorts of object descriptors that have been exploited broadly for pattern recognition [88], object recognition [89], and shape matching [90]. They provide a compact numerical expression of the spatial features that enables rapid comparisons. Moments such as 2D/3D Zernike moments are based on the theory of orthogonal polynomials [91], which allow de-

scriptors to be constructed to an arbitrary order with some redundancy. It is also possible to reconstruct the object from its moments with quality determined by the number of terms used [88, 92].

The Zernike polynomials were introduced by Frits Zernike in 1934 [93]. Historically, Zernike introduced a set of orthogonal-normalized (Orthonormal) radial polynomials primarily dedicated to optical applications [94]. Later, the Zernike functions were used to define Zernike moments of 2D images [91] (see Figure 3.29 for 2D Zernike terms). More recent works used 3D Zernike moments to derive robust invariant descriptors of 3D images and/or objects and perform image/object reconstruction from a finite set of 3D Zernike moments [94].

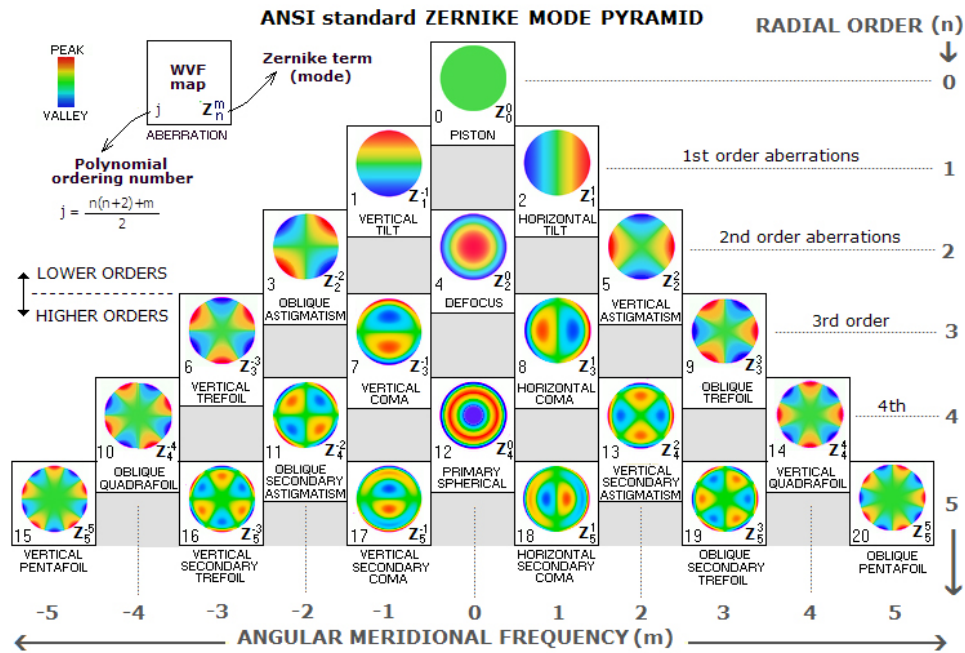


**Figure 3.29:** Graphical illustration of top 20 Zernike terms as a pyramid. Zernike terms ( $Z_n^m$ ) expansion pyramid is a function of term's radial degree (or order)  $n$  and azimuthal frequency  $m$ . It is the basis for classifying aberrations as lower ( $n \leq 2$ ) and higher-order ( $n > 2$ ) in ophthalmology. **On left:** associated Zernike terms and names of aberrations; the so called  $j$ -number (commonly referred as mode), the polynomial ordering number, is dependant on  $n$  and  $m$ , determining the position of the term in the Zernike terms' expansion. (Figure taken from [www.telescope-optics.net](http://www.telescope-optics.net))

The Zernike functions  $Z_n^m(r)$ , are base functions that are constructed to form an orthonormal set over the unit ball (i.e.  $0 \leq r^2 \leq 1$ ,  $r^2 = x^2 + y^2 + z^2$ ). They are based on the familiar spherical harmonics,  $Y_l^m(\theta, \phi)$  which  $\theta$  and  $\phi$  are the standard angular spherical coordinates. The spherical harmonics can be described as [95]:

$$Y_l^m(\theta, \phi) = N_l^m e^{im\phi} P_l^m(\cos \theta) = N_l^m \left( \frac{x + iy}{\sqrt{x^2 + y^2}} \right)^m P_l^m\left(\frac{z}{r}\right), \quad (3.33)$$

The normalization factor  $N_l^m$  is given by:

$$N_l^m = \sqrt{\frac{2l+1}{4\pi} \frac{(l-m)!}{(l+m)!}}, \quad (3.34)$$

and  $P_l^m(\cos \theta)$  are the associated Legendre polynomials.

The *3D Zernike Descriptors* are series expansion of an input 3D function, which allow rotation invariant and compact representation of a 3D object that is considered as the 3D function. The mathematical foundation of the *3D Zernike Descriptors* was laid by Canterakis [96]. Later, Novotni and Klein [97] applied them to 3D object retrieval. Below is a brief mathematical derivation of them. For detailed derivations and discussions, refer to the literatures [96, 97].

The 3D Zernike functions are defined as follows [95]:

$$Z_{nl}^m(r) = \sum_{\nu=0}^k q_{kl}^{\nu} r^{2\nu} e_l^m(r), \quad (3.35)$$

with the following definitions for parameters:

$$e_l^m(r) = r^l Y_l^m(\theta, \phi), \quad k = (n-1)/2, \quad (3.36)$$

$$q_{kl}^{\nu} = \frac{(-1)^{k+\nu}}{2^{2k}} \sqrt{2l+4k+3} \binom{2k}{k} \binom{k}{\nu} \binom{2(k+l+\nu)+1}{2k} / \binom{k+l+\nu}{k},$$

The coefficients  $q_{kl}^{\nu}$  are chosen to ensure orthonormality over the unit ball; they can also be written in terms of  $n$  as follows:

$$q_{nl}^{\nu} = (-1)^{\frac{n-1}{2}+\nu} \sqrt{2n+3} \frac{\Gamma\left[\frac{3+l+n}{2} + \nu\right]}{\nu! \Gamma\left[1 + \frac{n-1}{2} - \nu\right] \Gamma\left[\frac{3}{2} + l + \nu\right]}, \quad (3.37)$$

where  $\Gamma[x]$  is the complete Gamma function. The Zernike functions, therefore, are a 3D generalization of the spherical harmonics (see Figure 3.30), which are only orthonormal on the surface of the unit ball [95].

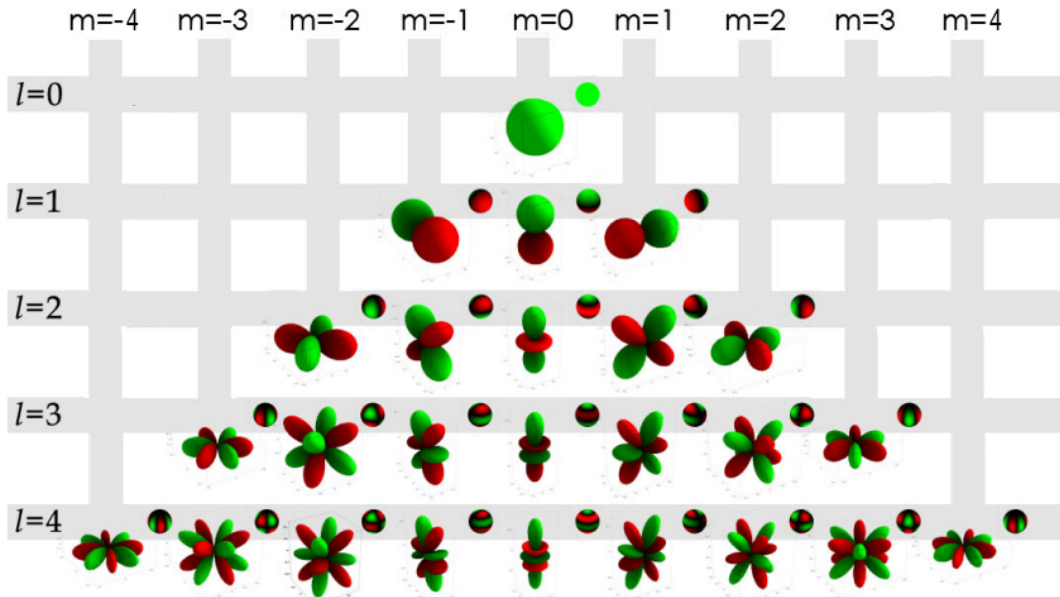


**Figure 3.30:** The 3D spherical harmonic basis. Visual representations of some of the first real spherical harmonics. **Green color** represents positive function values and **red color** represents where it is negative. The distance of the surface from the origin indicates the value of  $Y_l^m(\theta, \phi)$  in angular direction  $(\theta, \phi)$ . (Figure taken from [www.quora.com](http://www.quora.com))

Two instances of Zernike functions for  $(nl) = (53)$  and  $(nl) = (82)$  can be seen in Figure 3.31. It shows the isoamplitude surface for the real part of the Zernike function for each individual function,

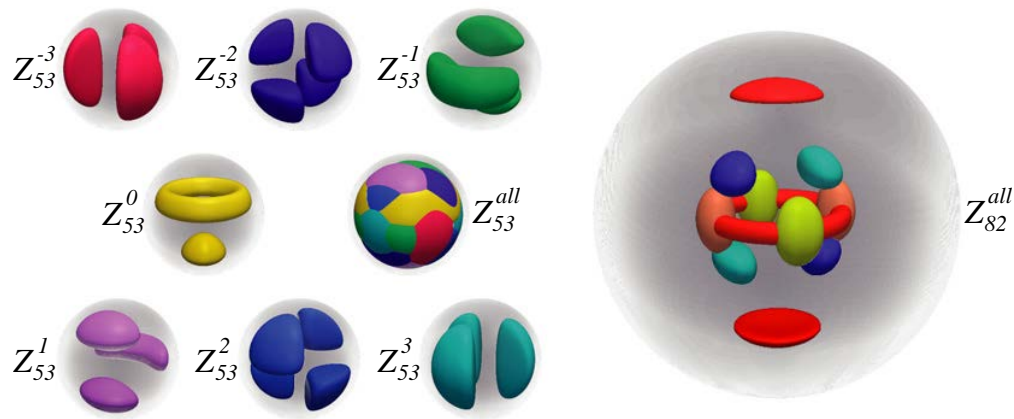


**Figure 3.31:** Example visualizations of selected 3D Zernike functions  $Z_{53}^m$  and  $Z_{82}^m$ . The gray halo around each function represents the embedding sphere. (Figure taken from [95])

at an amplitude level equal to 0.1. Note that, as Zernike functions are defined over the unit ball, to compute the moments using them, the object has to be scaled down to be fitted inside the unit ball before the computation [95].

For the current work, I used Zernike descriptors as complementary features to retrieve the shape specific feature vector of each lesion object [62]. Since the segmented lesions are originally in 3D volumetric voxelized format, I used a method to compute 3D Zernike descriptors from voxelized models as natural extensions of spherical harmonics based descriptors presented by Novotni and Klein<sup>6</sup> [97], which captures object coherence in the radial direction as well as in the direction along a sphere. The Zernike invariants acquired from each lesion forms a feature vector to be combined with other feature vectors and feed the classifier.

### 3.7. CLASSIFICATION USING RANDOM FOREST

Recently the applications of machine learning have drawn more attention in medical computing as a way to integrate the knowledge and experience of physicians in the areas such as computer aided diagnosis, detection and segmentation. The main function of these algorithms is to generalize from observed evidences and make predictions about unseen data [98].

In machine learning, every instance in the dataset presented to the algorithm, shares the same set of features. These features may be continuous, categorical or binary. The learning is called *supervised* if the algorithm is provided by the known labeled instances (the corresponding correct outputs), on the contrary, if instances are unlabeled, the learning is called *unsupervised*. The purpose of unsupervised (clustering) algorithms is to discover unknown, but useful, classes of items. *Reinforcement* learning is another type of machine learning in which the training data are provided to the learning system by the environment (external trainer) in the form of a scalar reinforcement signal that establishes a measure of how proper the system acts. The learner must discover which actions yield the best reward, by trying each action in proper sequence [99].

In the last decade, a number of machine learning methods have been introduced to be applied in several categories. Recently Caruana & Niculescu-Mizil [100] presented a large-scale empirical comparison between ten supervised learning methods: SVMs, neural nets, logistic regression,

<sup>6</sup>3D Zernike Descriptors (University of Bonn)

<http://cg.cs.uni-bonn.de/project-pages/3dsearch/downloads.html> [Accessed on 10 August 2015]

naive bayes, memory-based learning, random forests, decision trees, bagged trees, boosted trees, and boosted stumps. Their surprising results show that prior to calibration, bagged trees, random forests, and neural nets give the best average performance across all eight metrics and eleven test problems.

Random forests can be trained on large, very high-dimensional datasets without significant overfitting within a reasonable amount of time, since the tree construction is guided by the data density. RF is also very efficient at runtime, since matching a sample against a tree is logarithmic in the number of leaves. It also can tolerate a significant amount of labeling noise and errors in the training data [101]. Additionally, the independency of each tree in the forest to others, can greatly reduce the variance of estimation. Furthermore, the structure of random forest is flexible and more trees can be added to the forest later [102]. In the following section the random forest working mechanism is describe briefly.

### RANDOM FOREST

Among many existing machine learning techniques, random forests became a popular ensemble learning algorithm, as it achieve state-of-the-art performance in variety computer vision tasks. RF intuitively and flexibly offers a probabilistic foundation for dealing with different learning tasks. By effective partitioning of high-dimensional feature spaces via divide and conquer strategy and model probability distributions in each cell of these partitions, they permit to approximate any arbitrary functions or densities for classification, regression or clustering tasks. The divide and conquer strategy can be briefed as follows:

*"Partition observations by using a set of simple **decisions** in a **hierarchical** fashion" [98].*

In this section the basic algorithm of Random Forests for classification is briefly described. A detailed description of RFs is beyond the scope of this work and can be found in [103].

A Random Forest is formed by many binary decision trees which are inducted and trained on a training set consisting of multi-dimensional input data points  $x$  and the desired system output (e.g. class label)  $y$ . Each tree has access only to a random part of the whole data set, which this subset enters the tree at the root node [104]. One of the data dimensions  $f$  is randomly selected and a simple binary split is performed [105]. Equation 3.38 shows an example of the binary split where  $\theta$  is an arbitrary threshold:

$$x_f < \theta \quad (3.38)$$

The threshold  $\theta$  splits the data points: the ones that fulfill thresholding are circulated to the left child node, all others to the right child node. There are several methods to define the threshold  $\theta$  (e.g. by random sampling, as median, or by optimize the purity of the child nodes in consideration of the sample class distribution). The threshold splitting is applied to all nodes recursively, but always with different data dimensions and threshold values. The stop condition is if a maximal tree height is reached or too few data samples are available. Therefore, a leaf (terminal node) is created, that simply estimates the relative class-frequency  $P_t(c|n_t)$  of the data points, which reached this leaf (node  $n_t$  of tree  $t$ ) [105].

To estimate the class label of a query data point  $x$ , the query is propagated through all  $T$  trees of the forest beginning at the root node. Its way ends in exactly one leaf  $n_t$  in each tree  $t$ . The individual class probabilities  $P_t(c|n_t)$  of those leaves are combined using a simple average (see Equation 3.39), which provides the final estimate of the class' a posteriori distribution [105].

$$P(c|x) = \frac{1}{T} \sum_{t=1}^T P_t(c|n_t) \quad (3.39)$$

In RF each node has access to a specific subset of the whole dataset, namely the fraction of samples that are propagated by its parent to that node. During the training process these samples provide class labels which allow the computation of a local estimate of the class distribution within this node.

To sum up, in a decision tree, an input is entered at the top and as it traverses down the tree the data gets bucketed into smaller assortments. RF combines these trees with the notion of an ensemble (see Figure 3.32). Thus, in ensemble terms, the trees are weak learners and the RF is a strong learner [106].

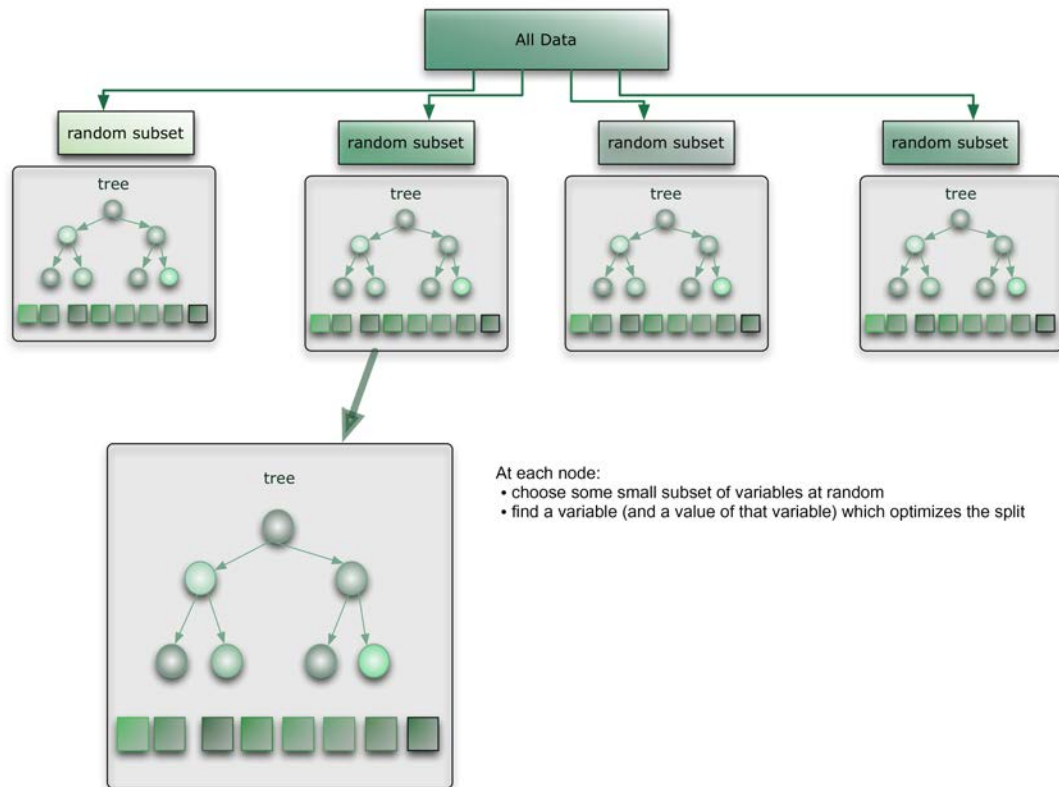


**Figure 3.32:** Random forest a combination of decision trees. At each node for some number  $m$  1)  $m$  predictor variables are selected randomly; 2) The predictor variable is used to do the best binary split on that node; 2) at the next node, randomly choose another  $m$  from all predictor variables and do the same (Figure taken from [citizenm.net](http://citizenm.net))

To classify the lesions types in this work, an implementation of RF algorithm existing in *The VIGRA Computer Vision Library* (Vision with Generic Algorithms) [107] is used. It is adopted since it was already implemented in *MeVisLab* (described in Chapter 4) and because of convenience of usage. For evaluation other tools were adopted (see Chapter 5).

# 4

## DEVELOPMENT

To develop the processing pipeline of this study, I used the MeVisLab<sup>1</sup> medical image processing framework. In the following sections more details regarding this powerful framework will be discussed.

### MEVISLAB FRAMEWORK

MeVisLab represents a powerful, modular framework for image processing research and development with a special focus on medical imaging. It allows fast integration and testing of new algorithms and the development of clinical application prototypes.

MeVisLab includes advanced software modules for segmentation, registration, volumetry, as well as quantitative morphological and functional analysis. The implementation of MeVisLab makes use of a number of well-known third-party libraries and technologies, most importantly the application framework Qt, the visualization and interaction toolkit Open Inventor, the scripting language Python, and the graphics standard OpenGL.

MeVisLab is developed by MeVis Medical Solutions AG in close cooperation with the research institute Fraunhofer MEVIS. A part of the modules contained in the MeVisLab distribution are directly contributed by Fraunhofer MEVIS [108].

Figure 4.1 shows MeVisLab graphic user interface (GUI) in Mac OS X.

### 4.1. PROCESSING PIPELINE

MeVisLab is a modular development framework. Based on modules, networks can be created and also applications can be built.

To support the creation of image processing networks, MeVisLab offers an IDE that allows data-flow modeling by visual programming [109].

A fundamental part of MeVisLab is the object-oriented MeVis Image Processing Library (ML) providing a generic framework for image processing.

Each algorithm is represented as a self-descriptive module inside the development environment. Via an intuitive graphical user interface, these functional units can be combined to form complex and powerful image processing networks that are executed by a core image processing

---

<sup>1</sup>MeVisLab website: <http://www.mevislab.de/> [Accessed on 26 August 2015]



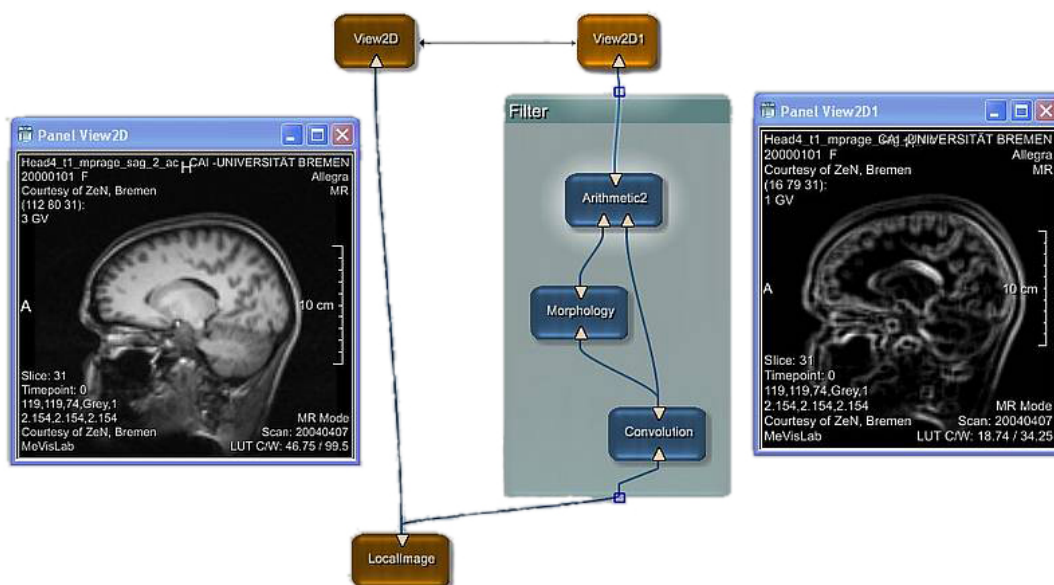


**Figure 4.2:** MeVisLab image processing network example. Each algorithm is represented as a self-descriptive module which can be combined with other modules to form complex and powerful image processing networks (Figure taken from [mevislab.de](http://mevislab.de))

offers a priority-controlled page cache and high performance for large data sets. *Macro Modules* can be created to encapsulate subnetworks of modules, scripting functionality and high-level algorithms [108].

Data connections (connectors) are provided to establish the links between modules. The output of one module can simply attach to another module's input to form a processing pipeline in which every module does an individual operation on the data.

In the following, each section of the processing network is describe in more details:

1. **Pre-processing:** As Figure 4.4(a) shows, in this step several modules are connected to do the preprocessing task and prepare the input for segmentation step. The module (1) loads the DCE-MR image sequence to the network as (2) loads the corresponding lesion binary mask provided by the radiologist. The two modules (3) reformat the image and the corresponding mask from any view that MR scan is taken to orthogonal view. Module (4) corrects the probable motion artifact in input MR sequence. Module (5) calculates the subtraction image from the MR sequences ( $t_1 - t_0$ ). Module (6) masks the lesion region from the subtraction image with the corresponding mask loaded.
2. **Segmentation:** This part of the network consists of modules doing segmentation and output the lesion within its enclosing box. As Figure 4.4(b) shows, this part begins with module (7) for mean shift segmentation. This module has two input images, the breast MR subtraction image and binary mask image. Module (8) applies a thresholding filter on the mean shift result and only passes the values above the defined threshold (here is 0.5). Two modules (9) and (10) put the segmented lesion into its smallest enclosing box by limiting the size of output to the lesion size to boost up the processing speed.
3. **Sphere Packing:** The module (11) shown in the Figure 4.5 packs the input lesion volume with 4000 spheres. The output of this module is shown with the number (12).
4. **Normalization:** Module (12) in Figure 4.5 normalizes the output spheres from the sphere

packing step and feeds the three upper feature extraction module sets.

5. **Volume-Radius Histogram:** The module set (14) are responsible for extracting the Volume-Radius histogram. The very bottom module in this set controls the new incoming data, the ML module in middle, creates the histogram and the ones on top extract the feature vector out of histogram.
6. **3D Shape Histogram:** The module set (15) extracts the shape histogram features. The main function is the macro module in the middle, which forms the spherical wireframe around all the packing spheres.
7. **Graph Features:** The module set (16) forms a graph based on input sphere data and extract all the earlier mentioned graph features from graphs topology.
8. **Zernike Invariants:** The module set (17) generates Zernike invariants directly from the lesion binary volume acquired from the segmentation step.
9. **Feature Combination** The module (18) gathers all the feature vectors generated by several modules sets and forms an all-inclusive linear feature vector in addition to the lesion's ID and class label (benign or malignant). All the acquired feature vectors are inserted into a CSV dataset file to provide to the machine learning algorithm.
10. **Evaluation:** After gathering all the samples in the dataset, It can be used to train the classifier. As can be seen in Figure 4.3, the samples dataset is loaded via the macro modules at the bottom to feed the machine learning modules. The modules *VigraRanodmForestTraining* is to train and create the forest model for RF algorithm. Module *VigraRanodmForestClassification* is the classification part of RF, which works based on the already created forest structure.

In Chapter 5, further analyzing and evaluation tweaks are done using Weka and R software on the dataset created by MeVisLab.

## COMPUTER-AIDED DIAGNOSIS (CADx) TOOL

Eventually, the whole processing framework was integrated into a *Computer-Aided Diagnosis (CADx)* interface to investigate its real applications. Using such tool, the radiologist can load the breast MR scans into the system, navigate through all the slices of 3D image and analyze the possible lesion enhancements.

Figure 4.6 shows a screenshot of the CADx GUI. One can annotate the suspicious lesion area by placing one or multiple seed points on each part of the distribution. Then, the tool automatically segments the lesion area using the inserted seed point and region growing algorithm. As can be seen in Figure 4.6, a seed point is placed on the lesion in breast subtraction image (yellow rectangle) and the corresponding 3D illustration of segmented lesion area is shown (in red) on the right side panel of the tool.

Now the lesion volume is ready to be analyzed by the framework in order to classify the type of the annotated lesion. The simple interface of the classification framework lies at the bottom right part of the interface of the CADx.

By pressing the "Classify" button, the result of the classification is shown to the user. For this case, the threshold of classification results is defined equal to 0.5 to discriminate the benign and malignant lesions. This value can also be change by user via the interface, but for simplicity of use it is hidden at this level.

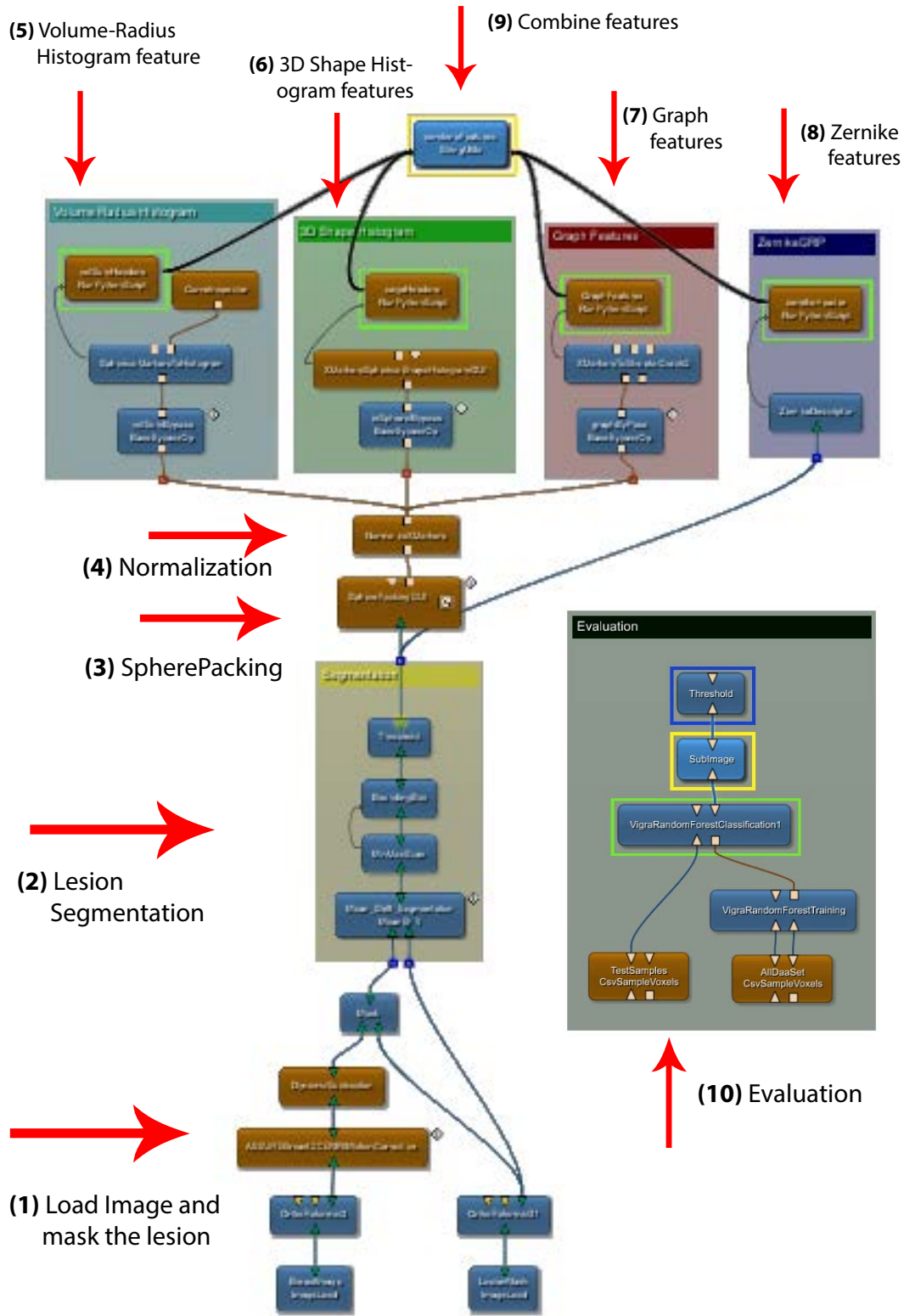


**Figure 4.3:** The processing network used in this work. The pipeline starts from bottom to top, including modules to load breast data, acquire the subtraction image, mask the lesion area (1), segmentation (2), sphere packing (3), normalization (4) and several feature extraction module groups (5-8). **On top**, the feature vectors are combined to form a dataset (9) and use to train the classifier and do the classification/evaluation (10).

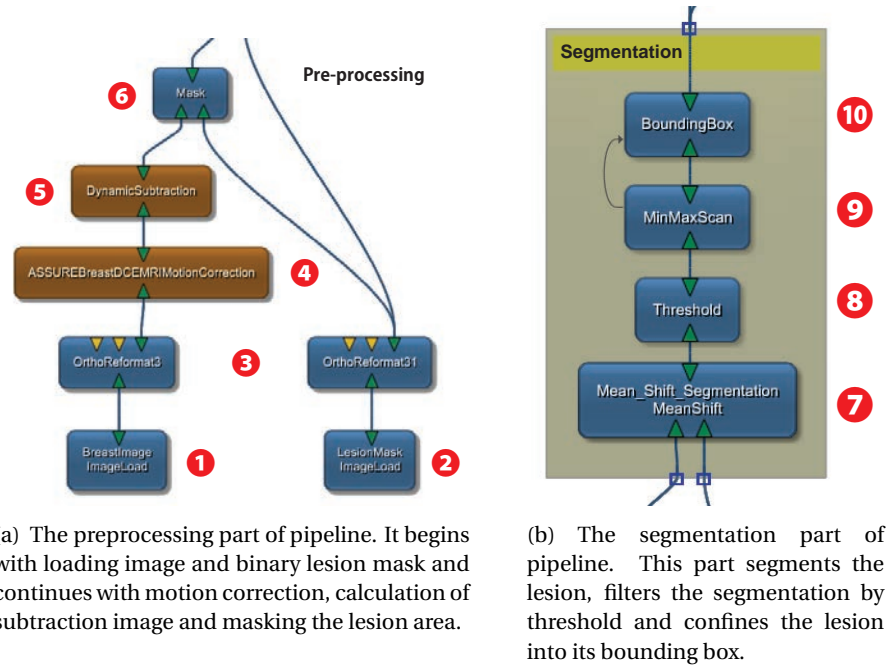


**Figure 4.4:** The two initial parts of this study's processing network in MeVisLab.

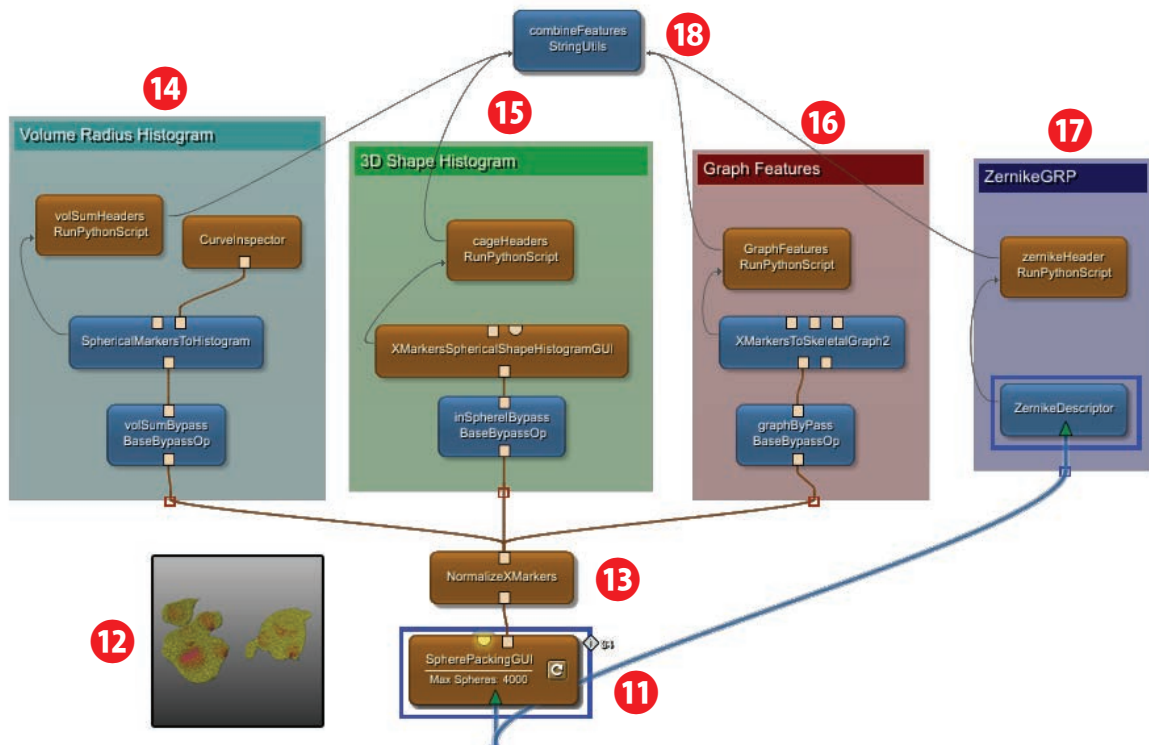


**Figure 4.5:** The third part of this study's processing pipeline in MeVisLab. In this part of the network the lesion binary volume is packed with spheres, then normalized and sent to several feature extraction modules. Finally, all feature vectors are combined to form a sample dataset.

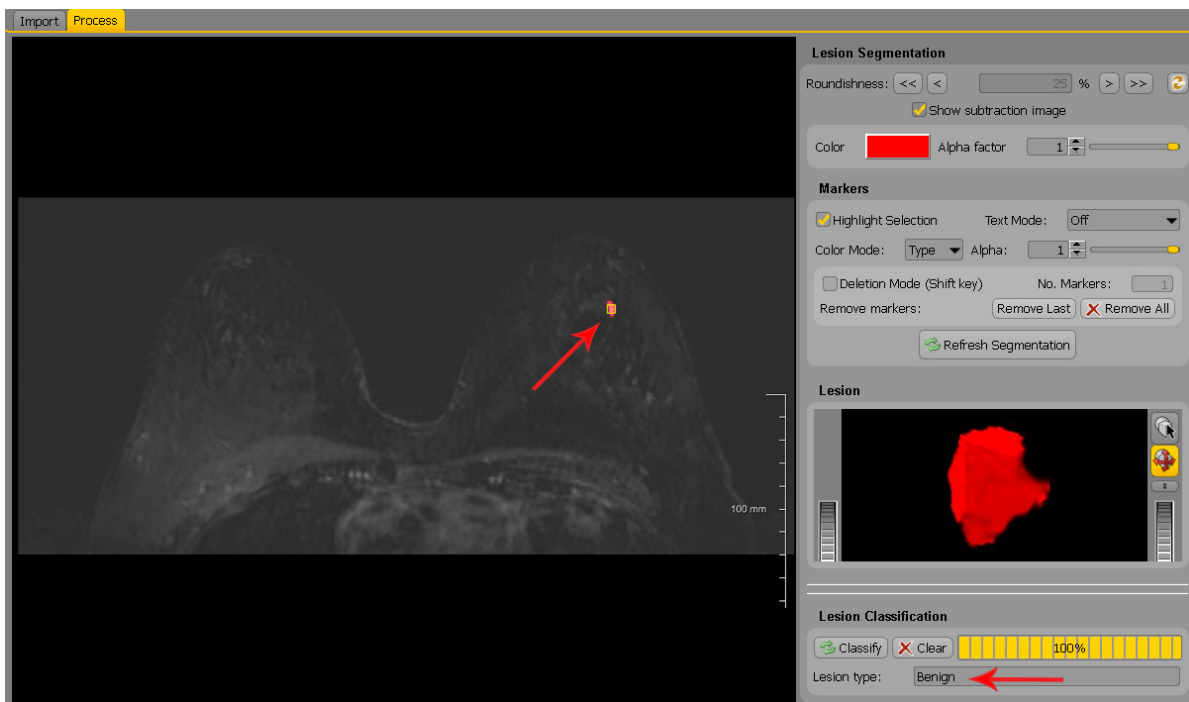


**Figure 4.6:** The application of the proposed framework as a module integrated into a Computer-Aided Diagnosis (CADx) tool. Using CADx tool, radiologists can analyse the MR scans using their subtraction image. By placing a seed point (**yellow rectangle** on the MR image) over any suspicious enhancement, the tool can segment the lesion area and show the corresponding 3D illustration (the **red 3D object** on right panel). Using lesion classification component, the CADx tool is able to detect the type of segmented lesion and show the results using either benign or malignant labels.



# 5

## EVALUATION AND RESULTS

To evaluate the performance of the presented method, a test dataset of MR images of 86 patients enclosing 106 lesion enhancements (38 benign and 68 malignant) was adopted. Only the subtracted image from the first two MR sequences ( $t_1 - t_0$ ) were processed of dynamic contrast enhanced images. The image resolution varied from  $256 \times 128 \times 80$  to  $512 \times 256 \times 16$  with different voxel sizes. The reference lesion binary masks were manually annotated by an experienced radiologist. Considering the lesion distribution, the radiologist annotated either one or several binary masks for a single lesion, thus he/she has specified the lesion type.

The lesions segmentations were acquired using a semi-automatic mean shift segmentation approach. By packing the obtained lesion volume with spheres, several feature vectors, including volume-radius histogram, 3D spherical shape histogram, and graph features from different aspects of the packed objects were extracted. As a rule of thumb, among most of the learning algorithms, the classification accuracy can be improved by combining features to gain a more effective classifier [110, 111]. Therefore, by providing a combination of acquired feature vectors, the all-inclusive dataset of features is assembled to train the classifier.

Experimentally it turned out that, even combining the sphere features with the invariants feature vector achieved from Zernike descriptor, excels the classification results. Therefore, Zernike invariants also were integrated into my combined features.

### 5.1. PERFORMANCE EVALUATION MEASURES

The quality measures of classification are taken from a confusion matrix which records correctly and incorrectly recognized examples for each class. Table 5.1 presents a confusion matrix for binary classification, where  $t_p$  are true positive,  $f_p$  are false positive,  $f_n$  are false negative, and  $t_n$  are true negative counts.

Class \ Recognized	as Positive	as Negative
Positive	$t_p$	$f_n$
Negative	$f_p$	$t_n$

Table 5.1: A confusion matrix for binary classification (Table taken from [112]).

Researchers have introduced different parameters to evaluate the performance of machine learning algorithms and classifiers. *Accuracy* is one of the most used empirical measures shows the probability of a sample being correctly classified; however, it does not distinguish between the number

of correct labels of different classes [112]:

$$accuracy = \frac{t_p + t_n}{t_p + f_p + f_n + t_n} \quad (5.1)$$

In contrast, there are the following two measures that separately estimate a classifier's performance on different classes:

$$sensitivity = \frac{t_p}{t_p + f_n} \quad (5.2)$$

and

$$specificity = \frac{t_n}{f_p + t_n} \quad (5.3)$$

The applications of sensitivity and specificity are often in bio- and medical and in studies involved image and visual data [112].

In many areas of applications, there is a class of special interest (usually *positive*). Other classes are either left as is (multi-class classification) or combined into one (binary classification). Here, the measures of choice is calculated on the positive class:

**Precision** is a function of true positives and examples misclassified as positives (false positives):

$$precision = \frac{t_p}{t_p + f_p} \quad (5.4)$$

**Recall** is a function of its correctly classified examples (true positives) and its misclassified examples (false negatives):

$$recall = \frac{t_p}{t_p + f_n} = sensitivity \quad (5.5)$$

**F-score** is evenly balanced when  $\beta = 1$ . It favors precision when  $\beta > 1$ , and recall otherwise.

$$F - measure = \frac{(\beta^2 + 1) * precision * recall}{\beta^2 * precision + recall} \quad (5.6)$$

**ROC** provides a comprehensive classifier performance evaluation as defined by:

$$ROC = \frac{P(x|positive)}{P(x|negative)} \quad (5.7)$$

$P(x|C)$  denotes the conditional probability that a data entry has the class label  $C$ . An *ROC curve* plots the classification results from the most positive classification to the most negative classification [112, 113].

In a ROC curve the *true positive rate* (Sensitivity) is plotted in function of the *false positive rate* (100-Specificity) for different cut-off points of a parameter. In this curve each point represents a sensitivity/specificity pair corresponding to a particular decision threshold. The area under the ROC curve (AUC) is a measure of how well a parameter can distinguish between two diagnostic groups (diseased/normal) [114].

To evaluate the machine learning methods, the results of three popular classifiers, including Adaboost, Naive Bayes, and Random Forests were compared using Weka software version 3.6 [115]. As can be seen in Figure 5.1, Random Forest classifier outperforms the other two regarding the average results in almost all factors.

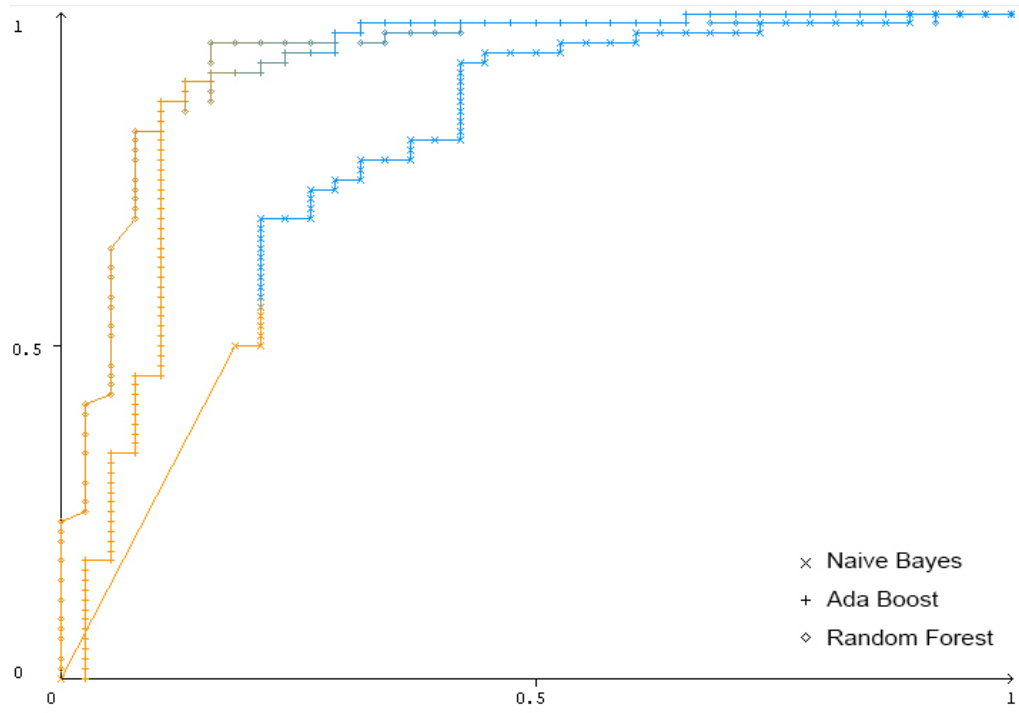
In the results statistics

- **TP Rate** is the rate of *true positives* in results.
- **FP Rate** is the rate of resulted *false positives*.
- **Precision** is defined as the fraction of elements correctly classified as positive out of all the elements the algorithm classified as positive (see Equation 5.4).
- **Recall** is the fraction of elements correctly classified as positive out of all the positive elements (see Equation 5.5).
- **F-Measure** is a weighted average of the F-Measures of the classes, weighted by the proportion of how many elements are in each class (see Equation 5.6).
- **ROC Area** is the area under the curve (AUC), the evaluation for the classifier performance (see Equation 5.7).

The 10-fold cross validation method [116] is used among other several methods available (e.g. thresholds, mean precision, and precision above) to evaluate the RF classifier results. Figure 5.2 shows *OOB (out-of-bag) ROC curve* and *error rate* graphs obtained from the RF classifier results. The *OOB data* is used to get a running unbiased estimate of the classification error as trees are added to the forest. Thus, it is used to get estimates of variable importance [117]. *Error rate* is progressively shown for the number of trees built which is useful to decide the optimum number of trees to build the forest.

Totally, 252 features obtained from several mentioned methods, which were combined as an all-inclusive feature vector. Here, the composition of this feature vector with the best optimum parameters and number of features from each method are presented:

- **The first** part of feature vectors includes 50 features denotes the **volume-radius histogram** with the labels *VolRadHisto01 – VolRadHisto50*. Several evaluations are done in order to acquire the optimum number of histogram bins using only volume-radius histogram features and regardless of other attributes. The results can be seen in Figure 5.3 the maximum accuracy acquired from dividing the spheres radius range into 50, 55 and 80 bins for the histogram apart from other features. Therefore, the value of 50 bins was chosen as the lowest number of bins to gain the maximum accuracy results.
- **The second** part of feature vectors includes 111 features denotes the **3D spherical shape histogram** with the labels *ShapeHisto01 – ShapeHisto110* and *ShapeHistoFill*. The first 110 features resulted from partitioning the enclosing spherical wireframe by 11 rings, 10 shells, and 1 sector ( $11 \times 10 \times 1 = 110$ ). These values are obtained from a brute-force search method to acquire the best results (see Figure 5.4). In this group of features, the last one represents the proportion of the enclosing wireframe sphere occupied by internal spheres' volumes. A further evaluation showed that among four different methods to decide the center point of enclosing sphere (see Figure 3.15), placing the center point in the *middle of the two most distant* internal spheres provides the best accuracy.
- **The third** part of feature vectors includes 72 features denotes the **Zernike moments** with the labels *Zenike01 – Zenike72*. This number is obtained from the Zernike moments descriptors with the *Maximum Order* of 15, again obtained by brute-force searching the best accuracy



(a) The ROC curve comparison

ML Algorithm	TP Rate	FP Rate	Precision	Recall	F-Measure	ROC Area	Class
Random Forest	0.956	0.184	0.903	0.956	0.929	0.929	0 (Malignant)
	0.816	0.044	0.912	0.816	0.861	0.929	1 (Benign)
	0.906	0.134	0.906	0.906	0.904	0.929	Weighted Avg.
Naive Bayes	0.559	0.211	0.826	0.559	0.667	0.781	0 (Malignant)
	0.789	0.441	0.5	0.789	0.612	0.68	1 (Benign)
	0.642	0.293	0.709	0.642	0.647	0.745	Weighted Avg.
AdaBoost	0.912	0.158	0.912	0.912	0.912	0.899	0 (Malignant)
	0.842	0.088	0.842	0.842	0.842	0.899	1 (Benign)
	0.887	0.133	0.887	0.887	0.887	0.899	Weighted Avg.

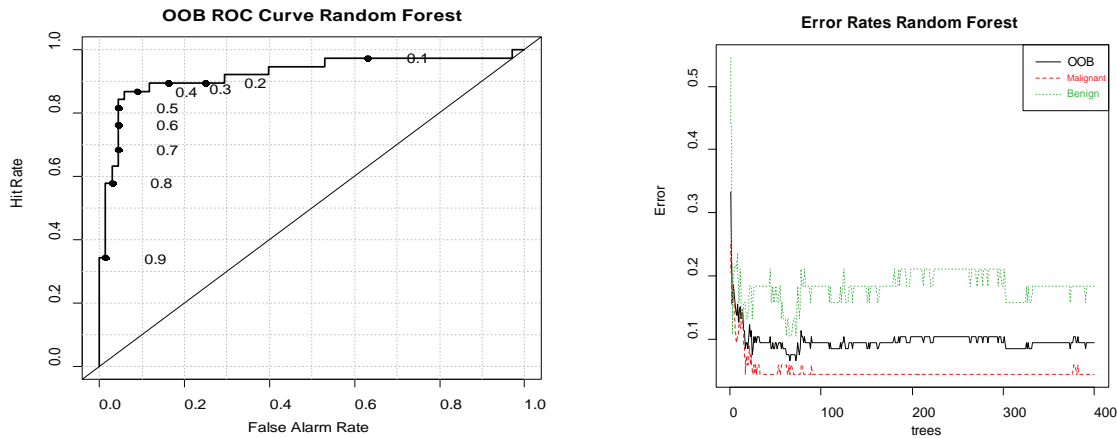
(b) The comparison of classification results in different machine learning algorithms

**Figure 5.1:** The comparison of classification results between three classifiers. Here, the results of three popular classifiers were compared with my dataset using Weka v3.6 software [115]. Random forest outperforms the other two. (a) shows the ROC curve of each classifier. (b) shows the statistical classifiers results.

among the classification results (see Figure 5.5).

- **The forth** part of feature vectors includes 15 features denotes the **graph features**. The features' labels consist of two parts: the word "Graph\_" plus the name of the graph feature, i.e. *Graph\_edgeDensity* or *Graph\_compactnessIndexCP*. Again by brute-force searching for the best combination of parameters, *Gabriel Graph* was chosen to get the highest accuracy among all the graph structures.

Furthermore, by trying different graph clustering parameters, the best results were acquired from the *K-Max* clustering parameter equal to  $n$ . This means the features acquired from a unified graph structure with *no clustering*. This gives the best classification accuracy for graph features.



(a) Random Forest ROC curve based on OOB (out-of-bag). The prediction for each observation in the training dataset.

(b) Random Forest error rate progressively for the number of trees built. Useful to decide the optimum number of trees to build.

**Figure 5.2:** Charts of Random Forest analysis.

## FEATURE SELECTION

As a rule of thumb, it is important for a machine learning algorithm to generate decision rules that have high predictability or reliability. Using unordered rule sets, can arise conflicts between the rules, i.e., two or more rules cover the same example but predict different classes [118]. It is therefore important to use mechanisms to prevent over-fitting of the training data [111]. Feature subset selection and feature ranking are common ways to prevent this matter [119].

For that reason, feature selection based on their importance and their impact on the classification results is adopted to select a subset of relevant features to construct the model. Rattle: A Graphical User Interface for Data Mining using R [120] is used to get the top 30 feature ranking. In Rattle variable importance is described by the *Mean Decrease Accuracy* (MDA) criterion or the *Mean Decrease Gini* (MDG or Gini index), and it represents a ranking of variables in terms of their importance as predictors. MDG reflects the overall goodness of fit, while the MDA depends on how well the model actually predicts. The two indices measure different things, but they are related [121]. The MDA is thought to be a better measure [122].

Figure 5.6 shows the variable importance plot obtained from RF using Rattle [120]. It can be seen that among the 30 most important features in both MDA and MDG rankings, the first place belongs to the features of *volume-radius histogram* method (black features). *Zernike moments* features are in the second place of importance, especially in MDA ranking. The third rank belongs to the *graph features*, including only three features of *New Compactness Index CP\**, *linear structure* and *Dunn's Index*. As not many *spherical shape histogram* features can be seen among the most important features, they place forth.

Accordingly, the number of feature space can be reduced by removing the redundant one from the dataset. Some classifiers can be misled by irrelevant or redundant such as functionally dependent, attributes. Hence, criteria such as the number of irrelevant or redundant attributes could also be considered [123]. As a result, only the features in top 30 rankings were kept to do the another evaluation and the rest were excluded from the training dataset.

Table 5.3 shows the classification results and some evaluation statistics using only the top 30 features acquired from both MDA and MDG feature rankings. Notice the *Area under ROC* values

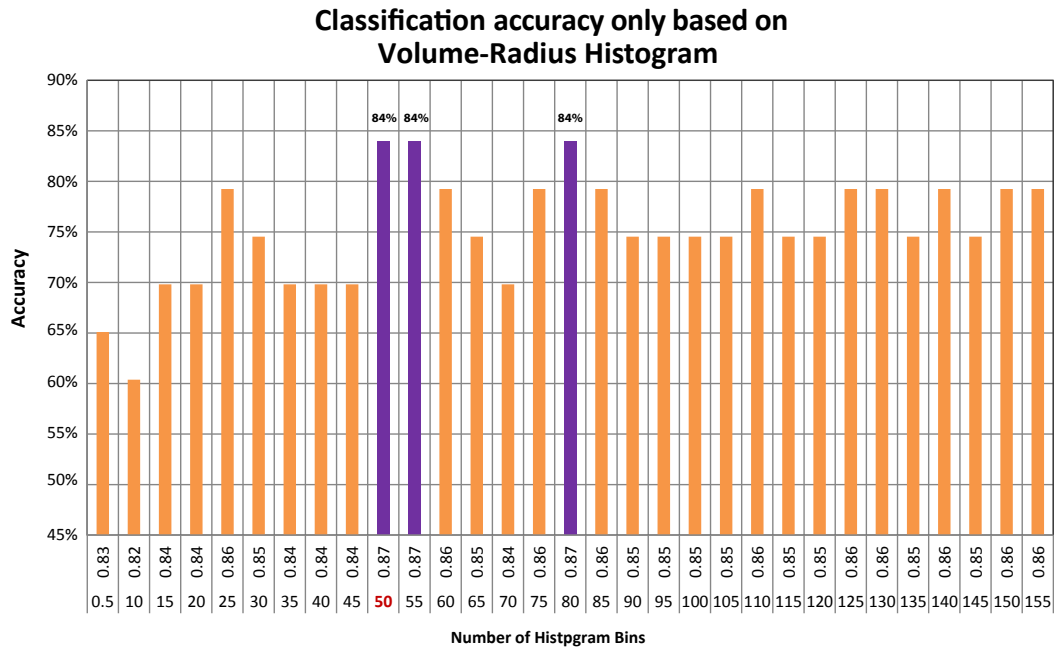


**Figure 5.3:** Classification accuracy only based on Volume-Radius Histogram features. Using a *brute-force search* several bin values were tried to obtain the best classification accuracy. The maximum accuracy (84%) was acquired from 50, 55 and 80 number of bins for volume-radius histogram method isolated from other features.

that has increased in comparison to the evaluation with all 252 attributes and is also slightly higher in MDA ranking. Therefore, the top 30 most important features based on the MDA ranking were chosen to do the further optimizations.

## PRINCIPAL COMPONENT ANALYSIS (PCA)

Principal component analysis (PCA) is a well-known method for feature extraction. PCA linearly transforms a high-dimensional input vector into a low-dimensional one whose components are uncorrelated by calculating the eigenvectors of the covariance matrix of the original inputs [124].

The new components are called principal components. By using only the first several eigenvectors sorted in descending order of the eigenvalues, the number of principal components can be reduced. It is the dimensional reduction characteristic of PCA method [124].

Weka software has been used to perform principal components analysis and transformation of data in conjunction with a Ranker search. In this software dimensionality reduction is accomplished by choosing enough eigenvectors to account for some percentage of the variance in the original data - default value is 0.95 (95%). Attribute noise can be filtered by transforming to the PC space, eliminating some of the worst eigenvectors, and then transforming back to the original space [125].

After applying the principal component analysis on the top 30 attributes and choosing the variance of 90% for eigenvectors, the best results were achieved. PCA transformed the 30 attributes in the dataset to the following *five* principal components with some weighting applied:

1.  $-0.244volSum07 - 0.244volSum11 - 0.243volSum06 - 0.243volSum08 - 0.243volSum10$
2.  $0.337Zenike08 + 0.336Zenike09 + 0.336Zenike04 + 0.335Zenike03 + 0.335Zenike01$
3.  $0.636ShapeHisto80 + 0.63ShapeHisto69 - 0.341ShapeHisto28 - 0.128Zenike07 - 0.099volSum44$

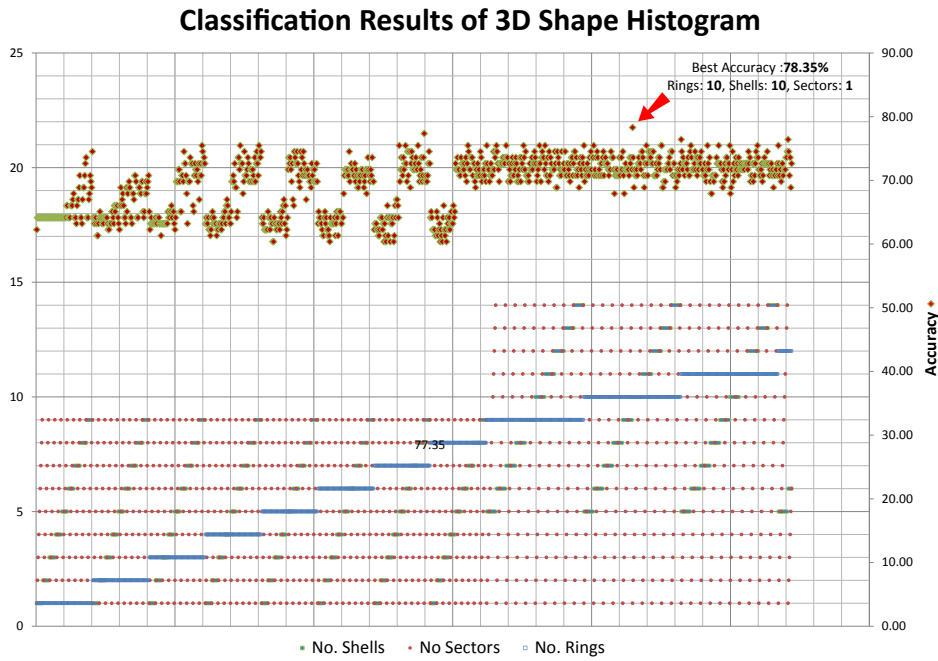


**Figure 5.4:** Classification accuracy only based on 3D shape Histogram features. Using a *brute-force search* method, different combination of the number of shells, rings and sectors were tried to obtain the best classification accuracy. In the plot, the different combination of dots is shown in the lower part. Each dot shows the number of **shells** (in green), the number of **sectors** (in red) and the number of **rings** (in blue). The corresponding classification accuracy results of the sections combination are placed in the higher part of the plot. The **maximum accuracy (78.35%)** is acquired from the combination of 11 shells, 10 rings and 1 sector to form the spherical wireframe. These results show the accuracy of this method apart from other feature extraction methods.

4.  $0.651 volSum44 - 0.468 Graph\_newCP^* - 0.35 Graph\_Dunn'sIndex - 0.264 Graph\_LinearStructure - 0.167 ShapeHisto28$
5.  $0.677 volSum44 + 0.388 ShapeHisto28 + 0.375 Graph\_newCP^* + 0.284 Graph\_Dunn'sIndex + 0.232 Graph\_LinearStructure$

Using only the mentioned five principal components - which are the combination of top 30 features - creating RF model using Weka only takes *0.04 seconds*. This time shows a significant decrease in comparison to the time needed for creating the model before applying PCA, which was *0.03 seconds*. Using all the 252 features with no ranking and normalization this time was 0.06 seconds (see Table 5.3).

The summary of the classifier evaluation results using the final five features can be seen in the following tables 5.3 and 5.2:

As mentioned earlier, the area under the receiver operating characteristic (ROC) curve (AUC) is used as a very popular performance measure for classifiers [126], which serves as a quantitative evaluation measure for the processing pipeline [10]. It is a measure of difference between distributions of the estimated probability that an object belongs to class 0 and class 1. The classification rule will generally be better the more these two distributions differ. It concentrates attention on how well the rule differentiates between the distributions of the two classes. It is not influenced by external factors which depend on the classification usage [127].

To sum up, the proposed method in differentiating between malignant and benign lesions, achieved the accuracy of 89.62%, precision of 90.1%, and area under the ROC curve (AUC) of 0.972 using Random Forest classifier. The processing time for the trained classifier to provide the results is around

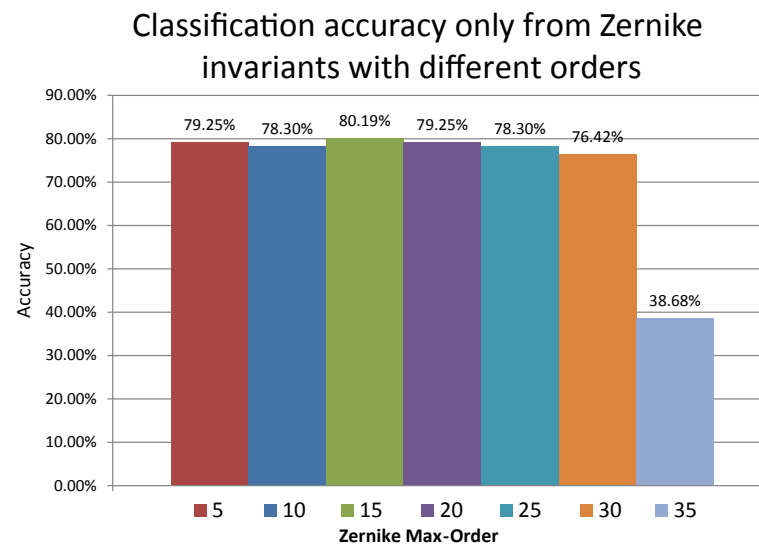


**Figure 5.5:** Classification accuracy only based on Zernike moments features. Using *exhaustive search*, different Maximum order values were tried to obtain the best classification accuracy. The **maximum accuracy (80.19%)** is acquired from the Zernike moments with maximum order equal to 15. These results show the accuracy of this method apart from other feature extraction methods.

4.2 seconds using a 3.5 GHz Intel CPU and a GeForce GTX 680 graphics card.

Figure 5.7 shows some of samples in evaluation which are correctly classified ((a), (b), (c), (d)), along with the cases which are classified incorrectly ((e), (f)). Several illustrations can be seen in the figure which represent different steps of feature extraction process.

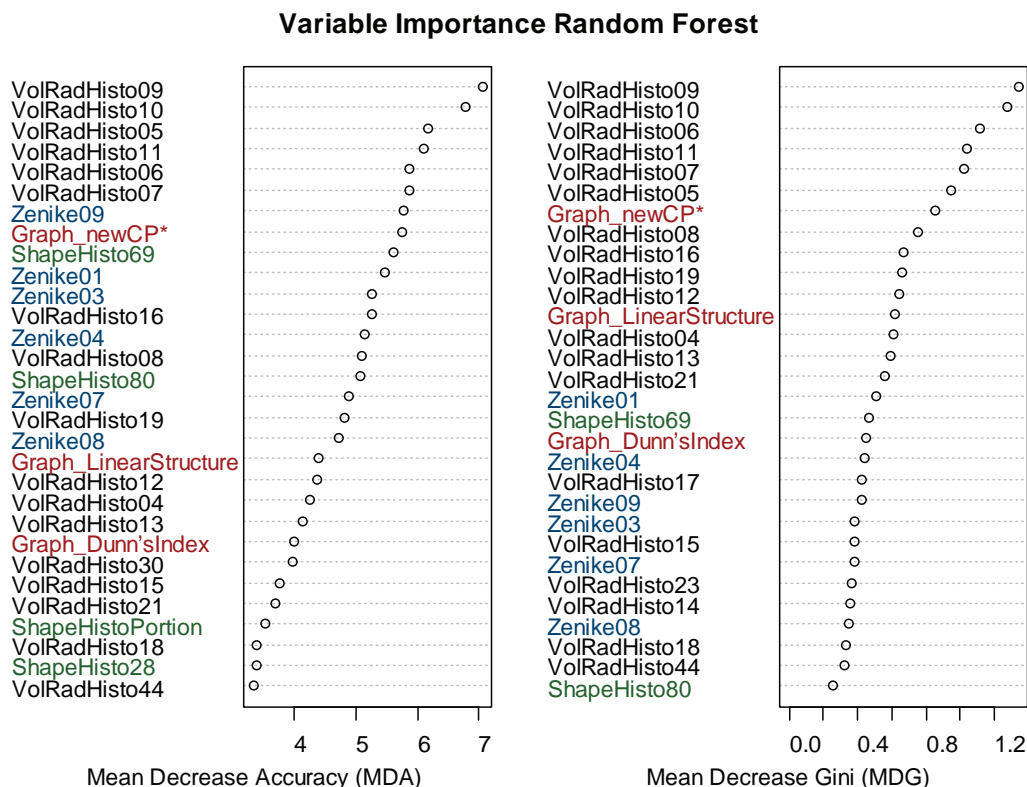


**Figure 5.6:** Variable importance in Random Forest evaluation. **On left**, the *Mean Decrease Accuracy* ranking depends on how well the model actually predicts. **On right**, the *Mean Decrease Gini* ranking reflects the overall goodness of fit. The two indices measure different things, but they are related [121].

Feature set	TP Rate	FP Rate	Precision	Recall	F-Measure	ROC Area	Class	a	b	
<b>All features</b>	0.956	0.211	0.89	0.956	0.922	0.9	0	64	4	a = 0
	0.789	0.044	0.909	0.789	0.845	0.9	1	6	32	b = 1
Avg.	0.896	0.151	0.897	0.896	0.894	0.9				
<b>MDA features</b>	0.941	0.184	0.901	0.941	0.921	0.957	0	64	4	a = 0
	0.816	0.059	0.886	0.816	0.849	0.957	1	7	31	b = 1
Avg.	0.896	0.139	0.896	0.896	0.895	0.957				
<b>MDG features</b>	0.956	0.184	0.903	0.956	0.929	0.963	0	65	3	a = 0
	0.816	0.044	0.912	0.816	0.861	0.963	1	7	31	b = 1
Avg.	0.906	0.134	0.906	0.906	0.904	0.963				
<b>PCA on MDG</b>	0.941	0.211	0.889	0.941	0.914	0.965	0	64	4	a = 0
	0.789	0.059	0.882	0.789	0.833	0.965	1	8	30	b = 1
Avg.	0.887	0.156	0.887	0.887	0.885	0.965				
<b>PCA on MDA</b>	0.941	0.184	0.901	0.941	0.921	0.972	0	64	4	a = 0
	0.816	0.059	0.886	0.816	0.849	0.972	1	7	31	b = 1
Avg.	0.896	0.139	0.896	0.896	0.895	0.972				

(a) Detailed accuracy by class

(b) Confusion matrix

**Table 5.2:** (a) shows evaluation results of random forest classification on all the features, after applying MDA, MDG, PCA on MDA features subset and PCA on MDG features subset. (b) shows the classification results in classifier's output confusion matrix. The row indicates the true class, the column indicates the classifier output. Each entry is the number of instances of *row* that were classified as *column*.

<b>Evaluation Statistic</b>	<b>All features</b>	<b>MDA features</b>	<b>MDG features</b>	<b>PCA on MDG</b>	<b>PCA on MDA</b>
Total Number of Instances	106	106	106	106	106
Number of Attributes	252	30	30	5	5
Correctly Classified Instances	95 (89.62%)	95 (89.62%)	96 (90.56%)	94 (88.67%)	95 (89.62%)
Incorrectly Classified Instances	11 (10.37%)	1 (10.377%)	10 (9.43%)	12 (11.32%)	11 (10.37%)
Kappa statistic	0.7676	0.7704	0.79	0.748	0.7704
Mean absolute error	0.233	0.169	0.1592	0.1686	0.2659
Root mean squared error	0.3166	0.2752	0.2659	0.2769	0.2651
Relative absolute error	50.5503 %	36.6541 %	34.5461 %	36.5722 %	35.4876 %
Root relative squared error	65.9921 %	57.3609 %	55.4142 %	57.7064 %	55.2579 %
Time to build RF model	0.06	0.04 s	0.05 s	0.03 s	0.03 s
<b>Area under ROC (AUC)</b>	<b>0.9</b>	<b>0.957</b>	<b>0.963</b>	<b>0.965</b>	<b>0.972</b>

**Table 5.3:** Random forest evaluation results using MDA and MDG feature selections and also applying PCA on their results using Weka software. **All features column** shows the evaluation statistics acquired from all the features with no feature selection. **MDA features column** shows the classification statistics acquired after feature selection of Mean Decrease Accuracy (MDA) ranking. **MDG features column** shows the same statistics for Mean Decrease Gini (MDG) variable importance. **PCA on MDG column** shows the RF evaluation statistics after applying Principal Component Analysis (PCA) on the MDG feature selection. **PCA on MDA column** shows the RF evaluation results after applying PCA on MDA feature ranking. Based on the AUC values, MDG shows slightly better results than MDA; however, after applying PCA on both, the AUC of MDA method is slightly higher than AUC of MDG.

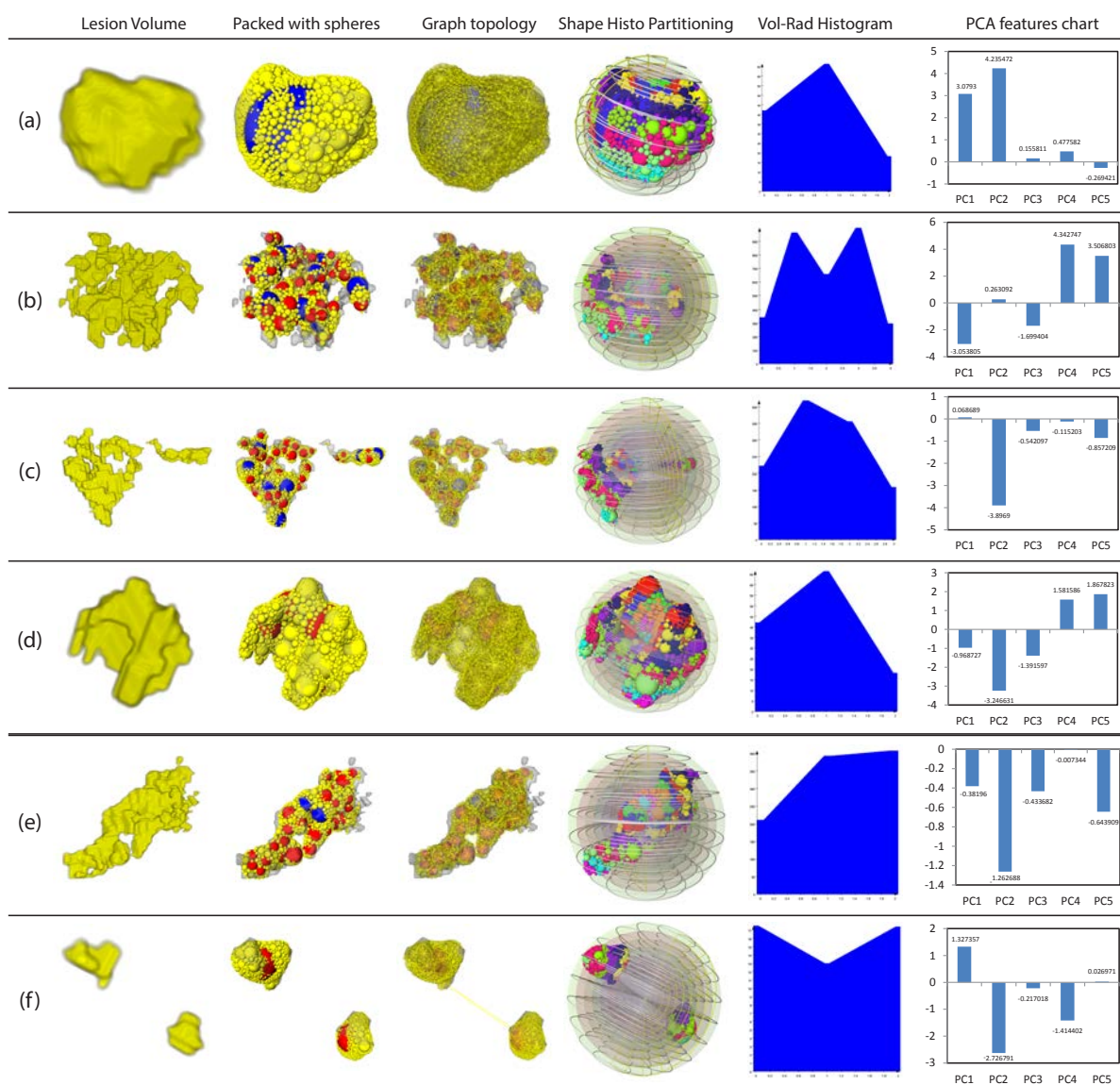


**Figure 5.7:** Classification evaluation sample data. In this figure several steps of feature extraction are illustrated for different benign and malignant cases. From left to right: the original lesion volume, the packed lesion geometry with spheres, the graph topology based on connecting the center points, enclosing spherical wireframe that partitions lesion's surrounding space to acquire elements (embedded spheres) distributions, volume-radius histogram, and the corresponding chart based on the Principal Components (PC) attributes of the lesion are represented. (a) & (b) show two examples of *true positive* cases which their types are benign and they are classified as benign too. (c) & (d) show two examples of *true negative* cases which their types are malignant and they are classified as malignant too. (e) show an examples of *false negative* case which its type is malignant but it is classified as benign. (f) show an examples of *false negative* case which its type is benign but it is classified as malignant.



# 6

## SUMMARY AND CONCLUSIONS

This chapter briefly reviews the thesis, summarizes the key contributions and findings, outlines failed experiments and the limitations of the research undertaken, and discusses opportunities for future research.

### THESIS SUMMARY

**Chapter 1** provided an introduction to the field of the research and the following statement of the goal underlying the research:

*-classification of the non-mass lesions to benign or malignant types, using merely the morphological features.*

In order to achieve that goal, the following approach was proposed:

1. *Using the method of sphere packing to acquire multiple morphological features of lesion structures.*
2. *Evaluating the performance of the new method using real clinical breast MRI data.*

**Chapter 2** presents some background knowledge of dynamic contrast-enhanced MR imaging, breast MRI, breast lesions and their kinetic, morphological and textural analysis. The chapter followed by a literature review which states that not many works are done to classify non-mass breast lesions.

**Chapter 3** presents the materials used and the method outline. The processing steps starting from motion compensation and lesion segmentation pre-processing and continues by sphere packing the lesions volume, normalization and feature extraction from Volume-Radius histogram, 3D spherical shape histogram, Graph topological and Zernike invariants methods. Finally, the Random Forest algorithm is used to evaluate the results using 10-fold cross validation over the dataset of the combination of all the features.

**Chapter 4** presents the proceeding pipeline used in *MeVisLab* software and the integration of the work in a CADx system.

**Chapter 5** presents the evaluation results in several steps before and after applying feature selection methods. The evaluations are done using the Random Forest machine learning since it outperformed the other two algorithms used to compare their performance.

## 6.1. FAILED EXPERIMENT

Here, an experiment which was done to acquire different type of features is pointed out. Since the classification results of this method was not satisfactory, its feature was excluded from the classifier's dataset, thus it is considered as failed experiments.

### LESION ALIGNMENT TOWARD THE NIPPLE POSITION

Based on the literature, the distributions of the mammary gland and the ductal system of the breast are approximated to linear structures in a radial direction toward the nipple [128]. Therefore, in a normal breast, the distributions of lesions that extend along the duct are also in the direction toward the nipple [129]. This characteristic of lesion was adopted as a measure to specify their malignancy.

Since cancerous lesions have a distribution pattern among the surrounding tissue and the direction of the distribution pattern is generally toward the nipple, this could be a significant feature, especially for malignant lesion detection. Accordingly, by detecting the nipple position in the breast containing the lesion and acquiring its distribution direction, their alignment can be measured.

In order to get the orientation of each lesion, Principal component analysis (PCA) [130] is used to get the first eigenvector of the geometry starting from the centroid point of the lesion. Instead of directly computing the PCA from volumetric lesion, the eigenvector calculation is done on the internal spheres from the sphere packing step. The nipple position in each breast is also I also extracted and the nipple vector was drawn going from the lesion's centroid toward the nipple seed point (see Figure 6.1).

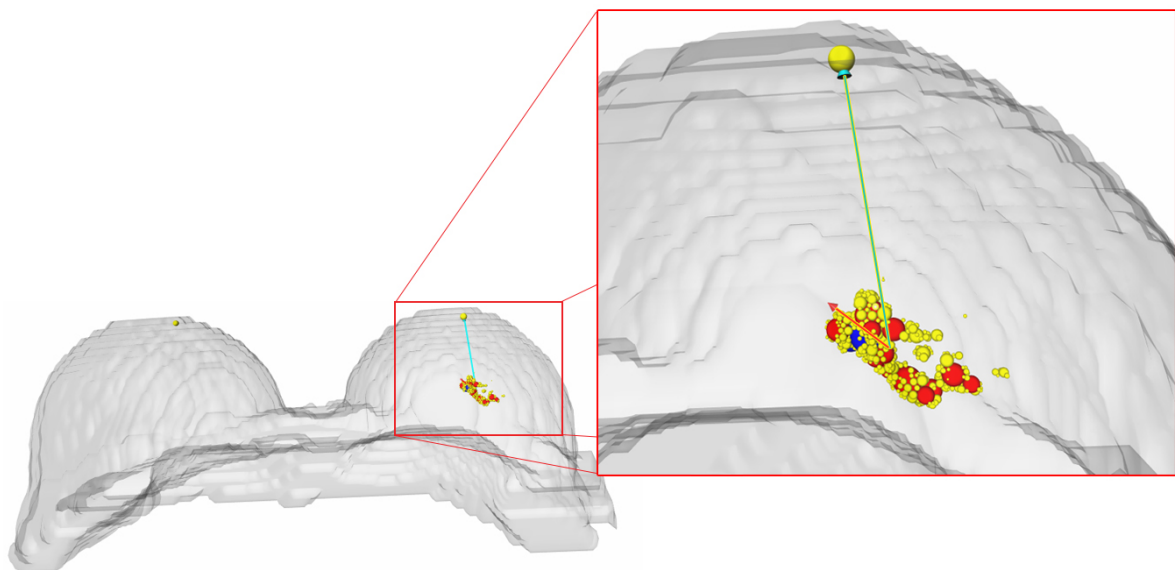


**Figure 6.1:** Distribution orientation of the lesion and nipple direction. The figure shows a sphere packed lesion inside the breast. The **yellow sphere** on the apex of each breast represents the nipple position. **Red vector** inside the packed lesion is the first PCA eigenvector shows the main distribution orientation of internal spheres. **Cyan vector** which goes from the centroid of the lesion toward the nipple position is the nipple vector. The alignment of these two vectors could be used as a feature to classify malignant lesion.

Having nipple vector and first eigenvector are enough to acquire their alignment. It is done by first normalizing the both vectors and computing their dot product using Equation 6.1, which represents this concept in  $n$  dimensional space. The value of dot production between two vectors is equal to 1, if they are *parallel* (fully aligned) or it is 0, if two vectors are *orthogonal*.

$$\mathbf{A} \cdot \mathbf{B} = \sum_{i=1}^n A_i B_i = A_1 B_1 + A_2 B_2 + \dots + A_n B_n \quad (6.1)$$

The classification evaluation results only based on the dot product value feature can be seen in the following tables 6.1 and 6.2:

RF statistics	Feature results
Total Number of Instances	106
Number of Attributes	1
Correctly Classified Instances	55 (51.88%)
Incorrectly Classified Instances	51 (48.11%)
Kappa statistic	-0.0289
Mean absolute error	0.4834
Root mean squared error	0.596
Relative absolute error	103.6718%
Root relative squared error	123.4462%
<b>Area under ROC (AUC)</b>	<b>0.455</b>

**Table 6.1:** Random forest evaluation statistics of lesion orientation toward the nipple.

TP Rate	FP Rate	Precision	Recall	F-Measure	ROC Area	Class	a	b
0.612	0.641	0.621	0.612	0.617	0.455	0	41	26
0.359	0.388	0.35	0.359	0.354	0.455	1	25	14
Avg.	0.519	0.521	0.519	0.52	0.455			

(a) Detailed accuracy by class

(b) Confusion matrix

**Table 6.2:** (a) shows random forest classification accuracy for lesion orientation toward the nipple. (b) shows the classification results in classifier's output confusion matrix in which the row indicates the true class, the column indicates the classifier output. Each entry is the number of instances of *row* that were classified as *column*.

The acquired value of accuracy is 51.8% with the AUC of 0.45. The AUC value is always between 0 and 1, since it is a portion of the area of the unit square. However, because random guessing produces the diagonal line between (0, 0) and (1, 1), which has an area of 0.5, no realistic classifier should have an AUC less than 0.5 [131]. As a result of low accuracy and low AUC, the mentioned attempt is marked as failed experiment.

## 6.2. OPPORTUNITIES FOR FURTHER WORK

The proposed classification method may potentially be improved by alternating several implementation steps:

- **Segmentation step:** The used semi-automatic mean shift segmentation algorithm needed the user interaction and decision on the level of thresholding. As a result, the segmentation could be very subjective. To overcome this weakness in the future work, *Watershed Transform* based strategies for image segmentation [132] or *Region Growing* method using manual seed points [133] can be adopted.
- **Sphere packing step:** The volumetric objects were converted to mesh geometries regardless of the measurement units. A mapping measure of lesion's volumetric object to sphere units

could be obtained to perform a better packing defining the maximum or minimum of the spheres radius values.

- **Normalization step:** The lesion volumes could be normalized before sphere packing step instead of normalizing the spheres acquired from packing. Apart from that, the alignment-normalization (pose registration) processes could be used to align object from internal spheres to its canonical coordinate frame before extracting features [62].
- **Volume-Radius histogram step:** In addition to summation of spheres' volumes in histogram, the uncovered area of the spheres could also be investigated to acquire more features.
- **3D spherical histogram step:**
  1. Instead of counting the center points of spheres in each section of the enclosing spherical wireframe, either the volume of internal spheres bounded by each fragment or the number of spheres full bounded by that fragment could be used for histogram values.
  2. To locate the center point of the enclosing spherical wireframe, several more possibilities could be investigated, e.g. placing the center point among the 10% of the biggest or smallest spheres.
  3. The orientation of the surrounding spherical wireframe could be determined using several methods. For instance, *Principal component analysis (PCA)* and eigenvectors could be used as reference for orientation and eigenvalues could be used to define its radius.
- **Graph topological features step:** More topological features using more graph structures could be investigated such as graph symmetry.
- **Zernike Invariants step:** The Zernike moments could be acquired from the internal spheres as an object rather than voxelized lesion volume.
- **Lesion alignment toward the nipple (failed experiment):** Other eigenvectors could be investigated to prove the efficiency of the method. The lesion volume could also be used to investigate its alignment with the nipple vector.
- **Evaluation step:** To compare the machine learning algorithms, more of ML methods could be investigated. For feature selection, also more feature raking algorithms could be considered with various number of top attributes.

Future work could also consider the combination of kinetical or textural features in order to obtain a higher performance. In that case, the classification of several sub types of benign or malignant lesions also could be investigated.

### 6.3. LIMITATIONS

In this study several limitations were encountered, these included:

- Regarding the amount of work needed to be done for this study, the time limit of a master thesis was insufficient to achieve all defined the goals.
- A bigger dataset with more lesion samples could be examined to get even better evaluation outcomes.
- The “ground truth” lesions mask used in the study originated from a single expert reader's manual segmentation. Ideally, several datasets from different experts could be used to account for intersubject variability.

# BIBLIOGRAPHY

- [1] P. Kawalec, S. Łopuch, and A. Mikrut, *Effectiveness of Targeted Therapy in Patients With Previously Untreated Metastatic Breast Cancer: A Systematic Review and Meta-Analysis*, *Clinical Breast Cancer* (2014), 10.1016/j.clbc.2014.10.006.
- [2] P. Skaane, A. I. Bandos, R. Gullien, E. B. Eben, U. Ekseth, U. Haakenaasen, M. Izadi, I. N. Jebsen, G. Jahr, M. Krager, L. T. Niklason, S. Hofvind, and D. Gur, *Comparison of Digital Mammography Alone and Digital Mammography Plus Tomosynthesis in a Population-based Screening Program*, *Radiology* **267**, 47 (2013).
- [3] V. Kalles, G. C. Zografos, X. Provatopoulou, D. Koulocheri, and A. Gounaris, *The current status of positron emission mammography in breast cancer diagnosis*. *Breast cancer (Tokyo, Japan)* **20**, 123 (2013).
- [4] S. V. Sree, E. Y.-K. Ng, R. U. Acharya, and O. Faust, *Breast imaging: A survey*. *World journal of clinical oncology* **2**, 171 (2011).
- [5] F. Arvidsson, Jonathan and Johansson, *Automatic detection of 3D breast lesions in dynamic contrast-enhanced MR images*, Ph.D. thesis, Chalmers University of Technology (2011).
- [6] C. K. Kuhl, P. Mielcareck, S. Klaschik, C. Leutner, E. Wardelmann, J. Gieseke, and H. H. Schild, *Dynamic breast MR imaging: are signal intensity time course data useful for differential diagnosis of enhancing lesions?* *Radiology* **211**, 101 (1999).
- [7] C. D. Lehman, J. D. Blume, P. Weatherall, D. Thickman, N. Hylton, E. Warner, E. Pisano, S. J. Schnitt, C. Gatsonis, M. Schnall, G. A. DeAngelis, P. Stomper, E. L. Rosen, M. O'Loughlin, S. Harms, and D. A. Bluemke, *Screening women at high risk for breast cancer with mammography and magnetic resonance imaging*. *Cancer* **103**, 1898 (2005).
- [8] H. Rabiei, A. Mahloojifar, and M. E. Farmer, *Providing context for tumor recognition using the wrapper framework*, 2007 4th IEEE International Symposium on Biomedical Imaging: From Nano to Macro - Proceedings, 1252 (2007).
- [9] Y. Gal, A. Mehnert, A. Bradley, K. McMahon, and S. Crozier, *Automatic Segmentation of Enhancing Breast Tissue in Dynamic Contrast-Enhanced MR Images*, *Digital Image Computing Techniques and Applications*, 124 (2007).
- [10] S. Hoffmann, J. Shutler, M. Lobbes, B. Burgeth, and a. Meyer-Bäse, *Automated analysis of non-mass-enhancing lesions in breast MRI based on morphological, kinetic, and spatio-temporal moments and joint segmentation-motion compensation technique*, *EURASIP Journal on Advances in Signal Processing* **2013**, 172 (2013).
- [11] S. Agliozzo, M. De Luca, C. Bracco, a. Vignati, V. Giannini, L. Martincich, L. a. Carbonaro, a. Bert, F. Sardanelli, and D. Regge, *Computer-aided diagnosis for dynamic contrast-enhanced breast MRI of mass-like lesions using a multiparametric model combining a selection of morphological, kinetic, and spatiotemporal features*, *Medical Physics* **39**, 1704 (2012).

- [12] G. M. Grimsby, R. Gray, A. Dueck, S. Carpenter, C. C. Stucky, H. Aspey, M. E. Giurescu, and B. Pockaj, *Is there concordance of invasive breast cancer pathologic tumor size with magnetic resonance imaging?* *American Journal of Surgery* **198**, 500 (2009).
- [13] I. M. a. Obdeijn, C. E. Loo, A. J. Rijnsburger, M. N. J. M. Wasser, E. Bergers, T. Kok, J. G. M. Klijn, and C. Boetes, *Assessment of false-negative cases of breast MR imaging in women with a familial or genetic predisposition*, *Breast Cancer Research and Treatment* **119**, 399 (2010).
- [14] E. L. Rosen, S. a. Smith-Foley, W. B. DeMartini, P. R. Eby, S. Peacock, and C. D. Lehman, *BI-RADS MRI enhancement characteristics of ductal carcinoma in situ*, *Breast Journal* **13**, 545 (2007).
- [15] N. Sakamoto, M. Tozaki, K. Higa, Y. Tsunoda, T. Ogawa, S. Abe, S. Ozaki, M. Sakamoto, T. Tsuruhara, N. Kawano, T. Suzuki, N. Yamashiro, and E. Fukuma, *Categorization of non-mass-like breast lesions detected by MRI*, *Breast Cancer* **15**, 241 (2008).
- [16] R. Weller and G. Zachmann, *ProtoSphere: a GPU-assisted prototype guided sphere packing algorithm for arbitrary objects*, *ACM SIGGRAPH ASIA 2010 Sketches*, 1 (2010).
- [17] R. D. S. Teixeira, *Automatic Analysis of Mammography Images: Classification of Breast Density*, Ph.D. thesis, Universidade do Porto (2013).
- [18] T. U. Eindhoven, B. I. Analysis, P. M. Systems, and A. Development, *Computer-aided analysis of non-mass-like enhancement in breast MR*, Ph.D. thesis, Technische Universiteit Eindhoven (2007).
- [19] G. Tortora and B. Derrickson, *Principles of anatomy and physiology*, (2001).
- [20] E. Sarru, F. Mudarris, and S. Amr, *Male breast cancer . Case report and brief review*, *Middle East Journal of Family Medicine* **6** (2004).
- [21] K. Cooper and K. Gosnell, *Foundations and Adult Health Nursing* (Elsevier Health Sciences, 2014) p. 2240.
- [22] V. a. McCormack and I. dos Santos Silva, *Breast density and parenchymal patterns as markers of breast cancer risk: a meta-analysis*. *Cancer epidemiology, biomarkers and prevention : a publication of the American Association for Cancer Research*, cosponsored by the American Society of Preventive Oncology **15**, 1159 (2006).
- [23] American Cancer Society, *Breast cancer*, Tech. Rep. (American Cancer Society, 2013).
- [24] G. P. Gupta and J. Massagué, *Cancer Metastasis: Building a Framework*, *Cell* **127**, 679 (2006).
- [25] B. Weigelt, J. L. Peterse, and L. J. van 't Veer, *Breast cancer metastasis: markers and models*. *Nature reviews. Cancer* **5**, 591 (2005).
- [26] L. LIBERMAN and J. H. MENELL, *Breast Imaging Reporting and Data System (BI-RADS)*, *The Radiologic clinics of North America* **40** (2002).
- [27] a. Jackson, D. Buckley, G. Parker, and M. Ah-See, *Dynamic contrast-enhanced magnetic resonance imaging in oncology* (Springer, 2005).
- [28] G. Agrawal, M. Y. Su, O. Nalcioğlu, S. a. Feig, and J. H. Chen, *Significance of breast lesion descriptors in the ACR BI-RADS MRI lexicon*, *Cancer* **115**, 1363 (2009).

- [29] A. C. of Radiology. BI-RADS Committee and A. C. of Radiology, *Breast imaging reporting and data system* (American College of Radiology, 1998).
- [30] D. Förnvik, S. A. Tingberg, and M. Ruschin, *Complementary analysis of breast cancer using MRI and breast tomosynthesis*, Ph.D. thesis, Lund University (2008).
- [31] M. J. Stoutjesdijk, J. Veltman, H. Huisman, N. Karssemeijer, J. O. Barentsz, J. G. Blickman, and C. Boetes, *Journal of Magnetic Resonance Imaging*, Vol. 26 (Wiley Online Library, 2007) pp. 606–614.
- [32] L. W. Nunes, M. D. Schnall, E. S. Siegelman, C. P. Langlotz, S. G. Orel, D. Sullivan, L. A. Muenz, C. A. Reynolds, and M. H. Torosian, *Diagnostic performance characteristics of architectural features revealed by high spatial-resolution MR imaging of the breast*. *AJR. American journal of roentgenology* **169**, 409 (1997).
- [33] L. W. Nunes, M. D. Schnall, S. G. Orel, M. G. Hochman, C. P. Langlotz, C. A. Reynolds, and M. H. Torosian, *Correlation of lesion appearance and histologic findings for the nodes of a breast MR imaging interpretation model*, *Radiographics* **19**, 79 (1999).
- [34] M. Tozaki and K. Fukuda, *High-spatial-resolution MRI of non-masslike breast lesions: interpretation model based on BI-RADS MRI descriptors*, *American Journal of Roentgenology* **187**, 330 (2006).
- [35] K. Nie, J.-H. Chen, J. Y. Hon, Y. Chu, O. Nalcioglu, and M.-Y. Su, *Quantitative analysis of lesion morphology and texture features for diagnostic prediction in breast MRI*, *Academic radiology* **15**, 1513 (2008).
- [36] N. Iyer, S. Jayanti, K. Lou, Y. Kalyanaraman, and K. Ramani, *Three-dimensional shape searching: state-of-the-art review and future trends*, *Computer-Aided Design* **37**, 509 (2005).
- [37] D. Newell, K. Nie, J. H. Chen, C. C. Hsu, H. J. Yu, O. Nalcioglu, and M. Y. Su, *Selection of diagnostic features on breast MRI to differentiate between malignant and benign lesions using computer-aided diagnosis: Differences in lesions presenting as mass and non-mass-like enhancement*, *European Radiology* **20**, 771 (2010).
- [38] A. N. Nnewihe, *HIGH RESOLUTION BREAST MRI*, Ph.D. thesis, Stanford University (2012).
- [39] R. M. Haralick, K. Shanmugam, and I. Dinstein, *Textural Features for Image Classification*, *IEEE Transactions on Systems, Man, and Cybernetics* **3** (1973), 10.1109/TSMC.1973.4309314.
- [40] W. Chen, M. L. Giger, H. Li, U. Bick, and G. M. Newstead, *Volumetric texture analysis of breast lesions on contrast-enhanced magnetic resonance images*, *Magnetic Resonance in Medicine* **58**, 562 (2007).
- [41] S. a. Jansen, X. Fan, G. S. Karczmar, H. Abe, R. a. Schmidt, and G. M. Newstead, *Differentiation between benign and malignant breast lesions detected by bilateral dynamic contrast-enhanced MRI: A sensitivity and specificity study*, *Magnetic Resonance in Medicine* **59**, 747 (2008).
- [42] M. D. Schnall, J. Blume, D. A. Bluemke, G. A. DeAngelis, N. DeBruhl, S. Harms, S. H. Heywang-Kobrunner, N. Hylton, C. K. Kuhl, E. D. Pisano, and Others, *Diagnostic architectural and dynamic features at breast MR imaging: multicenter study 1*, *Radiology* **238**, 42 (2006).
- [43] W. Chen, M. L. Giger, U. Bick, and G. M. Newstead, *Automatic identification and classification of characteristic kinetic curves of breast lesions on DCE-MRI*, *Medical Physics* **33**, 2878 (2006).

- [44] C. K. Kuhl, P. Mielcareck, S. Klaschik, C. Leutner, E. Wardelmann, J. Gieseke, and H. H. Schild, *Dynamic breast mr imaging: Are signal intensity time course data useful for differential diagnosis of enhancing lesions? 1*, *Radiology* **211**, 101 (1999).
- [45] S. A. Jansen, X. Fan, G. S. Karczmar, H. Abe, R. A. Schmidt, M. Giger, and G. M. Newstead, *DCEMRI of breast lesions: Is kinetic analysis equally effective for both mass and nonmass-like enhancement?* *Medical physics* **35**, 3102 (2008).
- [46] M. Goto, H. Ito, K. Akazawa, T. Kubota, O. Kizu, K. Yamada, and T. Nishimura, *Diagnosis of breast tumors by contrast-enhanced MR imaging: Comparison between the diagnostic performance of dynamic enhancement patterns and morphologic features*, *Journal of Magnetic Resonance Imaging* **25**, 104 (2007).
- [47] U. Wedegärtner, U. Bick, K. Wörtler, E. Rummeny, and G. Bongartz, *Differentiation between benign and malignant findings on MR-mammography: usefulness of morphological criteria*, *European radiology* **11**, 1645 (2001).
- [48] S. K. Plevritis, B. L. Daniel, R. J. Herfkens, G. H. Glover, Y. Yen, and C. S. Leong, *Improved diagnostic accuracy of breast lesions with combined rapid dynamic and high-resolution contrast-enhanced MR imaging: A multivariate ROC analysis*, in *Radiology*, Vol. 205 (RADIOLOGICAL SOC NORTH AMER 20TH AND NORTHAMPTON STS, EASTON, PA 18042, 1997) p. 95.
- [49] C. S. Leong, B. L. Daniel, R. J. Herfkens, R. L. Birdwell, S. S. Jeffrey, D. M. Ikeda, A. M. Sawyer-Glover, and G. H. Glover, *Characterization of breast lesion morphology with delayed 3DSSMT: An adjunct to dynamic breast MRI*, *Journal of Magnetic Resonance Imaging* **11**, 87 (2000).
- [50] P. Gibbs and L. W. Turnbull, *Textural analysis of contrast-enhanced MR images of the breast*, *Magnetic Resonance in Medicine* **50**, 92 (2003).
- [51] D. Rueckert, L. I. Sonoda, C. Hayes, D. L. G. Hill, M. O. Leach, and D. J. Hawkes, *Nonrigid registration using free-form deformations: application to breast MR images*, *Medical Imaging, IEEE Transactions on* **18**, 712 (1999).
- [52] H. L. L. Wang, A. Gubern-Mérida, O. Diaz, Y. Diez, R. Mann, S. Diekmann, F. Zöhrer and J. Schwaab, *Automated detection of motion in breast DCE-MRI to assess study quality and prevent unnecessary call-backs*, *Presented at European Congress of Radiology (ECR) (2015)*, [10.1594/ecr2015/C-1845](https://doi.org/10.1594/ecr2015/C-1845).
- [53] L. Wang, B. Platel, T. Ivanovskaya, M. Harz, and H. K. Hahn, *Fully automatic breast segmentation in 3D breast MRI*, in *Biomedical Imaging (ISBI), 2012 9th IEEE International Symposium on* (IEEE, 2012) pp. 1024–1027.
- [54] G. Bogdan and C. M. Christoudias., *Edge Detection and Image SegmentatiON (EDISON) System*, (2009).
- [55] D. Comaniciu, P. Meer, and S. Member, *Mean Shift : A Robust Approach Toward Feature Space Analysis*, *Pattern Analysis and Machine Intelligence, IEEE Transactions on* **24**, 603 (2002).
- [56] J. N. Kaftan, A. A. Bell, and T. Aach, *Mean Shift Segmentation-Evaluation of Optimization Techniques*. in *VISAPP (1)* (2008) pp. 365–374.
- [57] K. Fukunaga and L. D. Hostetler, *The estimation of the gradient of a density function, with applications in pattern recognition*, *Information Theory, IEEE Transactions on* **21**, 32 (1975).
- [58] R. O. Duda, P. E. Hart, and D. G. Stork, *Pattern classification. 2nd*, Edition. New York (2001).

- [59] K. G. Derpanis, *Mean shift clustering*, Lecture Notes. [http://www.cse.yorku.ca/~kosta/CompVis\\_Notes/mean\\_shift.pdf](http://www.cse.yorku.ca/~kosta/CompVis_Notes/mean_shift.pdf) (2005).
- [60] D. Comaniciu and P. Meer, *Robust analysis of feature spaces: color image segmentation*, in *Computer Vision and Pattern Recognition, 1997. Proceedings., 1997 IEEE Computer Society Conference on* (IEEE, 1997) pp. 750–755.
- [61] J. Teuber, R. Weller, G. Zachmann, and S. Guthe, *Fast Sphere Packings with Adaptive Grids on the GPU*, In *GIAR VRWorkshop*, 181 (2013).
- [62] F. Yu, Z. Lu, H. Luo, and P. Wang, *Three-Dimensional Model Analysis and Processing*, Advanced Topics in Science and Technology in China (Springer Berlin Heidelberg, 2011).
- [63] C.-C. Lin, W.-L. Tai, and C.-C. Chang, *Multilevel reversible data hiding based on histogram modification of difference images*, *Pattern Recognition* **41**, 3582 (2008).
- [64] M. Ankerst, G. Kastenmüller, H.-P. Kriegel, and T. Seidl, *3D shape histograms for similarity search and classification in spatial databases*, in *Advances in Spatial Databases* (Springer, 1999) pp. 207–226.
- [65] Z. Lian, A. Godil, and X. Sun, *Visual Similarity based 3D Shape Retrieval Using Bag-of-Features*, *Shape Modeling and Applications*, 25 (2010).
- [66] J. W. H. Tangelder and R. C. Veltkamp, *A survey of content based 3D shape retrieval methods*, *Multimedia Tools and Applications* **39**, 441 (2008).
- [67] V. Barra and S. Biasotti, *3D shape retrieval and classification using multiple kernel learning on extended Reeb graphs*, *The Visual Computer*, 1247 (2014).
- [68] B. Gärtner, *Fast and robust smallest enclosing balls*, *Algorithms-ESA'99* **1643**, 325 (1999).
- [69] E. Welzl, *Smallest enclosing disks (balls and ellipsoids)*, in *New Results and New Trends in Computer Science* (Springer-Verlag, Berlin/Heidelberg, 1991) pp. 359–370.
- [70] M. Hemmer, *Algebraic Foundations*, in *{CGAL} User and Reference Manual* (CGAL Editorial Board, 2015) 4th ed.
- [71] S. Ali, R. Veltri, J. A. Epstein, C. Christudass, and A. Madabhushi, *Cell cluster graph for prediction of biochemical recurrence in prostate cancer patients from tissue microarrays*, in *SPIE Medical Imaging* (International Society for Optics and Photonics, 2013) pp. 86760H—86760H.
- [72] J. Siek, L. Q. Lee, and A. Lumsdaine, *The boost graph library: user guide and reference manual*, C++ in-depth series (Addison-Wesley, 2002).
- [73] C. Correa and P. Lindstrom, *Towards Robust Topology of Sparsely Sampled Data*, *IEEE Transactions on Visualization and Computer Graphics* **17**, 1852 (2011).
- [74] C. D. Correa and P. Lindstrom, *Locally-scaled spectral clustering using empty region graphs*, in *Proceedings of the 18th ACM SIGKDD international conference on Knowledge discovery and data mining* (ACM, 2012) pp. 1330–1338.
- [75] G. Tinhofer, *A note on compact graphs*, *Discrete Applied Mathematics* **30**, 253 (1991).
- [76] F. Boutin and M. Hascoet, *Cluster validity indices for graph partitioning*, in *Information Visualisation, 2004. IV 2004. Proceedings. Eighth International Conference on*, IEEE (IEEE Computer Society, Washington, DC, 2004) pp. 376–381.

- [77] N. Bolshakova and F. Azuaje, *Cluster validation techniques for genome expression data*, Signal processing **83**, 825 (2003).
- [78] F. Harary, R. Z. Norman, and D. Models, *An Introduction to the Theory of Directed Graphs*, New York: Wiley. Harary Structural Models: An Introduction to the Theory of Directed Graphs 1965 (1965).
- [79] R. A. Botafogo, E. Rivlin, and B. Shneiderman, *Structural analysis of hypertexts: identifying hierarchies and useful metrics*, ACM Transactions on Information Systems (TOIS) **10**, 142 (1992).
- [80] J. C. Bezdek and N. R. Pal, *Some new indexes of cluster validity*, Systems, Man, and Cybernetics, Part B: Cybernetics, IEEE Transactions on **28**, 301 (1998).
- [81] D. L. Davies and D. W. Bouldin, *A cluster separation measure*. IEEE transactions on pattern analysis and machine intelligence **1**, 224 (1979).
- [82] C. Ding, X. He, H. Zha, M. Gu, and H. Simon, *Spectral min-max cut for graph partitioning and data clustering*, Lawrence Berkeley National Lab. Tech. report **47848** (2001).
- [83] F. Huang, S. Zhang, and X. Zhu, *Discovering network community based on multi-objective optimization*, Journal of Software **24**, 2062 (2013).
- [84] R. G. Raidou, U. A. V. D. Heide, C. V. Dinh, G. Ghobadi, J. F. Kallehauge, M. Breeuwer, and A. Vilanova, *Visual Analytics for the Exploration of Tumor Tissue Characterization*, Eurographics Conference on Visualization (EuroVis) 2015 **34** (2015).
- [85] U. Brandes, M. Gaertler, and D. Wagner, *Experiments on graph clustering algorithms* (Springer, 2003).
- [86] S. Mancoridis, B. S. Mitchell, C. Rorres, Y.-F. Chen, and E. R. Gansner, *Using Automatic Clustering to Produce High-Level System Organizations of Source Code*. in IWPC, Vol. 98 (Citeseer, 1998) pp. 45–52.
- [87] L. Hubert and P. Arabie, *Comparing partitions*, Journal of classification **2**, 193 (1985).
- [88] V. Venkatraman, L. Sael, and D. Kihara, *Potential for protein surface shape analysis using spherical harmonics and 3D Zernike descriptors*, Cell biochemistry and biophysics **54**, 23 (2009).
- [89] Z. Chen and S.-K. Sun, *A Zernike moment phase-based descriptor for local image representation and matching*, Image Processing, IEEE Transactions on **19**, 205 (2010).
- [90] J. Ricard, D. Coeurjolly, and A. Baskurt, *Generalizations of angular radial transform for 2D and 3D shape retrieval*, Pattern Recognition Letters **26**, 2174 (2005).
- [91] M. R. Teague, *Image analysis via the general theory of moments\**, JOSA **70**, 920 (1980).
- [92] C.-H. Teh and R. T. Chin, *On image analysis by the methods of moments*, Pattern Analysis and Machine Intelligence, IEEE Transactions on **10**, 496 (1988).
- [93] Z. von F, *Beugungstheorie des schneidenverfahrens und seiner verbesserten form, der phasenkontrastmethode*, Physica **1**, 689 (1934).
- [94] M. S. Al-Rawi, *3D (pseudo) Zernike moments: Fast computation via symmetry properties of spherical harmonics and recursive radial polynomials*, in *Image Processing (ICIP), 2012 19th IEEE International Conference on* (IEEE, 2012) pp. 2353–2356.

- [95] P. G. Callahan and M. D. Graef, *Precipitate shape fitting and reconstruction by means of 3D Zernike functions*, *Modelling and Simulation in Materials Science and Engineering* **20**, 15003 (2012).
- [96] N. Canterakis, *3D Zernike moments and Zernike affine invariants for 3D image analysis and recognition*, in *In 11th Scandinavian Conf. on Image Analysis* (Citeseer, 1999).
- [97] M. Novotni and R. Klein, *Shape retrieval using 3D Zernike descriptors*, *Computer-Aided Design* **36**, 1047 (2004).
- [98] O. Pauly and Others, *Random Forests for Medical Applications*, *Ph.D. thesis*, Technische Universität München (2012).
- [99] I. G. Maglogiannis, *Emerging Artificial Intelligence Applications in Computer Engineering: Real World AI Systems with Applications in EHealth, HCI, Information Retrieval and Pervasive Technologies*, *Frontiers in artificial intelligence and applications* (IOS Press, 2007).
- [100] R. Caruana and A. Niculescu-Mizil, *An Empirical Comparison of Supervised Learning Algorithms*, in *Proceedings of the 23rd International Conference on Machine Learning*, ICML '06 (ACM, New York, NY, USA, 2006) pp. 161–168.
- [101] J. Gall and V. Lempitsky, *Class-specific hough forests for object detection*, in *Decision forests for computer vision and medical image analysis* (Springer, 2013) Chap. Decision F, pp. 143–157.
- [102] G. Yu, J. Yuan, and Z. Liu, *Unsupervised random forest indexing for fast action search*, in *Computer Vision and Pattern Recognition (CVPR)* (IEEE, Providence, RI, 2011) pp. 865–872.
- [103] L. Breiman, *Random forests*, *Machine learning* **45**, 5 (2001).
- [104] L. Breiman, *Bagging predictors*, *Machine learning* **24**, 123 (1996).
- [105] R. Hänsch and O. Hellwich, *Performance Assessment and Interpretation of Random Forests by Three-dimensional Visualizations*, *International Conference on Information Visualization Theory and Application (IVAPP 2015)* , 149 (2015).
- [106] D. Benyamin, *A Gentle Introduction to Random Forests, Ensembles, and Performance Metrics in a Commercial System | Blog & Press* (Retrieved from <http://bit.ly/1WbxrMc>), (2012).
- [107] U. Köthe, *The VIGRA Computer Vision Library* (Retrieved from <http://ukoethe.github.io/vigra>), (2015).
- [108] Wikipedia, *MeVisLab* - [www.wikipedia.org/wiki/MeVisLab](http://www.wikipedia.org/wiki/MeVisLab), (2015).
- [109] MeVis Medical Solutions, *MeVisLab Reference Manual*, (2015).
- [110] P. Viola and M. Jones, *Rapid object detection using a boosted cascade of simple features*, in *Computer Vision and Pattern Recognition, 2001. CVPR 2001. Proceedings of the 2001 IEEE Computer Society Conference on*, Vol. 1, IEEE (IEEE, 2001) pp. I—511.
- [111] S. B. Kotsiantis, I. D. Zaharakis, and P. E. Pintelas, *Machine learning: a review of classification and combining techniques*, *Artificial Intelligence Review* **26**, 159 (2006).
- [112] M. Sokolova, N. Japkowicz, and S. Szpakowicz, *Beyond accuracy, F-score and ROC: a family of discriminant measures for performance evaluation*, in *AI 2006: Advances in Artificial Intelligence* (Springer, 2006) pp. 1015–1021.

- [113] C. Ferri, P. Flach, J. Hernández-Orallo, and A. Senad, *Modifying ROC curves to incorporate predicted probabilities*, in *Proceedings of the second workshop on ROC analysis in machine learning* (2005) pp. 33–40.
- [114] F. Schoonjans, *ROC curves - [www.medcalc.org/manual/roc-curves.php](http://www.medcalc.org/manual/roc-curves.php)*, (2015).
- [115] M. Hall, E. Frank, G. Holmes, B. Pfahringer, P. Reutemann, and I. H. Witten, *The WEKA data mining software: an update*, ACM SIGKDD explorations newsletter **11**, 10 (2009).
- [116] J. Shao, *Linear model selection by cross-validation*, Journal of the American statistical Association **88**, 486 (1993).
- [117] Leo Breiman, *Random forests - classification description*, (2015).
- [118] T. Lindgren, *Methods for rule conflict resolution*, in *Machine Learning: ECML 2004* (Springer, 2004) pp. 262–273.
- [119] H. Yoon, K. Yang, and C. Shahabi, *Feature subset selection and feature ranking for multivariate time series*, Knowledge and Data Engineering, IEEE Transactions on **17**, 1186 (2005).
- [120] G. J. Williams, *Data Mining with {Rattle} and {R}: The art of excavating data for knowledge discovery*, Use R! (Springer, 2011).
- [121] R. A. Berk, *Data mining within a regression framework*, in *Data Mining and Knowledge Discovery Handbook* (Springer, 2005) pp. 231–255.
- [122] F. Wolfe, D. J. Clauw, M.-A. Fitzcharles, D. L. Goldenberg, R. S. Katz, P. Mease, A. S. Russell, I. J. Russell, J. B. Winfield, and M. B. Yunus, *The American College of Rheumatology preliminary diagnostic criteria for fibromyalgia and measurement of symptom severity*, Arthritis care & research **62**, 600 (2010).
- [123] K. Alexandros and H. Melanie, *Model selection via meta-learning: a comparative study*, International Journal on Artificial Intelligence Tools **10**, 525 (2001).
- [124] L. J. Cao and W. K. Chong, *Feature extraction in support vector machine: a comparison of PCA, XPCA and ICA*, in *Neural Information Processing, 2002. ICONIP'02. Proceedings of the 9th International Conference on*, Vol. 2 (IEEE, 2002) pp. 1001–1005.
- [125] M. Hall, *Principal Components - Weka documentation*, (2015).
- [126] M. J. Pencina, R. B. D'Agostino, R. B. D'Agostino, and R. S. Vasan, *Evaluating the added predictive ability of a new marker: from area under the ROC curve to reclassification and beyond*, Statistics in medicine **27**, 157 (2008).
- [127] D. J. Hand and R. J. Till, *A simple generalisation of the area under the ROC curve for multiple class classification problems*, Machine learning **45**, 171 (2001).
- [128] A. T. Stavros, D. Thickman, C. L. Rapp, M. A. Dennis, S. H. Parker, and G. A. Sisney, *Solid breast nodules: use of sonography to distinguish between benign and malignant lesions*. Radiology **196**, 123 (1995).
- [129] T. Matsubara, T. Ichikawa, T. Hara, H. Fujita, S. Kasai, T. Endo, and T. Iwase, *Novel method for detecting mammographic architectural distortion based on concentration of mammary gland*, International Congress Series **1268**, 867 (2004).
- [130] I. Jolliffe, *Principal component analysis* (Wiley Online Library, 2002).

- 
- [131] T. Fawcett, *An introduction to ROC analysis*, Pattern recognition letters **27**, 861 (2006).
- [132] S. Beucher and F. Meyer, *The morphological approach to segmentation: the watershed transformation*, OPTICAL ENGINEERING-NEW YORK-MARCEL DEKKER INCORPORATED- **34**, 433 (1992).
- [133] R. Adams and L. Bischof, *Seeded region growing*, Pattern Analysis and Machine Intelligence, IEEE Transactions on **16**, 641 (1994).